Astronomy Letters, Vol. 28, No. 1, 2002, pp. 1–11. Translated from Pis'ma v Astronomicheskiĭ Zhurnal, Vol. 28, No. 1, 2002, pp. 3–13.
Original Russian Text Copyright © 2002 by Reshetnikov, Vasil'ev.

The Observed Structure of Extremely Distant Galaxies

V. P. Reshetnikov[*] **and A. A. Vasil'ev**

Astronomical Institute, St. Petersburg State University, Bibliotechnaya pl. 2, Petrodvorets, 198904 Russia

Received July 18, 2001

Abstract—We have identified 22 galaxies with photometric redshifts $z_{\rm ph} = 5$–7 in the northern and southern Hubble Space Telescope deep fields. An analysis of the images of these objects shows that they are asymmetric and very compact ($\sim$1 kpc) structures with high surface brightness and absolute magnitudes of $M_B \approx -20^m$. The average spectral energy distribution for these galaxies agrees with the distributions for galaxies with active star formation. The star formation rate in galaxies with $z_{\rm ph} = 5$–7 was estimated from their luminosity at $\lambda = 1500$ Å to be $\sim$30 $M_\odot$ yr^{-1}. The spatial density of these objects is close to the current spatial density of bright galaxies. All the above properties of the distant galaxies considered are very similar to those of the so-called Lyman break galaxies (LBGs) with $z \sim 3$–4. The similarity between the objects considered and LBGs suggests that at $z \sim 6$, we observe the progenitors of present-day galaxies that form during mergers of protogalactic objects and that undergo intense starbursts.

Key words: *theoretical and observational cosmology; galaxies, groups and clusters of galaxies, intergalactic gas*

INTRODUCTION

The Hubble Space Telescope (HST) and major ground-based telescopes allowed several galaxies (not quasars or radio galaxies) at large "cosmological" redshifts to be identified and studied in recent years (Stern and Spinrad 1999). For instance, objects with redshifts $z = 5.60$ (Weymann *et al.* 1998) and $z = 5.34$ (Spinrad *et al.* 1998) have been discovered in the northern Hubble Deep Field. Other galaxies with $z = 5.34$ (Dey *et al.* 1998), $z = 5.74$ (Hu *et al.* 1999), and $z = 5.63$ (Dawson *et al.* 2001) are also known. The importance given to searches for such extremely distant and, therefore, very young objects is quite understandable, because they serve as crucial tests for modern models of galaxy formation and also allow the processes in the relatively early Universe to be studied.

The principal aim of our work is to attempt to analyze the observed structure of the most distant objects identified in deep fields in the spectral region at the boundary between the optical and the infrared.

GALAXY SAMPLE

The goal of this work unambiguously defines both the region to be searched for the objects we are interested in (the northern and southern Hubble Deep Fields) and the technique capable of identifying them (photometric redshifts).

Hubble Deep Fields (northern and southern—HDF-N and HDF-S) are currently the deepest "punctures" made into the Universe (Ferguson *et al.* 2000). In these two small areas (each with a size of $\sim$5.3 arcmin^2) several thousand objects have been identified down to a limiting magnitude of $V \sim 30^m$. Each Deep Field pixel has an angular size of only $0''.04$, which allows objects with sizes $\sim$1 kpc to be resolved at almost all z. Original field images were obtained in F300W, F450W, F606W, and F814W broadband filters (numbers in filter names indicate the central wavelength in nanometers). These filters are often referred to as U_{300}, B_{450}, V_{606}, and I_{814} because of their relative proximity to the corresponding standard filters. Later, HST and ground-based infrared (JHK) images of the deep fields were taken. These additional data were obtained mostly with lower angular resolution and lower limiting magnitude.

We decided to analyze objects located in two fields and having redshifts ranging from 5 to 7. The upper limit is due to the fact that at $z > 7$ the part of the galactic spectrum with $\lambda_0 > 1216$ Å (λ_0 is the wavelength in the restframe of the galaxy) falls beyond the passband of the I_{814} filter (the longest wavelength filter in which the original deep-field images are obtained). At $\lambda_0 < 1216$ Å, the observed flux from distant objects decreases abruptly due to absorption by

---

[*] E-mail: `resh@astro.spbu.ru`

Table 1. Galaxies in HDF-N

N	Name	$I_{814}(AB)$	$z_{\rm sp}$	$z_{\rm ph}$	Type
3a	3-951.1	26.20	5.34	5.25	Irr
3b	3-951.2	26.95	5.34	5.25	Irr
213	4-473.0	27.17	5.60	5.95	Irr
328	4-200.0	26.19	–	5.20	Irr
343	3-543.0	27.78	–	5.95	Irr
367	3-489.0	26.74	–	5.18	Irr
576	3-228.0	26.93	–	5.58	Irr
658	4-799.0	27.30	–	5.33	Irr
714	3-44.0	27.20	–	5.29	Irr

Table 2. Galaxies in HDF-S

N	Name	$I_{814}(AB)$	$z_{\rm ph}$	Type
0036	SB-WF-0393-1295	29.86	6.75	Scd
0089	SB-WF-0648-0506	28.53	5.49	Scd
0277	SB-WF-1510-1270	29.60	6.63	Sbc
0400	SB-WF-1947-1654	28.23	6.52	SB1
0470	SB-WF-2127-1818	29.77	6.85	SB1
0543	SB-WF-2328-3923	27.55	5.12	SB2
0611	SB-WF-2434-2255	28.28	5.20	Irr
0696	SB-WF-2611-1523	28.73	5.26	SB1
0881	SB-WF-3032-2976	29.19	6.01	Irr
0886	SB-WF-3049-1323	28.07	5.56	SB2
0932	SB-WF-3144-0926	29.10	6.94	SB1
1079	SB-WF-3473-1780	28.93	5.22	SB2
1097	SB-WF-3516-0827	29.25	5.72	Irr

intergalactic HI clouds (Madau 1995). We therefore cannot expect the images of more distant objects to be seen in the I_{814} band. The lower limit ($z > 5$) is set arbitrarily.

Recall that the age-redshift dependence is strongly nonlinear and galaxies at $z \sim 5$–7 differ little in age from those at $z \sim 3$–4 (of which $\sim 10^3$ are already known). Let us illustrate this point using the Einstein–deSitter model as an example. In this model, age t is related to z in the following simple way: $t = \frac{2}{3}(1+z)^{-\frac{3}{2}} H_0^{-1}$, where H_0 is the Hubble constant. It thus follows that for $H_0 = 50$ km/s/Mpc the present-day ($z = 0$) age of the Universe is equal to $t_0 = 13.0$ Gyr. Galaxies with $z = 3$ are observed at $t = 1.6$ Gyr, and those with $z = 4$, at $t = 1.2$ Gyr. Redshifts $z = 5$ and $z = 7$ correspond to the age of the Universe of 0.9 and 0.6 Gyr, respectively. The galaxies at $z \sim 3.5$ are therefore "older" than those observed at $z \sim 6$ by no more than 10^9 yr. Most of the time of cosmic evolution falls within $z \leq 1$.

To identify objects with $z = 5$–7, we used published photometric redshifts $z_{\rm ph}$ of objects in HDF-N and HDF-S adopted from the catalogs of Fernandez-Soto *et al.* (1999) and Fontana *et al.* (2000) (see the corresponding WWW addresses in the original papers). The $z_{\rm ph}$ estimates in the corresponding papers are based on seven-color (V_{300} to K) photometry. The accuracy of $z_{\rm ph}$ is difficult to assess, because only several galaxies are now known to have spectroscopic z exceeding 5 (see Introduction). However, in HDF-N, two such such objects were classified as galaxies with $z > 5$ based just on photometric redshifts, and their $z_{\rm ph}$ were subsequently corroborated through spectroscopic observations (Spinrad *et al.* 1998; Weymann *et al.* 1998). For these two objects, the difference between the two redshifts $z - z_{\rm ph}$ amounts to -0.13 ± 0.22 (see Table 1). Note also that mutually independent data by Fernandez-Soto *et al.* (1999) and Fontana *et al.* (2000) yield $z_{\rm ph}$ that agree fairly well with each other. Thus, the z_{ph} values for HDF-N objects with $z = 5$–7 identified using the data of Fontana *et al.* (2000) differ from the z_{ph} determinations of Fernandez-Soto *et al.* (1999) by $+0.24 \pm 0.39$ (eight galaxies).

The subsequent work was based on the original I_{814}-band frames of the two fields available from the site of the Space Telescope Science Institute (STScI). To identify real galaxies, we analyzed surface brightness distributions for all objects with $z_{\rm ph} = 5$–7. An analysis of the profiles of several dozen stars in these fields showed that they had FWHM $= 0''.14$. Note that the width of the stellar profiles depends only slightly on apparent magnitude: FWHM $= 0''.146 \pm 0''.018$ and FWHM $= 0''.139 \pm 0''.026$ for stars with $I_{814} > 22^m$ and fainter stars with $I_{814} > 24^m$, respectively. We left in the final list only the resolvable objects whose brightness distribution is more extended that those of stars (FWHM $> 0''.14$).

Tables 1 and 2 list candidate distant galaxies in HDF-N and HDF-S, respectively. The first column of Table 1 gives the number of the object according to the catalog of Fernandez-Soto *et al.* (1999); the second column, its name according to Williams *et al.* (1996); the third column, the apparent I_{814} magnitude in the AB system of Oke (1974); the fourth column, the spectroscopic redshift (Spinrad *et al.* 1998; Weymann *et al.* 1998); the fifth column, the photometric redshift $z_{\rm ph}$ according to Fontana *et al.* (2000) and the last column, the spectral type of the galaxy (i.e., the spectral type that best describes the observed spectral energy distribution). The columns

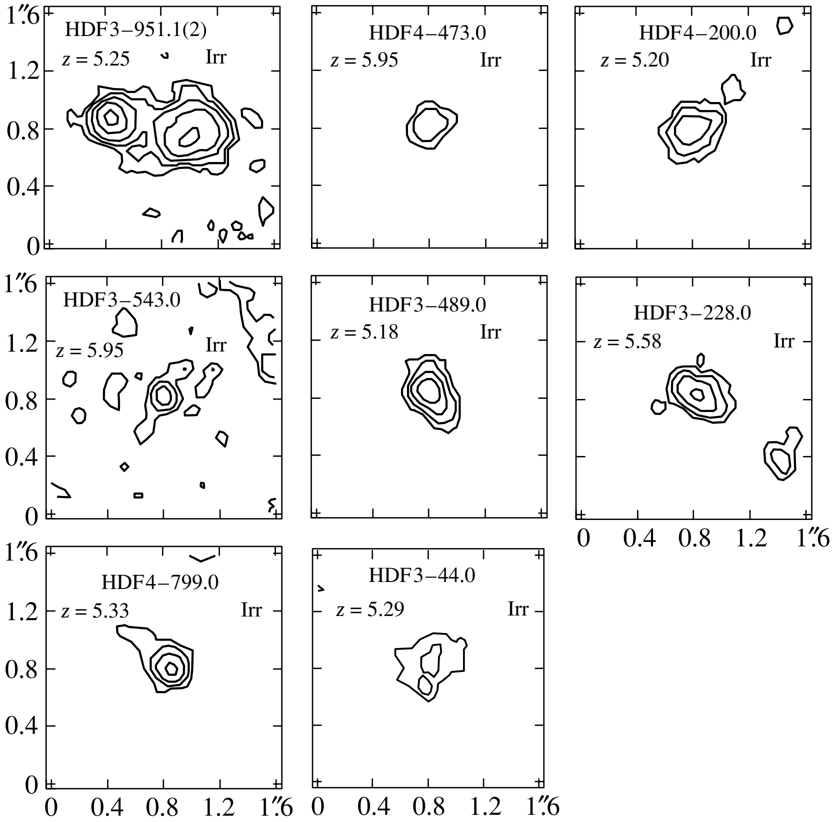

Fig. 1. Isophotes for HDF-N galaxies with $z_{\rm ph} = 5$–7. Indicated on each map are the name of the galaxy according to Williams *et al.* (1996), its photometric redshift, and spectral type. The size of the figure is 1″.6 × 1″.6, and its orientation coincides with that of the deep field. The outer isophote corresponds to $\mu(I_{814}) = 26.0$ ($\mu(I_{814}) = 26.5$ for HDF3-543.0) and contours are drawn with a step of 0.5.

of Table 2 contain the following data: the number of the galaxy according to Fontana *et al.* (2000); the name according to the Stony Brook group catalog (Fernandez-Soto *et al.* 1999); the apparent magnitude in the I_{814} filter of the AB system of Oke (1974); a photometric redshift; and the spectral type according to Fontana *et al.* (2000).

It can be seen from Tables 1 and 2 that 9 (including the double galaxy HDF 3–951.1/2) and 13 galaxies with $z = 5$–7 have been identified in HDF-N and HDF-S, respectively. Table 3 summarizes the average parameters of the objects found in the two fields. Note that objects in HDF-S are fainter and have, on the average, larger $z_{\rm ph}$ compared to the galaxies of the northern field. However, these differences between the average galaxy parameters are not statistically significant given the observed scatter of individual values.

We constructed our sample based on redshifts estimated from multicolor photometry, and we must therefore bear in mind that it may contain objects with the redshifts z outside the interval considered. That is why we hereafter use only the mean values of various galaxy parameters assuming that they remain relatively stable against removal or addition of several objects (the medians are close to the means in all of the cases considered).

PARAMETERS OF GALAXIES

1. Morphology

Figures 1 and 2 show smoothed contour maps for the galaxies of our sample. As is evident from these maps, our sample contains practically no regular symmetric objects. Most of the galaxies exhibit various asymmetries and structural deformations typical of local interacting and merging galaxies.

Table 3. Average parameters of galaxies

Field	N	$\langle z\rangle$	$\langle I_{814}\rangle$
HDF-N	9	$5.42 \pm 0.25(\sigma)$	$26.94 \pm 0.51(\sigma)$
HDF-S	13	5.94 ± 0.70	28.85 ± 0.70
HDF-N + HDF-S	22	5.73 ± 0.61	28.07 ± 1.14

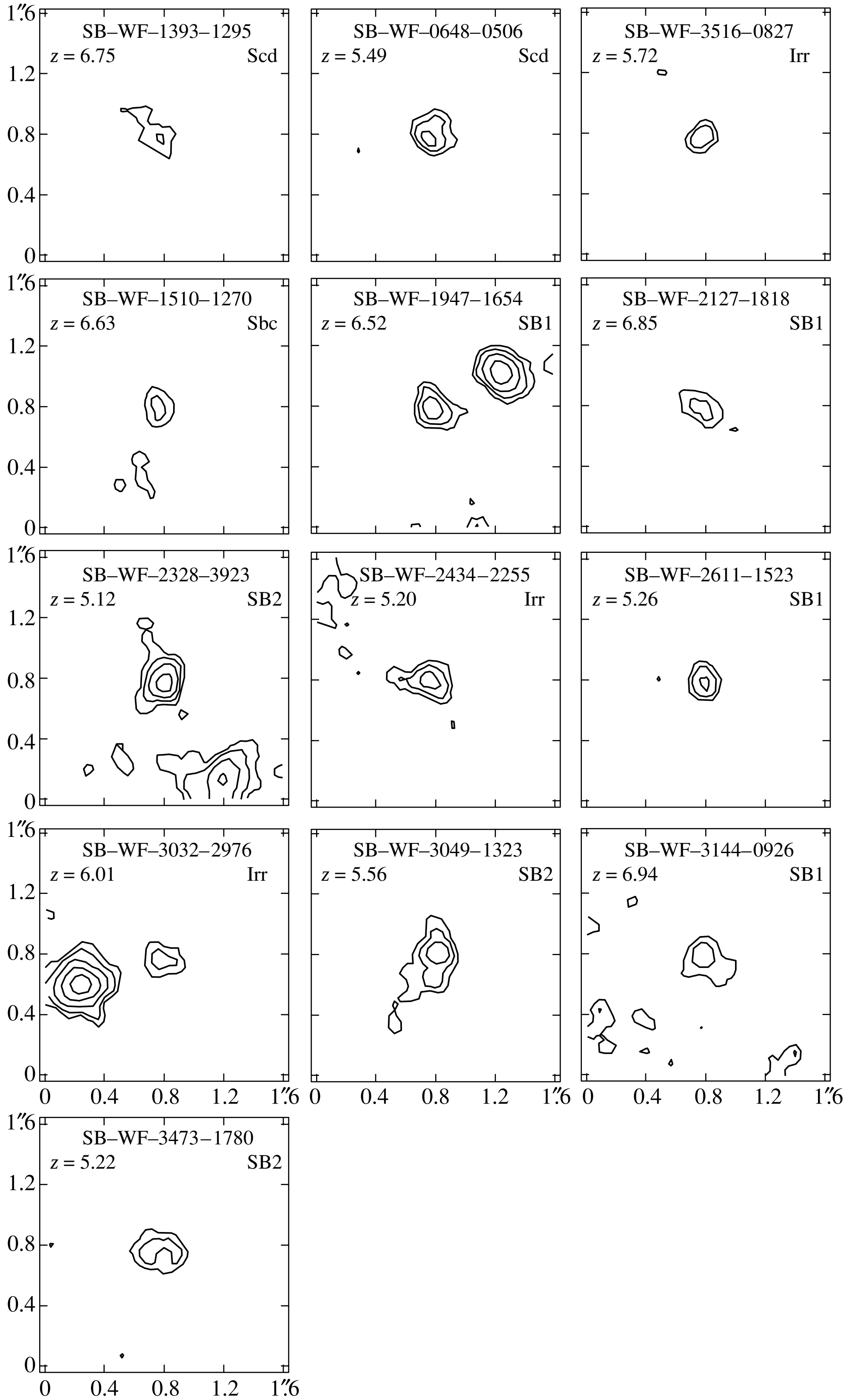

Fig. 2. Contour maps for galaxies with $z_{\rm ph} = 5$–7 in HDF-S. Indicated on each map are the name of the galaxy according to Fernandez-Soto *et al.* (1999), photometric redshift, and spectral type. The size of the figure is $1''.6 \times 1''.6$ and its orientation coincides with the original orientation of the deep field. The outer isophote corresponds to $\mu(I_{814}) = 26.0$, and contours are drawn at 0.5.

To quantitatively estimate the asymmetry of objects with $z_{\rm ph} = 5$–7, we analyzed their indices of rotational asymmetry A_{180}. We computed this index by subtracting from the initial image the image turned by 180° and normalizing the resulting difference to the initial image (the sum of relative brightness values within the galaxy). This index correlates with a number of galaxy parameters and can be used to construct an objective quantitative classification (Conselice *et al.* 2000). As comparison objects, we analyzed the sample of local interacting systems described by Reshetnikov and Combes (1996). The mean asymmetry indices for 28 interacting galaxies whose projected images do not overlap considerably are equal to $A_{180}(B) = 0.27 \pm 0.04$ and $A_{180}(I) = 0.28 \pm 0.05$ for the B and I bands, respectively. The observed asymmetry indices of galaxies with $z_{\rm ph} = 5$–7 found in the northern and southern fields within the framework of the same program are equal to $A_{180}(I_{814}) = 0.14 \pm 0.04$ and 0.13 ± 0.03, respectively.

The indices of distant and nearby galaxies cannot be compared directly, because (1) the images of the two types of objects are of very different resolutions; (2) the cosmological dimming of surface brightness the indices of distant galaxies must characterize their bright central regions; and (3) the possible problem with studying the asymmetry of distant galaxies is that in the case of objects with $z_{\rm ph} = 5$–7, the asymmetry measured in the I_{814} band actually refers to the ultraviolet region of the spectrum (∼1000–1500 Å) in the restframe of the galaxy, while the corresponding UV asymmetry of nearby objects is poorly known. The first two factors strongly decrease the observed asymmetry. Simulations run by Conselice *et al.* (2000) allowed these authors to show that degradation of linear resolution decreases the observed asymmetry index. The same authors demonstrated that the asymmetry of spiral galaxies usually strongly increases (severalfold) as one passes from the central regions toward the periphery. The asymmetry of distant galaxies measured under the same conditions as that of nearby galaxies can therefore be several times higher than the observed value. However, the asymmetry indices measured in the UV can be overestimated compared to optical determinations, and the third factor might therefore operate in the opposite sense.

It can be concluded, given the above uncertainties, that the observed structural asymmetry of galaxies with $z_{\rm ph} = 5$–7 is consistent with the assumption that it is a result of a gravitational perturbation.

2. Size

The mean observed angular isophotal diameter of galaxies at the $\mu(I_{814}) = 26.0$ level is $\langle d \rangle = 0''.43 \pm 0''.14$ (HDF-N—$0''.51 \pm 0''.13$, HDF-S—$0''.36 \pm 0''.11$). This corresponds to a linear diameter of 2.3 kpc (in terms of the Einstein–deSitter model with $H_0 = 50$ km/s/Mpc, $\Omega_m = 1.0$, and $\Omega_\Lambda = 0$) and 2.5 kpc for a model with nonzero Λ-term ($H_0 = 70$ km/s/Mpc, $\Omega_m = 0.3$, $\Omega_\Lambda = 0.7$, and $t_0 = 13.5$ Gyr). The above diameter is evidently very small compared to those of normal galaxies with $z = 0$. One must, however, bear in mind that due to cosmological dimming of surface brightness in the expanding Universe $\propto \dfrac{1}{(1+z)^4}$, the brightness of galaxies at $z = 5.73$ is $8^m.3$ lower than would be expected for similar objects at $z = 0$. Moreover, the k-correction can also decrease the observed brightness. What we observe in distant galaxies might possibly be only their brightest regions whose sizes by no means characterize the total extent of the entire objects.

The effective radius, which in practice is determined simply as the radius $r_{1/2}$ of a round diaphragm centered on the nucleus and containing half the total flux, or the full width of image at half maximum are often used as objective parameters characterizing the sizes of galaxies. The mean observed value for nine objects in HDF-N is $\langle r_{1/2} \rangle = 0''.20 \pm 0''.07$. Galaxies in the southern field are, on the average, fainter and smaller in size, yielding a formal estimate of $\langle r_{1/2} \rangle \le 0''.1$. The mean value averaged over both fields is $\langle r_{1/2} \rangle = 0''.10 \pm 0''.09$. Therefore, $r_{1/2}$ for objects with $z_{\rm ph} = 5$–7 correspond to linear sizes of ≤1 kpc, which is characteristic of very compact galaxies. We have, e.g., $r_{1/2} = 1.678h$ for a round galaxy with exponential surface brightness distribution, where h is the exponential disk scale. It follows from this that $h < 1$ kpc for distant galaxies provided that their brightness distribution can be fit to an exponential model (for reference, the corresponding scale length for the Milky Way is ∼3 kpc). Note also that radii $r_{1/2}$ for objects with $z_{\rm ph} = 5$–7 are in both angular and linear terms similar to (or somewhat smaller than) the corresponding parameters of Lyman break galaxies (LBGs) identified at $z \sim 3$ (Steidel *et al.* 1996a).

The mean FWHM of galaxies inferred from their two-dimensional images and corrected for the FWHM of stellar images is equal to $\langle \mathrm{FWHM} \rangle = 0''.26 \pm 0''.10$ and $\langle \mathrm{FWHM} \rangle = 0''.19 \pm 0''.09$ for the northern and southern fields, respectively. The combined sample including both fields yields $\langle \mathrm{FWHM} \rangle =$

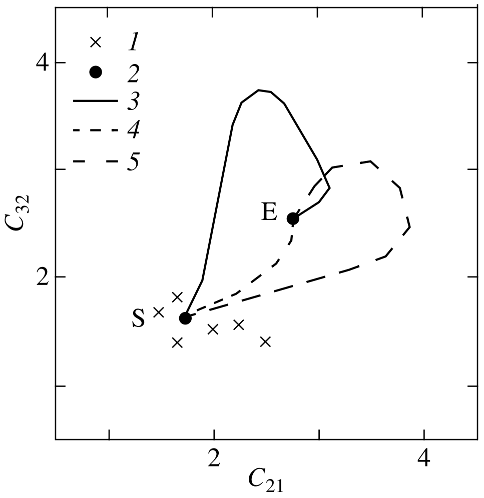

Fig. 3. Distribution of I_{814}-band concentration indices of HDF-N galaxies (*1* and *2*) are the expected values for an exponential disk (S) and the de Vaucoulers law (E), respectively. (*3*, *4*, and *5*) show the model relations for galaxies with the effective bulge radius to exponential disk scale ratios of $r_e/h = 10$, $r_e/h = 1$, and $r_e/h = 0.2$, respectively (Reshetnikov 1990).

$0''.21 \pm 0''.10$. Our measurements of the I_{814}-band FWHM for galaxies HDF 3–951.1/2 ($0''.47/0''.25$) agree well with similar measurements by Spinrad *et al.* (1998) ($0''.50/0''.28$). The observational estimates of the FWHM of the images of distant galaxies (FWHM $\sim$ 1 kpc) are also indicative of the compact sizes of the corresponding objects. We thus have FWHM $= 1.39h$ for exponential surface brightness distribution, implying that $h \leq 1$ kpc for distant galaxies.

3. Brightness Distribution

To analyze the surface brightness distributions in objects with $z_{\rm ph} = 5$–7, we first adopt the approach based on average parameters involving the so-called galaxy concentration indices C_{21} and C_{32} introduced by de Vaucouleurs and Aguero (1973). These indices characterize galaxy brightness distributions and correlate with the morphological type and bulge-to-disk luminosity ratio (Reshetnikov 1990). The indices in question can be defined, ignoring the apparent galaxy oblateness, as follows: $C_{21} = \dfrac{r_{1/2}}{r_{1/4}}$ and $C_{32} = \dfrac{r_{3/4}}{r_{1/2}}$, where $r_{1/4}$, $r_{1/2}$, and $r_{3/4}$ are the radii containing a quarter, half, and three quarters of the entire luminosity of the corresponding galaxy, respectively. It can be easily inferred that ($C_{21} = 1.75$, $C_{32} = 1.60$) and ($C_{21} = 2.75$, $C_{32} = 2.54$) for objects described by exponential brightness distribution and the de Vaucouleurs law, respectively.

Figure 3 shows the distribution of parameters of galaxies in HDF-N (southern-field objects are relatively fainter, and, therefore, their inferred parameters are more uncertain) on the C_{21}–C_{32} plane. As is evident from this figure, the averaged global photometric structure of distant objects considered is close to that of the exponential disk model.

Figure 4 shows the smoothed surface brightness distributions along apparent major axes of galaxies in the HDF-N. Cross sections of southern-field objects have similar structures and we therefore do not show them here. These distributions are asymmetric and noisy and can be fitted by exponential law in the case of relatively bright galaxies. The mean characteristics averaged over ten such exponential objects are: $\langle \mu_0(I_{814}) \rangle = 24.83 \pm 0.72$ (central surface brightness) and $h = 0''.17 \pm 0''.05$. The exponential scale length agrees, within the scatter, with earlier indirect estimates (see Section 2). To compare the central surface brightness with the corresponding parameter for nearby galaxies, it must be k-corrected and adjusted for cosmological brightness dimming. Absorption due to intervening HI clouds can be neglected in the I_{814} filter and at $z < 6$ (Madau *et al.* 1996).

For later-type galaxies and starburst objects, k-corrections are usually relatively small (Poggianti 1997). This is due to the fact that the spectral energy distributions of such objects remain flat or even increase with decreasing wavelength. Figure 5 shows, by way of example, the relative spectral energy distribution of a starburst galaxy with small internal absorption [$E(B-V) < 0.10$] according to Kinney *et al.* (1996). This distribution was obtained by averaging individual data for 39 galaxies. As is evident from the figure, in the wavelength interval 1200 Å $< \lambda \leq$ 10000 Å, the observed distribution can be, to a first approximation, fitted by a power-law dependence of the form $F(\lambda) \propto \lambda^{\beta}$, where $\beta = -1.1$, or, in frequency terms, $F(\nu) \propto \nu^{-\alpha}$, where $\alpha = \beta + 2 = 0.9$. The k-correction can then be inferred from the simple formula $k(z) = 2.5(\alpha - 1)\log(1+z)$ (Peacock 1999). For $z = 5.73$ and $\alpha = 0.9$, we obtain $k(5.73) = -0.25\log(1+z) = -0^m.2$ (the minus sign means that the galaxy becomes brighter). More accurate computations of k-corrections for starburst galaxies corroborate this estimate ($k \leq 1^m$) for I_{814} filter to redshifts as large as $z \sim 5$–6.

It can be estimated, neglecting k-correction, that the observed brightness should correspond to a B-band restframe value of $\mu_0(B) \sim 18^m$ ($\sim 4000 L_\odot B/{\rm pc}^2$). This is a very high surface brightness, which is 3–4^m above the typical levels for bright nearby spirals. No such disks can be found in our neighborhood, except, perhaps, for stellar disks in

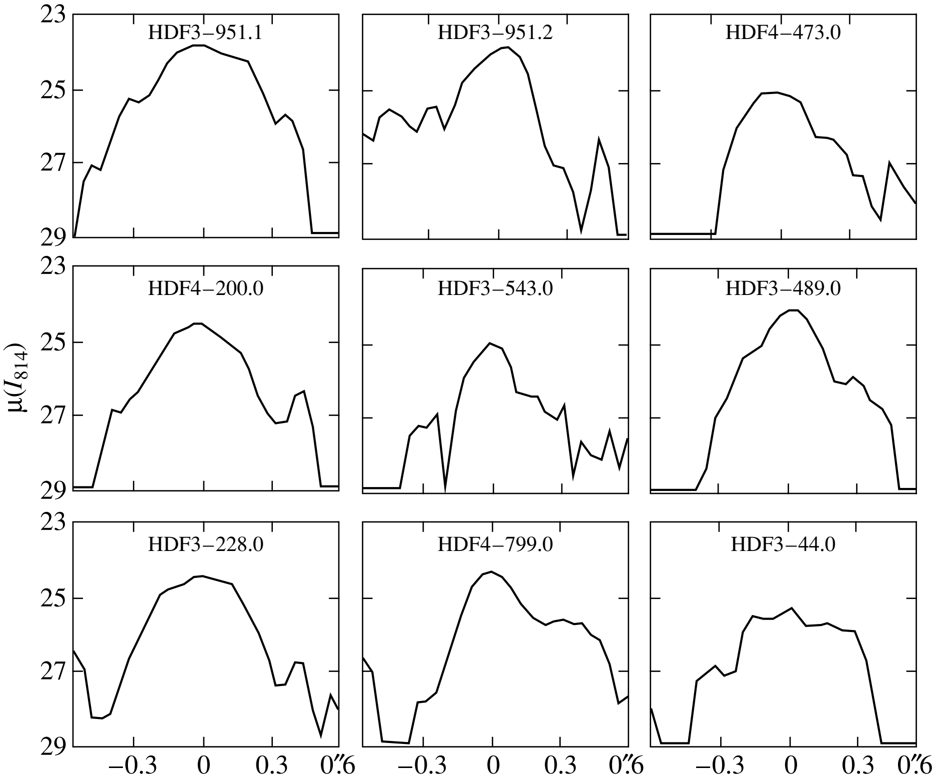

Fig. 4. I_{814}-band major-axis sections of galaxies in HDF-N.

the nuclei of E/S0 galaxies. However, the latter are, as a rule, more compact [see Fig. 1 in Reshetnikov (2000)]. The characteristics of the disks of galaxies at $z_{\rm ph} = 5$–7 are, on the whole, reminiscent of those of LBG at $z \sim 3$ (Steidel *et al.* 1996a).

Very high observed disk brightness values in distant galaxies is something to be expected, because at such large redshifts only extremely bright objects can be seen due to cosmological dimming ($\sim 8^m$). The high surface brightness of these objects must be explained by powerful bursts of star formation. If the ensuing photometric evolution is of a "passive" type, the surface brightness (and luminosities, see Section 4) of these galaxies should have decreased by now by several magnitudes and become quite typical of the disks of galaxies that surround us.

4. Luminosity

The typical total rest-frame luminosity of galaxies can be estimated from the mean parameters of the exponential fits to their photometric profiles determined in Section 3. For $\mu_0(B) \sim 18^m$ and $h \sim 1$ kpc, the absolute B-band magnitude is equal to $M_B = \mu_0(B) - 5\log h - 38.57 \sim -20.6$. It thus follows that the brightest objects of our sample (just the objects for which we estimated the parameters of photometric profiles) have luminosities similar to that of the Milky Way ($M_B \approx -20.3$) and those of L^*-galaxies (L^* is the characteristic luminosity that enters as a parameter in the Schechter-function fit to the galaxy luminosity function. It is approximately equal to the luminosity of the Milky Way).

We now use the results of Section 2 to determine the mean absolute luminosity for all 22 objects. The mean half-luminosity radius is equal to $\langle r_{1/2}\rangle = 0''.10$, (or 0.53–0.59 kpc for the sets of cosmological parameters considered above), and the mean surface brightness within $r_{1/2}$ is $\langle\mu_{1/2}(I_{814})\rangle = 25.1$. We obtain, after correcting this surface brightness for cosmological dimming and applying zero k-correction, a total rest-frame luminosity of $L_B \sim 10^{10}\,L_{\odot,B}$ or $M_B \sim -19.5$. This estimate agrees with the one we inferred above for the brightest objects of our sample.

We believe, however, that the inferred mean luminosity $M_B \sim -19.5$ is only a lower limit for the true luminosity, because, as is evident from the data in Table 2, many southern-field objects have their estimated $z_{\rm ph} > 6$, and at such redshifts absorption by intervening HI clouds becomes very important even in the I_{814} filter (Madau *et al.* 1996). At $z \geq 6$, the jump in the energy distribution at 1216 $(1+z)$ Å shifts

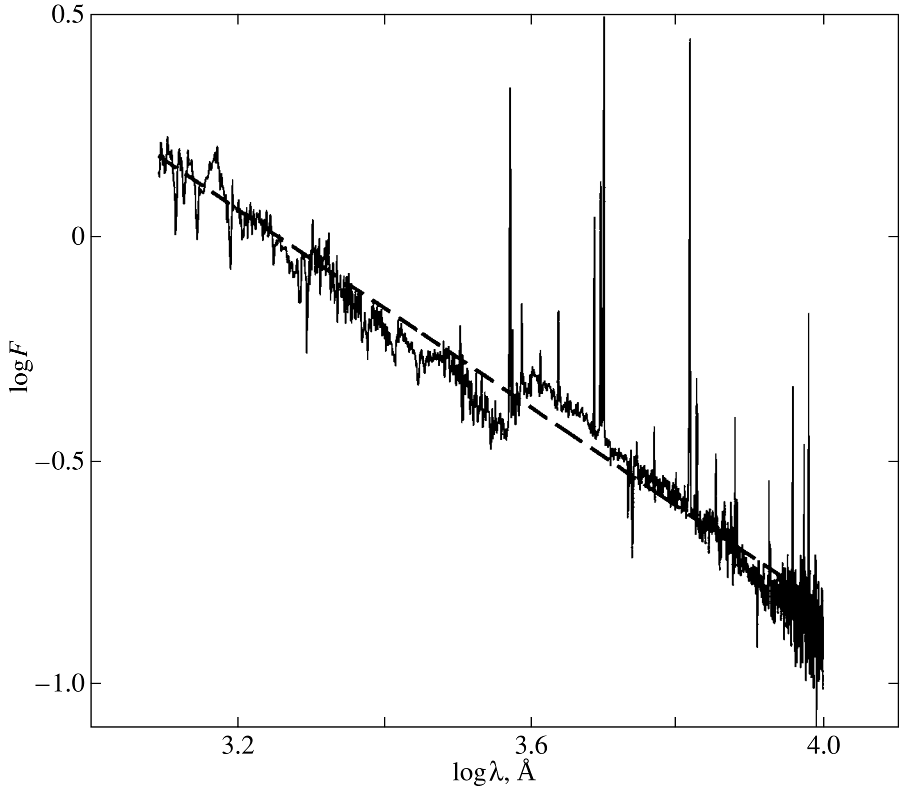

Fig. 5. Relative energy distribution (in const× erg cm^{-2} s^{-1} Å^{-1}) in the spectrum of a starburst galaxy with small internal absorption ($E(B-V) < 0.10$) according to Kinney *et al.* (1996). Dashed line shows the $F(\lambda) \propto \lambda^{-1.1}$ relation.

into the I_{814}-filter band and decreases the observed luminosity. This effect is readily seen in Fig. 6, which shows how estimated M_B vary with $z_{\rm ph}$. Because of observational selection (the Malmquist bias—excess of the number of bright objects in a magnitude-limited sample), the brightest objects should have been identified among the most distant and faint ones. Figure 6 demonstrates the opposite trend: the mean luminosity of galaxies identified among objects with $z \sim 5$–5.5 is close to L^*, and more distant galaxies are significantly less luminous. To correctly estimate the optical luminosities of galaxies with $z \geq 6$, the latter are to be observed at longer wavelengths.

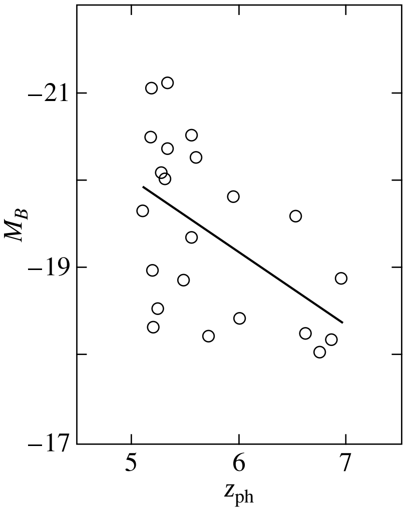

Fig. 6. B-band rest-frame absolute magnitudes of sample galaxies as a function of photometric redshift. Straight line shows the linear fit to the data.

The galaxies with $z_{\rm ph} = 5$–7 identified in deep fields must therefore be L^*-galaxies (like many LBGs at smaller z).

5. Spectral Energy Distribution

Figure 7 shows the averaged (rest-frame) spectral energy distribution normalized to 2000 Å for objects of our sample that have $z_{\rm ph} < 6$. The two solid lines show real distributions for starburst galaxies with different dust content (Kinney *et al.* 1996). The dashed line shows a model energy distribution for a single 5×10^8 yr old star formation burst. We computed this model using the PEGASE.2 package (Fioc and Rocca-Volmerange 1997) and the following parameters: initial mass function of Scalo (1986), zero internal absorption, and zero initial metallicity. It is evident from this figure that at wavelengths >1216 Å, the spectral energy distribution of distant objects agrees

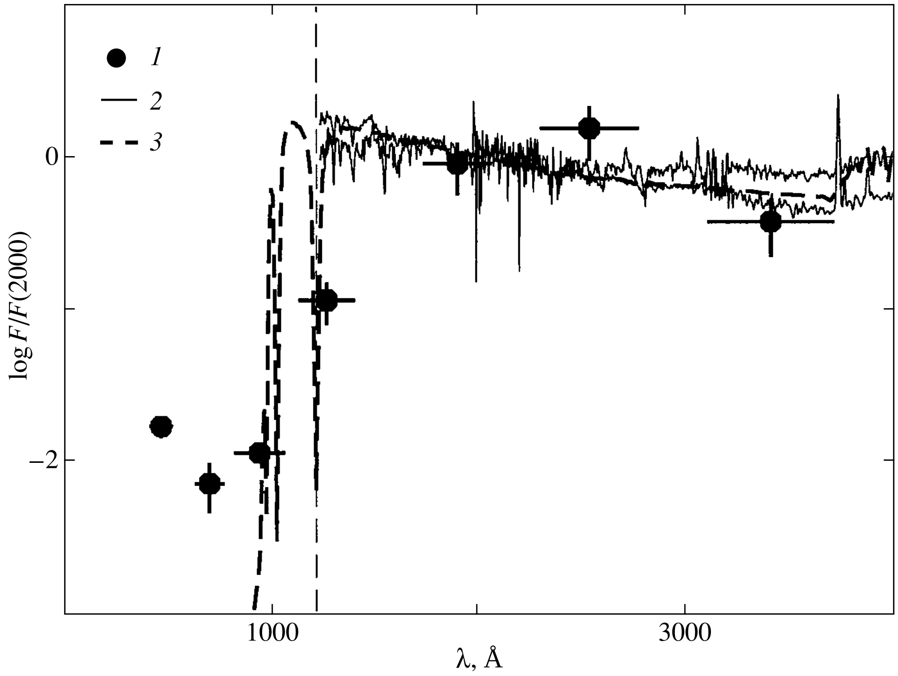

Fig. 7. Averaged spectral energy distribution for galaxies with $z_{\rm ph} = 5$–6 in two deep fields normalized to a wavelength of 2000 Å (*1* and *2*) are the standard distributions for starburst galaxies according to Kinney *et al.* (1996), and (*3*) is the spectral energy distribution for an isolated 5×10^8 yr old starburst. Vertical dashed line indicates the position of wavelength $\lambda = 1216$ Å.

with the flat spectrum typical of galaxies containing a large number of young, short-lived stars, and also with the observed distributions for LBGs at $z \sim 3$ (Papovich *et al.* 2001).

The distribution shown in Fig. 7 can be used to estimate the observed (uncorrected for internal absorption) luminosity of an "average" galaxy with $z =$ 5–6 in the UV-continuum at $\lambda = 1500$ Å ($L_{UV} \sim 10^{29}$ erg/s/Hz). Under certain assumptions, this luminosity can be directly related to star-formation rate. According to the calibration carried out by Madau (1998), the star-formation rate for objects in deep fields is equal to $\mathrm{SFR}_{UV} \approx 30\,M_\odot$/yr (the error can be as high as a factor of three). Our estimate of star-formation rate agrees with those obtained for individual distant galaxies (Spinrad *et al.* 1998; Weymann *et al.* 1998), and also with the parameters of LBGs at $z \sim 3$ (Pettini *et al.* 2001).

The averaged spectral energy distribution decreases abruptly at $\lambda < 1216$ Å. This decrease is due to several causes: (1) the almost complete lack of radiation at λ smaller than the Lyman limit (912 Å) for young O- and B-type stars (Fig. 7); (2) internal absorption in galaxies; and (3) absorption by intervening HI clouds. The jump in the observed spectral energy distribution is usually characterized by parameter D_A ["flux deficit parameter," see Oke and Korycansky (1982)]. For a flat or power-law ($F(\lambda) \propto \lambda^{-1.1}$) spectrum, our averaged distribution yields a $D_A > 0.9$ at $z = 5.4$, which is consistent with more accurate data for the spectra of distant galaxies (Stern and Spinrad 1999).

6. *Space Density*

Assuming that the space density of sample objects does not evolve, i.e., that all galaxies "survive" until the epoch of $z = 0$, one can infer their present-day density $n(z = 0)$. The corresponding estimates are $n(z = 0) = 0.7 \times 10^{-3}$ and 0.4×10^{-3} Mpc^{-3} for the Eistein–deSitter and nonzero Λ-term models, respectively. Given that in the redshift interval $z = 5$–6, our sample is more complete (16 galaxies), the corresponding estimates are equal to 0.8×10^{-3} and 0.6×10^{-3} Mpc^{-3}, respectively. Density $n(z = 0)$ for distant galaxies is thus equal to only a few percent of the total density of galaxies in the local Universe (Marzke *et al.* 1998). The spatial density of bright galaxies ($L \geq L^*$) ($n(z = 0) \sim 0.5 \times 10^{-3}$ Mpc^{-3}) is approximately equal to the number of objects expected to survive since the epoch of $z = 5$–7.

We point out another curious fact. The estimates of the space density of LBG galaxies at $z \sim 3$ are relatively close to those we obtained for galaxies at $z = 5$–7. Thus, Steidel *et al.* (1996b) found that $n(z = 0) = 0.4 \times 10^{-3}$ Mpc^{-3} ($H_0 = 50$ km/s/Mpc,

$\Omega_m = 1.0$, and $\Omega_\Lambda = 0$) for LBGs with $z = 3$–3.5, which differs from the corresponding value for galaxies with $z = 5$–7 by a factor of less than two. Lowental *et al.* (1997) report for starburst galaxies with $z \sim 3$ an estimate of $n(z = 0) \geq 1.1 \times 10^{-3}$ Mpc^{-3} obtained with the same cosmological parameters, in what appears to be comparable to our results.

CONCLUSIONS

We identified a total of 22 galaxies with $z_{\rm ph} = 5$–7 in the northern and southern Hubble Deep Fields. The following are the main features of the objects in our sample:

(1) Morphological peculiarity with the observed asymmetry that consistent with some external gravitational perturbation;

(2) Compact structure with FWHM ∼1 kpc;

(3) Asymmetric brightness distribution [the smoothed brightness distributions can be described by an exponential law in almost half (10 of 22) of the cases];

(4) Very high central disk brightness—$\mu_0(B) \sim 18^m$—in the brightest objects;

(5) The absolute luminosities are, on the average, close to those of L^*–galaxies or somewhat lower;

(6) The averaged spectral energy distribution is consistent with the assumption that the objects are distant starburst galaxies;

(7) The space density of objects observed at $z_{\rm ph} = 5$–7 is comparable to the present-day space density of bright ($L \geq L^*$) galaxies.

All the specific features of distant galaxies mentioned above are very similar to those of LBGs with $z \sim 3$. This similarity leads us to conclude that what we observe at $z_{\rm ph} = 5$–7 are the same LBGs, but perhaps caught at a somewhat earlier stage of evolution (see the Galaxy Sample section for the relative ages of galaxies at different z). Therefore, the population of LBGs already existed by $z \sim 6$, and, if these galaxies contribute substantially to cosmic star formation, the redshift dependence of star formation rate per unit volume of the Universe should not fall off rapidly, at least until $z \sim 6$.

What is the nature of LBGs and galaxies with $z_{\rm ph} = 5$–7? Several models have been suggested to explain the observed properties of LBGs. For instance, they can be bulges of massive galaxies (Giavalisco *et al.* 1996). Or they could have their luminosity and surface brightness decrease as a result of passive photometric evolution to become dwarf elliptical or spheroidal galaxies at $z = 0$ (Lowental *et al.* 1997). Or they could be subgalactic objects similar to those identified by Pascarelle *et al.* (1996), which subsequently produce—via mutual merging—more massive structures.

Detailed observational studies and modeling of a number of LBGs with $z \sim 3$ showed these objects to be relatively compact low-mass ($\sim 10^{10} M_\odot$) metal-poor starburst galaxies (Pettini *et al.* 2001; Papovich *et al.* 2001). Star formation in LBGs might be of recurrent nature (Papovich *et al.* 2001). The properties of LBGs seem to be best described by the "collisional starburst" model (Sommerville *et al.* 2001), where LBGs are assumed to be results of collisions between relatively low-mass objects. Such a scenario naturally arises within the framework of now very popular hierarchical clustering models. Sommerville *et al.* (2001) explain in terms of this model both the principal characteristics (size, star formation rate, color indices) and luminosity functions of the objects studied. It can be assumed, based on the similarity between objects of our sample and LBGs, that what we observe in the two deep fields ($z_{\rm ph} = 5$–7) are galaxies that form as a result of mergings of subgalactic objects, which undergo powerful starbursts and serve as "building blocks" for more massive galaxies.

ACKNOWLEDGMENTS

This work was supported by the Integration program (project A0145).

REFERENCES

1. Ch. J. Conselice, M. A. Bershady, and A. Jangren, Astrophys. J. **529**, 886 (2000).
2. S. Dawson, D. Stern, A. J. Bunker, *et al.*, Astron J. (2001) (in press); astro-ph/0105043.
3. G. de Vaucouleurs and E. Aguero, Publ. Astron. Soc. Pac. **85**, 150 (1973).
4. A. Dey, H. Spinrad, D. Stern, *et al.*, Astrophys. J. Lett. **498**, L93 (1998).
5. H. C. Ferguson, M. Dickinson, and R. Williams, Annu. Rev. Astron. Astrophys. **38**, 667 (2000).
6. A. Fernández-Soto, K. M. Lanzetta, and A. Yahil, Astrophys. J. **513**, 34 (1999).
7. M. Fioc and B. Rocca-Volmerange, Astron. Astrophys. **326**, 950 (1997).
8. A. Fontana, S. D'Odorico, F. Poli, *et al.*, Astron. J. **120**, 2206 (2000).
9. M. Giavalisco, C. C. Steidel, and D. Macchetto, Astrophys. J. **470**, 189 (1996).
10. E. M. Hu, R. G. McMahon, and L. L. Cowie, Astrophys. J. Lett. **522**, L9 (1999).
11. A. L. Kinney, D. Calzetti, R. C. Bohlin, *et al.*, Astrophys. J. **467**, 38 (1996).
12. J. D. Lowental, D. C. Koo, R. Guzman, *et al.*, Astrophys. J. **481**, 673 (1997).
13. P. Madau, Astrophys. J. **441**, 18 (1995).
14. P. Madau, H. C. Ferguson, M. E. Dickinson, *et al.*, Mon. Not. R. Astron. Soc. **283**, 1388 (1996).
15. P. Madau, L. Pozzetti, and M. Dickinson, Astrophys. J. **498**, 106 (1998).

16. R. O. Marzke, L. N. da Costa, P. S. Pellegrini, *et al.*, Astrophys. J. **503**, 617 (1998).
17. J. B. Oke, Astrophys. J., Suppl. Ser. **27**, 21 (1974).
18. J. B. Oke and D. G. Korycansky, Astrophys. J. **255**, 11 (1982).
19. C. Papovich, M. Dickinson, and H. C. Ferguson, Astrophys. J. (2001) (in press); astro-ph/0105087.
20. S. M. Pascarelle, R. A. Windhorst, W. C. Keel, and S. C. Odewahn, Nature **383**, 45 (1996).
21. J. A. Peacock, *Cosmological Physics* (Cambridge Univ. Press, Cambridge, 1999).
22. M. Pettini, A. E. Shapley, Ch. C. Steidel, *et al.*, Astrophys. J. **554**, 981 (2001).
23. B. M. Poggianti, Astron. Astrophys., Suppl. Ser. **122**, 399 (1997).
24. V. P. Reshetnikov, Kinematika Fiz. Nebesnykh Tel **6**, 30 (1990).
25. V. P. Reshetnikov, Pis'ma Astron. Zh. **26**, 563 (2000) [Astron. Lett. **26**, 485 (2000)]; astro-ph/0008220.
26. V. Reshetnikov and F. Combes, Astron. Astrophys., Suppl. Ser. **116**, 417 (1996).
27. J. M. Scalo, Fundam. Cosm. Phys. **11**, 1 (1986).
28. R. S. Somerville, J. R. Primack, and S. M. Faber, Mon. Not. R. Astron. Soc. **320**, 504 (2001).
29. H. Spinrad, D. Stern, and A. Bunker, Astron. J. **116**, 2617 (1998).
30. Ch. C. Steidel, M. Giavalisco, M. Dickinson, and K. L. Adelberger, Astron. J. **112**, 352 (1996a).
31. Ch. C. Steidel, M. Giavalisco, M. Pettini, *et al.*, Astrophys. J. Lett. **462**, L17 (1996b).
32. D. Stern and H. Spinrad, Publ. Astron. Soc. Pac. **111**, 1475 (1999).
33. R. J. Weymann, D. Stern, A. Bunker, *et al.*, Astrophys. J. Lett. **505**, L95 (1998).
34. R. E. Williams, B. Blacker, M. Dickinson, *et al.*, Astron. J. **112**, 1335 (1996).

Translated by A. Dambis

Astronomy Letters, Vol. 28, No. 1, 2002, pp. 12–18. Translated from Pis'ma v Astronomicheskiĭ Zhurnal, Vol. 28, No. 1, 2002, pp. 14–21.
Original Russian Text Copyright © 2002 by Emelyanov, Revnivtsev, Aref'ev, Sunyaev.

A Ten-Year-Long Peak of the X-ray Flux from the Burster 4U 1724–307 in the Globular Cluster Terzan 2: Evolution of the Donor Star or the Influence of a Third Star?

A. N. Emelyanov[1,2,*], **M. G. Revnivtsev**[1,2], **V. A. Aref'ev**[1], and **R. A. Sunyaev**[1,2]

[1]*Space Research Institute, Russian Academy of Sciences,*
Profsoyuznaya ul. 84/32, Moscow, 117810 Russia
[2]*Max-Planck-Institut für Astrophysik, Karl Schwarzschild Strasse 1,*
86740 Garching bei München, Germany

Received August 28, 2001

Abstract—We analyze observations of the burster 4U 1724–307 (1E 1724–3045) in the globular cluster Terzan 2 from 1971 until 2001. Uhuru, OSO-8, Einstein, and EXOSAT observations are used. In addition, we analyze data from the TTM telescope onboard the Mir/Kvant observatory and from the ASM and PCA instruments onboard the RXTE observatory. Based on PCA/RXTE scanning observations, we have mapped the sky in the Galactic-center region. The derived light curve of the burster 4U 1724–307 shows the source to be variable on a time scale of 30 years: over the first 20 years of observations (1970–1990), the source flux was approximately constant, while in the 1990s, it rose over ∼5 years and declined over approximately the same period, approaching its original value. We discuss several scenarios to explain the behavior of the light curve, including the evolution of the mass outflow rate from the donor-star surface, the episodic appearance of a second source in the globular cluster, and gravitational microlensing. As one of the scenarios, we also consider the possibility that the passage of a third star affects the accretion rate in the binary 4U 1724–307. We show that if this event is responsible for the 10-year-long rise in the luminosity of the burster 4U 1724–307, then the size and period of this binary can be estimated.

Key words: *Mir–Kvant observatory; RXTE/TTM, ASM, and PCA instruments; neutron stars, X-ray binaries, globular cluster Terzan 2, 4U 1724–307*

INTRODUCTION

The X-ray burster 4U 1724–307 was discovered in September 1975 when the OSO-8 observatory detected an intense burst from the globular cluster Terzan 2 (Swank *et al.* 1977; Grindlay 1978). At that time, seven bursters [see Grindlay (1977) for a review] were known in globular clusters [more than 85% of the sources in globular clusters are currently believed to be X-ray bursters (In't Zand *et al.* 1999)]. Subsequently, it was found that an X-ray flux from the Terzan 2 region was detected during Uhuru observations back in 1971–1973 (Forman *et al.* 1978). The identification of 4U 1724–307 with the globular cluster Terzan 2 was confirmed by the Einstein observatory (Grindlay *et al.* 1980; the localization accuracy is $\sim1''.5$), which detected a second burst in March 1979. Three more bursts from the source were detected in February 1992 by the ART-P telescope onboard the Granat observatory (Grebenev *et al.* 2002), in August 1996 by the MECS spectrometer onboard the BeppoSAX observatory (Guainazzi *et al.* 1998), and in November 1996 by the RXTE observatory (Molkov *et al.* 2000). Note that the high-angular-resolution observations of 4U 1724–307 by various observatories, Einstein (Grindlay *et al.* 1984), ROSAT (Mereghetti *et al.* 1995), and Chandra (Revnivtsev *et al.* 2001), revealed only one bright source in Terzan 2. The localizations of 4U 1724–307 by these observatories are compatible, within the error limits. The distance to Terzan 2 is assumed to be 6.6 kpc (Barbuy *et al.* 1998).

For 30 years, 4U 1724–307 has been observed in almost all energy bands [see Barret *et al.* (2000) for a review]. Here, we analyze the long-term variability of this source by using data from Uhuru, OSO-8, EXOSAT, Kvant/TTM, and RXTE, which observed it roughly in the same energy band range from 2 to 20 keV during 1973–2001.

---

[*] E-mail: `emelyanov@hea.iki.rssi.ru`

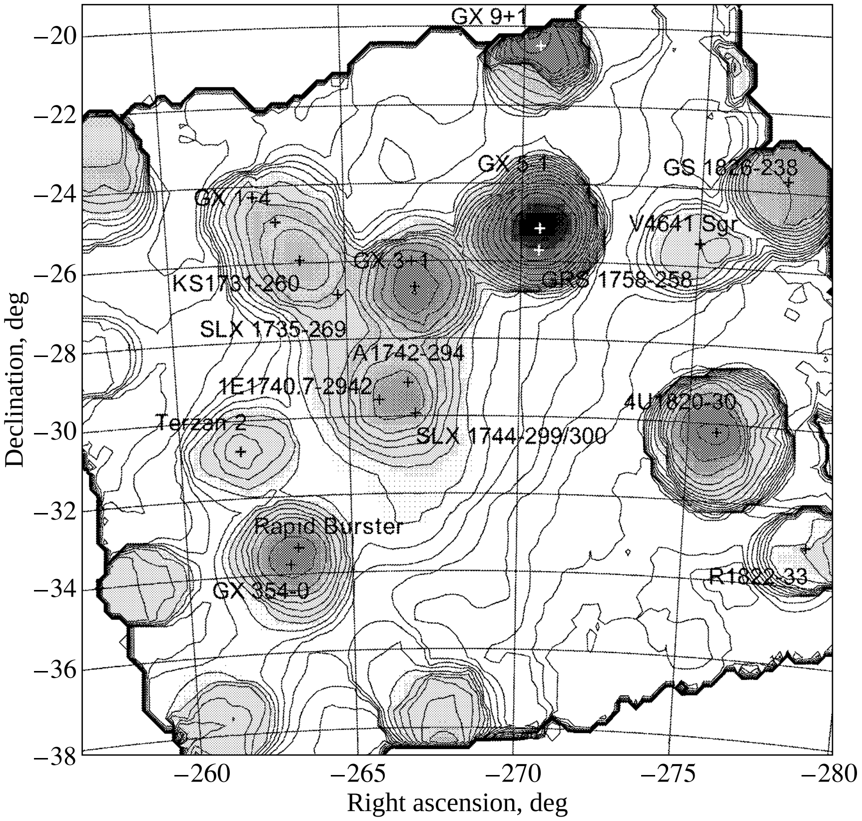

Fig. 1. Image of the sky in the Galactic-center region as constructed from the PCA/RXTE scanning observations in 1999.

OBSERVATIONS

Kvant/TTM

Here, we have performed for the first time a detailed analysis of the observations of the burster 4U 1724−307 with the coded-aperture telescope TTM (Brinkman *et al.* 1985) of the Kvant module docked with the Mir orbiting station. The TTM telescope operated in the energy band 2–30 keV and had a 15° × 15° field of view. Because of the restrictions related to background parameters in the Mir orbit, each TTM observation lasted no more than 26 min ($\lesssim$1.5 ks). The TTM sensitivity depended on the session duration and on the source position within the field of view, being $\sim$5–30 mCrab per session.

From October 21, 1988, until February 24, 1997, the TTM telescope conducted $\approx$130 observing sessions for the Galactic-center region; 4U 1724−307 was within the field of view of the instrument in each session.

RXTE

There are three instruments onboard the RXTE orbiting observatory (Brudt *et al.* 1993): two coaligned spectrometers with a common 1° field of view (PCA and HEXTE) and an all-sky monitor (ASM). ASM monitors the long-period variability of sources in the energy band 1–12 keV with a sensitivity of $\sim$6–10 mCrab per day. PCA has a large effective area ($\sim$6500 cm^2) for a relatively small field of view (1°). This spectrometer has regularly (approximately twice a week) scanned the Galactic-center region since 1999; the errors in the source fluxes per scan are $\sim$2–4 mCrab/scan. Thus, the PCA scanning data for the Galactic center effectively supplement the ASM data. The map of the Galactic-center region obtained by analyzing the PCA scanning observations is shown in Fig. 1. It should also be emphasized that the systematic PCA scanning of the Galactic-center region provides a unique opportunity not only to monitor the long-period variability of sources but also to analyze their spectroscopic variability, because the significance of the PCA X-ray flux is high.

The PCA data were reduced using the LHEASOFT software package. To estimate the background, we used the $L7/240$ model for the PCA scanning observations and the VLE model for the remaining observations. A total of $\sim$300 scanning observations for the Galactic-center region were analyzed; of these we chose those observations in which the source was visible ($\sim$90 observations).

We also analyzed 24 “directed” PCA observations of 4U 1724–307.

When analyzing the ASM light curve, we used data from the Space Research Center of the Massachusetts Institute of Technology (http://xte.mit.edu/).

Other Observatories

The Uhuru, OSO-8, Einstein, and EXOSAT data were taken from publications.

It should be noted that the energy bands for the instruments of the corresponding missions and their fields of view differ markedly. Thus, for example, two counters with $0\overset{\circ}{.}5 \times 5\overset{\circ}{.}2$ and $5\overset{\circ}{.}2 \times 5\overset{\circ}{.}2$ fields of view in the energy band 2–6 keV were used for the Uhuru observatory (Forman *et al.* 1978; Giacconi *et al.* 1971). The OSO-8 observatory used an argon counter ‘B’ (2–20 keV) with a 3° field of view. The Einstein observatory carried out observations with a proportional counter (MPC) whose operating energy range was 1.1–21 keV (Grindlay *et al.* 1980) and the field of view was $1\overset{\circ}{.}5$. The ME (Reynolds *et al.* 1999) and GSPC counters that had equal 45-arcmin fields of views and were sensitive in the energy bands 1–20 and 2–20 keV, respectively, were chosen for EXOSAT observations (the GSPC observational data were taken from the EXOSAT Electronic Archive).

Since the field of view of the recording instrument is large, we cannot accurately determine the flux from 4U 1724–307, i.e., we cannot separate its flux from the total flux from nearby sources, such as GX 354-0, the Rapid Burster, and others. For example, we can only say for the OSO-8 observatory, the persistent flux from 4U 1724–307 did not exceed ∼20 mCrab (Swank *et al.* 1977).

Note also that because of the difference in the energy bands of the instruments used, the source in the same state can have different fluxes expressed in mCrabs. In our case, however, the dependence on the range limits cannot be strong, because the spectrum of 4U 1724–307 is hard and similar to the spectrum of the Crab Nebula (see Barret *et al.* 2000).

The light curve for the burster 4U 1724–307 derived from the data of different observatories is shown in Fig. 2.

DISCUSSION

A characteristic feature of the light curve in Fig. 2 is the broad peak of X-ray activity in the source with maximum light in late 1996–early 1997. In general, the flux variations in Terzan 2 are in the form of a triangle with rise and decline times of ∼5–7 years. As far as we know, this is a unique case of such a smooth long-period variability of a fairly stable X-ray source.

Consider several possible long-period variability mechanisms for 4U 1724–307.

Disk Instabilities and Evolution of the Outflow Rate from the Donor Star?

At present, a universally accepted mechanism for the long-period variability of X-ray sources is the growth of various instabilities in an accretion disk (for example, as the so-called instabilities of dwarf novae) and evolution of the mass outflow rate from the donor-star surface. The mechanism of dwarf novae is unlikely to be realized in our case, because the flux variations in Terzan 2 are not very large, only a factor of 2 or 3, while the disk instabilities lead to variations in the accretion rate by one order of magnitude or more [see Warner (1995) for a review]. However, evolution of the mass outflow rate from the donor-star surface remains a probable cause of the observed 10-year-long variability of 4U 1724–307.

A Second Source in the Globular Cluster?

Another possible mechanism of the observed flux variations in Terzan 2 could be the emergence of a second X-ray source in this globular cluster for ∼10 years other than that observed from OSO-8, Uhuru, Einstein, and EXOSAT in the 1970s and 1980s. This possibility has long been discussed in the literature (Barret and Mereghetti 1993), but as yet nobody has been able to clearly show the presence of two bright X-ray binaries in any globular cluster. Moreover, high-angular-resolution ($0.5''$–$3''$) Einstein (Grindlay *et al.* 1984), ROSAT (Mereghetti *et al.* 1995)[1], and Chandra (Revnivtsev *et al.* 2001) observations of the globular cluster Terzan 2 failed to resolve the bright point-like X-ray source. At a stellar density in the cluster nucleus of 10^4 stars pc^{-3} and a nucleus size of ∼0.15 pc, only one or two stars in the globular cluster can fall within a $1''$ solid angle. Thus, the hypothesis of a second source merged with 4U 1724–307 in the image may be considered to be highly unlikely.

Passage of a Third Star in the Globular Cluster?

Note also the mechanism of the observed 10-year flux variability in Terzan 2 that may be typical only of X-ray sources in globular clusters. Since the stellar density in the nuclei of Galactic globular clusters (including that in the Terzan-2 nucleus) is large (up to 10^4 stars pc^{-3}), the probability for the close passage of two stars (or a third star near a binary) is not negligible (Fabian *et al.* 1975). For a distant (at 1000–10000 binary sizes) passage, the passing star slightly changes the Roche lobe of the donor star in

---

[1] We did not include the ROSAT observations in our complete light curve, because the ROSAT energy band (0.2–2.4 keV) differs greatly from the band we used (2–20 keV).

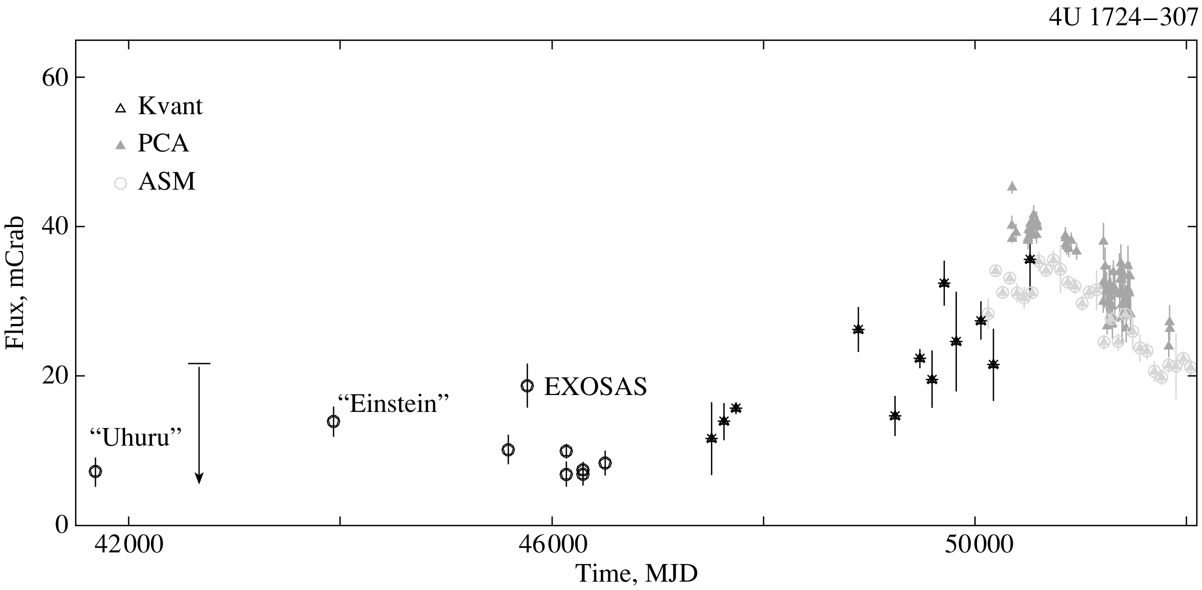

Fig. 2. The complete light curve for 4U 1724−307 constructed from the Uhuru, OSO-8, Einstein, EXOSAT, Kvant/TTM, and RXTE observations between 1973 and 2001.

the binary, which may cause an appreciable increase in the rate of accretion onto the compact object.

Let us obtain an order-of-magnitude estimate of the distance at which a third star must pass to change the mass outflow rate from the donor star by a factor of 2. In general, stars that outflow through the inner Lagrange point overfill their Roche lobes by $\sim$ 0.01–0.05%, i.e., $\Delta r/R \sim (1{-}2) \times 10^{-4}$ (Meyer and Meyer-Hofmeister 1983; Warner 1995). The outflow rate depends on this quantity as $\dot{M} \propto (\Delta r/R)^3$ (Warner 1995). Thus, to change the outflow rate by a factor of 2, we must change the overfilling factor $\Delta r/R$ approximately by a factor of 1.3, i.e., reduce the Roche-lobe radius by $\sim$0.01%. At a mass of the third (passing) star $M \sim M_\odot$, this change in the Roche lobe will be reached for the passage at a distance $\sim(5{-}10) \times 10^3 a$, where a is the binary size [see also Hut and Paczynski (1984) for more accurate calculations].

In the model for the passage of a third star, the time scale of change in the accretion rate in a binary is defined as the time in which the third star traverses a distance that is approximately equal to its distance from the binary. Observations yield a time scale of $\sim$ 10–15 years. The characteristic stellar velocity in the globular cluster Terzan 2 is $v \sim 3.2$ km s^{-1} (Webbink 1985), which gives a characteristic distance of $(1{-}2) \times 10^{14}$ cm. Thus, we can estimate the size of the binary 4U 1724−307, as $a \sim (1{-}2) \times 10^{14}/(5{-}10) \times 10^3 \sim 5 \times 10^{10}$ cm, typical of low-mass X-ray binaries. The assumed period of this binary is then several hours.

Using the calculations by Hut and Paczynski (1984), we constructed a model in which the accretion-rate variations are described by the following parameters: the time of periastron passage, the periastron distance divided by the velocity of the passing star, and the ratio of the binary size to the periastron distance. We fitted the derived light curve for 4U 1724−307 by this model and found the minimum distance between the binary and the third star divided by the passage velocity to be 1009 ±

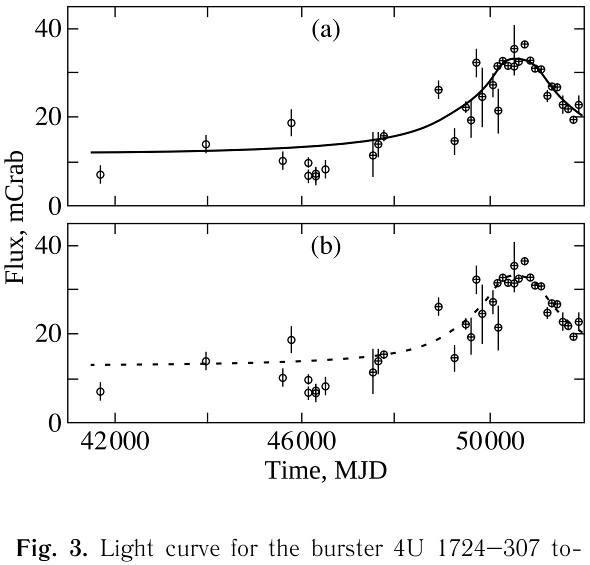

Fig. 3. Light curve for the burster 4U 1724−307 together with various model fits. The solid line in panel (a) represents the dependence of the source's X-ray flux in the model of an increase in the accretion rate due to the passage of a third star; the dotted line in panel (b) represented the source's microlensing light curve.

100 days. At a passing-star velocity of 3.2 km s^{-1}, this distance is $\sim 3 \times 10^{13}$ cm; the binary size is then (1–2) $\times 10^{10}$ cm, and its period is ∼1 hours if the Roche lobe is assumed to be overfilled.

Figure 3a shows experimental points and a model curve. The model curve well reproduces the light-curve shape. Since the third star passes far from the binary, its total effect on the binary is marginal, and all binary parameters after its passage must be close to their initial values. We may assume that if the offered interpretation is correct, then 4U 1724–307 in Terzan 2 will reach ∼10–15 mCrab (i.e., the level that it had before the increase in its intensity) in another ∼5–10 years.

Let us estimate the probability for the passage of a third star at a distance of (3–5) $\times 10^{14}$ cm. The binary free path length relative to the passage of a third star can be roughly defined as $\lambda \sim 1/N\sigma$. Here, N is the stellar density in the globular-cluster nucleus ($N \sim 10^4$ stars $pc^{-3} \sim 4 \times 10^{-52}$ stars cm^{-3}), and σ is the passage cross section, which can be estimated as $\sigma \sim \pi R^2$, $R \sim (3\text{–}5) \times 10^{14}$ cm, i.e., $\sigma \sim (3\text{–}6) \times 10^{29}$ cm^2. We obtain $\lambda \sim (4-9) \times 10^{21}$ cm. The star traverses this distance in $\tau \sim 5 \times 10^8$ years. Thus, over the globular-cluster lifetime ($\sim 10^{10}$ years), a third star passes by each binary several tens of times at a distance of several $\times 10^{14}$ cm. Note, however, that the probability for the passage of some third star by a specific binary (4U 1724–307) precisely during our observing period (∼30 years) is low.

Gravitational Microlensing?

One of the possible formation mechanisms for the 10-year-long peak of the x-ray flux from 4U 1724–307 could be gravitational microlensing. Its effect is to increase the brightness of the background source in the presence of a massive object between the source and the observer. When this massive object moves, the light curve of the background source has a definite shape that depends on the velocity, mass, and trajectory of the lensing object [see Paczynski (1996) for more details].

The possibility of observing gravitational microlensing in our Galaxy was noted 20 years ago (Gott 1981; Canizares 1982). In the last decade, several groups (MACHO, OGLE) have done much work in searching for such events, and more than a thousand microlensing events have been detected to date (Alcock *et al.* 2000).

The light curve of a background star when a gravitational lens (a focusing object) passes through the line of sight can be roughly described by a triangular shape if its brightening is not very large. A more accurate formula was given by Refsdal (1964) and Paczynski (1991). The characteristic flux rise and decline times are determined by the time it takes for the focusing object to traverse the so-called Einstein radius $R_{\rm E}$:

$$R_{\rm E}^2 = \frac{4GMx}{c^2}, \quad x = \frac{D_{\rm l}(D_{\rm s} - D_{\rm l})}{D_{\rm s}},$$

where M is the mass of the lensing object, $D_{\rm l}$ is the distance to the lens, and $D_{\rm s}$ is the distance to the source.

To determine the characteristic parameters for this model, we fitted the derived light curve of 4U 1724–307 by the dependence proposed by Refsdal (1964) and Paczynski (1991) (see Fig. 3b).

The fit yields the time it takes for the lensing object to traverse the Einstein radius, $t = 2100 \pm 300$ days. Using this value, we first concluded that the lens could not be within the globular cluster itself. Indeed, in that case, the distance between the source and the lens is $D_{\rm s} - D_{\rm l} \lesssim 3$ pc (the characteristic size of the globular cluster Terzan 2). The Einstein radius for the assumed mass of the focusing star $M = 1M_\odot$ is $R_{\rm E} \sim 1.3 \times 10^{12}$ cm. At a typical velocity $v \sim 3.2$ km s^{-1} of stars within the globular cluster Terzan 2, we obtain the time scale of change in the flux from 4U 1724–307, $t_{\rm E} \sim 45$ days, which is much shorter than the time $t \sim 2000$ days that we derived from observations. To increase the time scale of flux change in the model that assumes the lens to be located within the globular cluster requires a mass of the focusing object $M \gg 1M_\odot$, which is unlikely for globular clusters.

The travel time scale derived from the model fit is several-fold larger than the maximum time observed previously. So far, the largest known microlensing time scale is $t_{\rm E} \sim 2$ years (to be more precise, 641 days; see Mao 2001). Such a large (as in our case) time scale of change in the flux from the background star implies either a slow motion of the lensing object over the sky or its large mass. If we assume that the mass of this object does not exceed $M \lesssim 5M_\odot$, then we can constrain its transverse velocity. In this case, $R_{\rm E} \lesssim 7 \times 10^{13}$ cm and, hence, the transverse velocity of the lens is $v \lesssim 4$ km s^{-1}.

It should be emphasized that the probability of 4U 1724–307 being microlensed during our observing period is very low. The needed estimates of the microlensing probability are given, for example, in Paczynski (1991) and Alcock (2000). The probability that we see the star at a given time through its microlens (with an arbitrary microlensing time scale) is $P \sim (0.5\text{–}3) \times 10^{-6}$. We also showed that the time scales of flux changes in background stars are distributed through microlensing in such a way that the probability of an event with $t_{\rm E} \gtrsim 1000$ days is several orders of magnitude lower than that for an event with $t_{\mathrm{E}} \sim 30$ days, i.e., $P \lesssim 10^{-7}$.

Thus, we conclude that since such an event is unlikely, interpreting the observed light curve of 4U 1724–307 by gravitational microlensing needs a serious additional justification. One of the possible effects from the passage of a focusing object against the background of a globular cluster is a steady brightening of its stars that happen to be on the passage path. However, the mean time between such "flares" is too large, $\Delta t \gtrsim 2500$ years (the mean distance between globular-cluster stars in the plane of the sky is $\sim\sqrt{1/10^4}$ pc $\sim 3 \times 10^{16}$ cm; at a lens velocity $v \lesssim 4$ km s^{-1}, this distance will be traversed in $\Delta t \gtrsim 3 \times 10^{16}/4 \times 10^5 \sim 7.5 \times 10^{10}$ s).

Note yet another test to see whether the observed change in the luminosity of 4U 1724–307 can be caused by gravitational microlensing. This is the test for a peak X-ray luminosity. If the light from 4U 1724–307 is actually amplified by a microlens, then we can observe X-ray fluxes from the source that significantly exceed the Eddington flux that we calculated without any lens being included. Type-I X-ray bursts with a photospheric expansion have been repeatedly observed from the burster 4U 1724–307, suggesting that the total luminosity of the source must be approximately equal to the Eddington luminosity at the peak X-ray flux. Since mainly helium burns at this time, the Eddington luminosity can be estimated as $L_{\mathrm{X}} \sim 4 \times 10^{38}(M/1.4M_{\odot})$. However, the peak X-ray luminosity recorded during type I bursts (Grindlay *et al.* 1984; Molkov *et al.* 2000) does not exceed this value. Thus, the above reasoning can serve as further evidence against the hypothesis for microlensing of the flux from 4U 1724–307.

CONCLUSIONS

We have analyzed observations of the burster 4U 1724–307 in the globular cluster Terzan 2 by various X-ray observatories over a period of ∼30 years. The derived light curve for this source exhibits an appreciable variability on this time scale. Its characteristic feature is the broad peak of X-ray activity with maximum light in 1996–1997 and a duration of ∼10 years. A combination of the duration and triangular shape and a modest (by a factor of 2) change in the X-ray flux are unusual for X-ray sources. We offered several explanations of the observed light curve. We showed that the brightening in the 1990s could not be associated with the episodic appearance of a second bright X-ray source in the globular cluster. Apart from the intrinsic causes of the observed variability (e.g., evolution of the mass outflow rate from the donor-star surface), we offered two plausible explanations of the observed light curve, which are based on an external impact on the binary. The first involves the passage of a third star at a distance of 10^{14} cm from the binary 4U 1724–307. This passage causes a small change in the Roche lobe of the donor star and, hence, an increase in the accretion rate in the binary. However, the probability of such an event was shown to be low during our observing period (∼30 years), despite the high density of stars in the globular cluster. The other interesting explanation of the observed light curve involves gravitational microlensing. Unfortunately, the probability of such an event is also low. Thus, there may be physical mechanisms at work in the binary that lead to such a light curve.

ACKNOWLEDGMENTS

We wish to thank E.M. Churazov and M.R. Gilfanov, who kindly permitted us to use their TTM data reduction software, without which it would be impossible to obtain TTM scientific information. We are also grateful to S.A. Grebenev for valuable remarks. This study was supported in part by the Russian Foundation for Basic Research (project no. 00-15-96649).

REFERENCES

1. C. Alcock, R. Allsman, D. Alves, *et al.*, Astrophys. J. **541**, 734 (2000).
2. B. Barbuy, E. Bica, and S. Ortolani, Astron. Astrophys. **333**, 117 (1998).
3. D. Barret and S. Mereghetti, Nature **365**, 612 (1993).
4. D. Barret, J. Olive, L. Boirin, *et al.*, Astrophys. J. **533**, 329 (2000).
5. A. Brinkman, J. Dam, W. Mels, *et al.*, *Non-thermal and Very High Temperature Phenomena in X-ray Astronomy,* Ed. by G. C. Perola and M. Salvati (Institute Astronomico, Rome, 1985), p. 263.
6. H. Brudt, R. Rothschild, and J. Swank, Astron. Astrophys., Suppl. Ser. **97**, 355 (1993).
7. C. Canizares, Astrophys. J. **263**, 508 (1982).
8. A. Fabian, J. Pringle, and M. Rees, Mon. Not. R. Astron. Soc. **172**, 15 (1975).
9. W. Forman, C. Jones, L. Cominsky, *et al.*, Astron. Astrophys., Suppl. Ser. **38**, 357 (1978).
10. R. Giacconi, E. Kellog, P. Gorenstein, *et al.*, Astrophys. J. **165**, 27 (1971).
11. J. Gott, Astrophys. J. **243**, 140 (1981).
12. S. A. Grebenev, A. L. Lutovinov, M. N. Pavlinskiĭ, and R. A. Sunyaev, Pis'ma Astron. Zh. (2002) (in press).
13. J. Grindlay, Highlights Astron. **4**, 111 (1977).
14. J. Grindlay, Astrophys. J. Lett. **224**, L107 (1978).
15. J. Grindlay, H. Marshall, P. Hertz, *et al.*, Astrophys. J. Lett. **240**, L121 (1980).
16. J. Grindlay, P. Hertz, J. Steiner, *et al.*, Astrophys. J. Lett. **282**, L13 (1984).

17. M. Guainazzi, A. Parmar, A. Segreto, *et al.*, Astron. Astrophys. **339**, 802 (1998).
18. P. Hut and B. Paczynski, Astrophys. J. **284**, 675 (1984).
19. Sh. Mao, Mon. Not. R. Astron. Soc. (2001) (in press); astro-ph/0108312.
20. S. Mereghetti, D. Barret, L. Stella, *et al.*, Astron. Astrophys. **302**, 713 (1995).
21. F. Meyer and E. Meyer-Hofmeister, Astron. Astrophys. **121**, 29 (1983).
22. S. Mol'kov, S. Grebenev, and A. Lutovinov, Astron. Astrophys. **357**, 41 (2000).
23. B. Paczynski, Astrophys. J. Lett. **371**, L63 (1991).
24. B. Paczynski, Acta Astron. **314**, 419 (1996).
25. S. Refsdal, Mon. Not. R. Astron. Soc. **128**, 295 (1964).
26. M. Revnivtsev, S. Trudolyubov, and K. Borozdin, Astron. Astrophys. (2001) (in press).
27. A. Reynolds, A. Parmar, P. Hakala, *et al.*, Astron. Astrophys., Suppl. Ser. **134**, 287 (1999).
28. J. Swank, R. Becker, E. Boldt, *et al.*, Astrophys. J. Lett. **212**, L73 (1977).
29. B. Warner, in *Cataclysmic Variable Stars* (Cambridge Univ. Press, Cambridge, 1995), Cambridge Astrophysics Series, Vol. 28.
30. R. Webbink, in *Proceedings of the 113th IAU Symposium on Dynamics of Star Clusters, 1985,* p. 541.
31. J. J. M. In't Zand, F. Verbunt, and T. Strohmayer, Astron. Astrophys. **345**, 100 (1999).

Translated by V. Astakhov

Astronomy Letters, Vol. 28, No. 1, 2002, pp. 19–20. Translated from Pis'ma v Astronomicheskiĭ Zhurnal, Vol. 28, No. 1, 2002, pp. 22–24.
Original Russian Text Copyright © 2002 by Revnivtsev, Sunyaev.

Localization of the X-ray Burster KS 1731−260 from Chandra Data

M. G. Revnivtsev[1,2,*] **and R. A. Sunyaev**[2,1]

[1]*Space Research Institute, Russian Academy of Sciences, Profsoyuznaya ul. 84/32, Moscow, 117810 Russia*
[2]*Max-Planck Institut für Astrophysik, Karl Schwarzschild Strasse 1, 86740 Garching-bei-München, Germany*

Received August 7, 2001

Abstract—We analyze Chandra observatory images of the field of the X-ray burster KS 1731−260. A factor of 10 to 15 improvement in the localization accuracy (up to ∼0.6″) has allowed a possible candidate for counterparts of KS 1731−260 to be determined from infrared sky images (Barret *et al.* 1998). The possible counterpart (the sky position difference is ∼1.46″, i.e., less than 2σ) is a 16th magnitude star in the J band. If this star is actually an infrared counterpart of KS 1731−260, then we can estimate its luminosity and the lower limit on the counterpart total luminosity, $L > L_{J,H} \sim 10 L_\odot$. The sharp decline in the X-ray flux from KS 1731−260 in 2001 offers an additional test of whether the proposed candidate is actually a counterpart of KS 1731−260. If the optical and infrared luminosities of this counterpart are largely attributable to reradiation of the X-ray flux from the neutron star, as is the case in low-mass X-ray binaries, then the brightness of the counterpart star must decrease sharply in 2001, after the X-ray source is turned off.

Key words: *Mir–Kvant, TTM, pulsars, neutron stars and black holes, X-ray binaries, KS 1731−260*

INTRODUCTION

The X-ray source KS 1731−260 was discovered by the TTM telescope of the Mir–Kvant observatory in 1988 (Sunyaev 1989; Sunyaev *et al.* 1990). The source has been under the special attention of the Mir–Kvant–TTM team since then. It had exhibited significant X-ray activity for almost ten years after its discovery. The source was repeatedly observed by various X-ray observatories (GINGA, GRANAT, ROSAT, ASCA, RXTE; see, e.g., Barret *et al.* 1998, 2000; Narita *et al.* 2001). Type I X-ray bursts were detected, suggesting that the compact object in the system KS 1731−260 is a neutron star. The X-ray flux from the source in the standard energy band (2–20 keV) was 100–200 mCrab for ∼10 years, which gives an X-ray luminosity $L_X \sim 5 \times 10^{37}$ erg s^{-1} at a distance to KS 1731−260 of about 7–8 kpc (Smith *et al.* 1997). In early 2001, the source flux fell below ∼10 mCrab and seized to be detected by the RXTE instruments (Wijnands *et al.* 2001). Subsequent observations of this sky region by the Chandra observatory revealed a source that coincided in position with KS 1731−260 whose luminosity was $L_X \sim 2 \times 10^{33}$ erg s^{-1} (Wijnands *et al.* 2001). The 12-year-long X-ray light curve for the source constructed from TTM and RXTE/ASM data is given in Aleksandrovich *et al.* (2002).

Since KS 1731−260 is located in the Galactic plane, its optical light undergoes strong absorption. X-ray photoabsorption measurements (Barret *et al.* 1998) give a column density $N_H L \sim 1.2 \times 10^{22}$ cm^{-2}, which corresponds to an optical absorption $A_V \sim 7.2$ (see, e.g., Barret *et al.* 1998). Based on the TTM localization of the source (localization accuracy ∼1′), Cherepashchuk *et al.* (1994) suggested two possible optical counterparts of KS 1731−260. However, subsequent ROSAT observations improved the source position to ∼10″ (Barret *et al.* 1998), which ruled out the association of KS 1731−260 with the candidates proposed by Cherepashchuk *et al.* (1994). Based on their IR observations of the field around KS 1731−260, Barret *et al.* (1988) proposed 13 other candidate for counterparts in the error box of the HRI instrument onboard the ROSAT observatory.

Here, we present the results of our localization of KS 1731−260 using Chandra observations (localization accuracy ∼0.6″) and discuss the properties of a likely IR counterpart of this source.

ANALYSIS OF OBSERVATIONS AND RESULTS

In our analysis, we used the publicly available Chandra observations of KS 1731−260 carried out on March 27, 2001 (total exposure time ∼20 ks). A spectral analysis and a discussion of the spectra are

---

[*] E-mail: `mikej@hea.iki.rssi.ru`

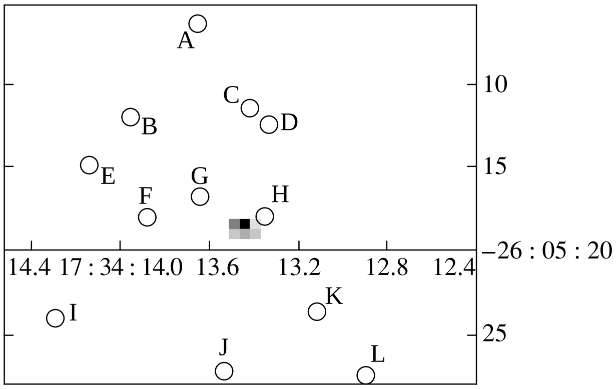

The Chandra image of the sky around KS 1731−260. The letters mark the possible IR candidates for counterparts of KS 1731−260 from Barret *et al.* (1998).

given in Wijnands *et al.* (2001) and Wijnands (2001). The data were analyzed with the standard CIAO 2.1.2 software package.

The expected localization accuracy of X-ray sources by the Chandra observatory was $\sim 1''$. However, an analysis of simultaneous optical and X-ray observations of various sky regions showed that the nominal localization accuracy of sources by the Chandra observatory was about $0.6''$ (see `http://asc.harvard.edu/mta/ASPECT/cel_loc/cel_loc.html` and `http://asc.harvard.edu/mta/ASPECT/celmon/`).

The source KS 1731−260 is clearly seen in the Chandra image of the sky. Its position agrees with the ROSAT position; using the Chandra data, we were able to improve the source position: $\alpha = 17^h34^m13\overset{s}{.}45$, $\delta = -26^\circ05'18\overset{''}{.}7$ (epoch 2000). This improved position allows us to take a fresh look at the list of 13 likely counterparts suggested by Barret *et al.* (1998). The figure shows the Chandra image of the sky. The letters mark the likely counterparts described by Barret *et al.* (1998) (Table 1 in this paper). Based on the new Chandra position, we can reject 12 of the 13 candidates. The only candidate for counterparts that agrees in position with KS 1731−260 at a $\sim 2\sigma$ confidence level is source H with the coordinates $\alpha = 17^h34^m13\overset{s}{.}35$ and $\delta = -26^\circ05'18\overset{''}{.}0$ (epoch 2000). However, because of the relatively large angular distance between KS 1731−260 and its candidate counterpart H ($\sim 1.46''$), further observations of the sky region around this burster are required. If much of the optical luminosity of KS 1731−260 is attributable to the X-ray heating of the companion star and the accretion disk from the neutron star, then after the burster turnoff, which occurred in 2001 (Wijnands 2001), the brightness of the IR counterpart must decrease appreciably. For a low-mass companion of the system, the change in brightness must be larger by three or four magnitudes.

If candidate H from Barret *et al.* (1998) is nevertheless the counterpart of KS 1731−260, we can impose important constraints on the parameters of the binary KS 1731−260. Barret *et al.* (1998) gave the observed brightnesses for all IR candidates, which allows us to estimate the IR luminosity of the possible counterpart. According to Table 1 from the above paper, star H has $m_J \sim 16$ and $m_H \sim 15$. For a distance of 7–8 kpc, these magnitudes correspond to the object's IR luminosity of about $(4\text{–}5) \times 10^{33}$ erg s^{-1}. However, we must also take into account the possible interstellar absorption toward the source. The absorption values derived from X-ray data ($N_H L \sim 1.2 \times 10^{22}$ cm^{-2}) are $A_J \sim 2.0$ and $A_H \sim 1.25$ (Barret *et al.* 1998). Allowance for this absorption increases the derived IR luminosity of the counterpart approximately by a factor of 3 to 6, i.e., $L_{J,H} \sim (0.4\text{–}1) \times 10^{35}$ erg s^{-1}.

When this paper had already been accepted for publication, an Astronomical Telegram appeared (Wijnands *et al.* 2001; ATel 72, `http://atel.caltech.edu`), in which the authors used the same data as we did. Our results are mutually consistent. In their telegram, the authors also report on new IR observations the KS 1731−260 field, which made it possible to exclude the association of star H with the X-ray source.

REFERENCES

1. N. Aleksandrovich, M. Revnivtsev, I. Aref'ev, *et al.*, Pis'ma Astron. Zh. (2002) (in press).
2. D. Barret, C. Motch, and P. Predehl, Astron. Astrophys. **329**, 965 (1998).
3. D. Barret, J. Olive, L. Boirin, *et al.*, Astrophys. J. **533**, 329 (2000).
4. A. Cherepashchuk, V. Goranskii, E. Karitskaya, *et al.*, Astron. Astrophys. **289**, 419 (1994).
5. T. Narita, J. Grindlay, and D. Barret, Astrophys. J. **547**, 420 (2001).
6. D. Smith, E. Morgan, and H. Bradt, Astrophys. J. Lett. **479**, L137 (1997).
7. R. Sunyaev, IAU Circ., No. 4839, 1 (1989).
8. R. Sunyaev, M. Gil'fanov, E. Churazov, *et al.*, Pis'ma Astron. Zh. **16**, 136 (1990) [Sov. Astron. Lett. **16**, 59 (1990)].
9. R. Wijnands, in *Proceedings of the 113th Meeting of the Astronomical Society of the Pacific "The High Energy Universe at Sharp Focus: Chandra Science," Paul, 2001*; astro-ph/0107600.
10. R. Wijnands, J. Miller, C. Markwardt, *et al.*, Astrophys. J. Lett. (2001) (in press); astro-ph/0107380.

Translated by N. Samus'

Astronomy Letters, Vol. 28, No. 1, 2002, pp. 21–23. Translated from Pis'ma v Astronomicheskiĭ Zhurnal, Vol. 28, No. 1, 2002, pp. 25–28.
Original Russian Text Copyright © 2002 by Kuzmin, Losovsky.

Giant Pulses from the Millisecond Pulsar PSR B1937+214

A. D. Kuzmin* **and B. Ya. Losovsky**

Pushchino Radio Astronomy Observatory, Astrospace Center,
Lebedev Physical Institute, Russian Academy of Sciences, Pushchino, Moscow oblast, 142292 Russia

Received August 3, 2001

Abstract—We have detected giant pulses from the millisecond pulsar PSR B1937+214 at the lowest frequency of 112 MHz. The observed flux density at the pulse peak is ∼40 000 Jy, which exceeds the average level by a factor of 600. Pulses of such intensity occur about once per 300 000 periods. The brightness temperature of the observed giant pulses is $T_\mathrm{B} \approx 10^{35}$ K. We estimated the pulse broadening by interstellar scattering to be $\tau_\mathrm{sc} = 3-10$ ms. Based on this estimate and on published high-frequency measurements of this parameter, we determined the frequency dependence of the pulse broadening by scattering: $\tau_\mathrm{sc}(f) = 25 \times (f/100)^{-4.0\pm0.2}$. *© 2002 MAIK "Nauka/Interperiodica".*

Key words: *pulsars, radio emission, giant pulses, scattering*

INTRODUCTION

Giant pulses are short-duration outbursts of pulsar radio emission, a rare phenomenon observed only in the Crab pulsar PSR B0531+21 and in the millisecond pulsar PSR B1937+214.

Giant pulses (GPs) from the millisecond pulsar PSR B1937+214 were detected by Wolszcan *et al.* (1984) at 430 and 1400 MHz both in the main pulse and in the interpulse. GPs with an intensity higher than the noise level by two orders of magnitude were generally encountered once per 400 000 periods. GPs are observed on the trailing edge of the integrated profile, and their width is approximately half the integrated-profile width. Cognard *et al.* (1996) observed a large number (1.7×10^6) of GPs at 430 MHz. About one in 10 000 pulses exceeded the average level by more than a factor of 20. GPs with a factor of 300 excess were encountered. Kinkhabwala and Thorsett (2000) carried out multifrequency studies of GPs from this pulsar. At 430, 1420, and 2380 MHz, the GP width was ≤ 10 μs. The GP spectrum is slightly steeper than the spectrum of its average radio emission.

These measurements were carried out at frequencies above 400 MHz. Giant pulses from the pulsar are difficult to detect and study at low frequencies, because the observed pulse is greatly broadened through interstellar scattering and dispersion broadening.

We have performed observations and detected giant pulses from the millisecond pulsar PSR B1937+214 at the lowest frequency of 112 MHz. Their radio flux density was measured. We estimated the pulse broadening by interstellar scattering and determined the frequency dependence of this parameter.

OBSERVATIONS AND REDUCTION

The observations were carried out from June 14 through July 10, 2001, with the BSA radio telescope at the Pushchino Radio Astronomy Observatory (Astrospace Center, Lebedev Physical Institute, Russian Academy of Sciences). To search for and detect individual pulses, we used the parameters that provided the highest sensitivity and a 128-channel receiver with the channel bandwidth $\Delta f = 20$ kHz. The frequency of the first (highest frequency) channel was 112.680 MHz, the sampling interval was 2.56 ms, and the time constant was $\tau = 3$ ms. The observations were performed in 2030-pulse-long trains. The observing session lasted about 3 min; 36 trains were observed per session. To improve the signal-to-noise ratio, we reduced the data by using a five-point moving average. Over 18 observing sessions containing 1 315 440 individual pulsar pulses, we detected four giant pulses with a signal-to-noise ratio of more than 8 (Fig. 1).

To confirm that they belong to the pulsar PSR B1937+214, we reduced the observational data by breaking down different frequency channels into groups; this reduction revealed a pulse in each group and yielded the expected dispersion delay. The second test involved data reduction by varying the dispersion measure. As one might expect, the dependence of the pulse width on the dispersion measure for the

---

*E-mail: `akuzmin@prao.psn.ru`

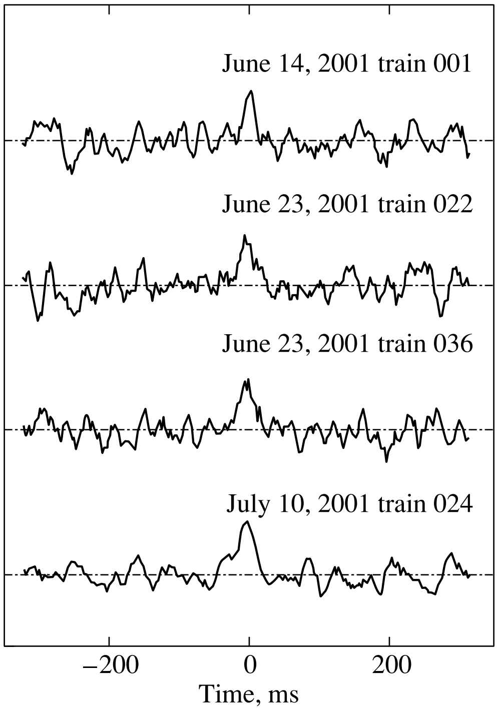

Fig. 1. Fragments of four trains from the pulsar PSR B1937+214 with giant pulses. The pulse time alignment in different trains is arbitrary.

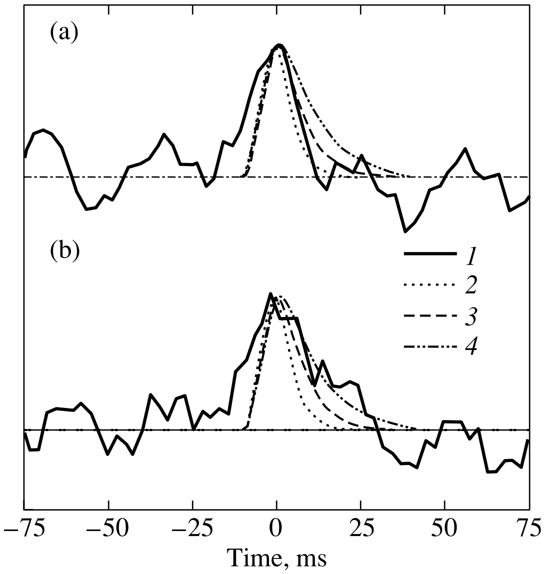

Fig. 2. Comparison of the observed giant pulses from the pulsar (*1*). (a) June 14, 2001 train 01, (b) June 23, 2001 train 23, with model-constructed profiles for various pulse broadenings by scattering: $\tau_{\rm sc} = 3$ ms (*2*), $\tau_{\rm sc} = 6$ ms (*3*), $\tau_{\rm sc} = 10$ ms (*4*).

pulsar has a minimum, while the signal-to-noise ratio has a maximum for data reduction with the nominal dispersion measure $\mathrm{DM} = 71.04$ pc cm^{-3}.

We measured the GP flux density using the method of calibration by the noise measured from discrete sources with known flux densities, in units of radio telescope flux sensitivity δS. The pulsar flux density at the observed pulse maximum $S_{\rm max\ obs}$ was determined from the relation

$$S_{\rm max\ obs} = \delta S / k_{\rm PSR} \times (\Delta F \tau)^{-1/2} \times (S/N),$$

where $k_{\rm PSR} = \sin h_{\rm PSR}$ is the factor that allows for the dependence of the radio telescope effective area on the pulsar elevation h, $\Delta F = 2.56$ MHz is the total bandwidth of the system, $\tau = 3$ ms is the receiver backend time constant, and S/N is the signal-to-noise ratio. In accordance with Kuzmin and Losovsky (2000), δS was represented as

$$\delta S = \delta S_{1000}(a + bT_{\rm bb}),$$

where δS_{1000} is the radio telescope flux sensitivity toward a sky region with the brightness temperature $T_0 = 1000$ K, and $T_{\rm bb}$ is the brightness temperature of the sky background toward the pulsar. The parameter δS_{1000} was taken to be 100 mJy MHz^{-1} s^{-1} (Kutuzov 2000); $a = 0.4$ and $b = 0.0006$ were taken from Kuzmin and Losovsky (2000). The measured flux density at the observed pulse maximum, $S_{\rm max\ obs}$, was recalculated with the conservation of pulse energy at the pulsar GP maximum as $S_{\rm max\ pulse} = S_{\rm max\ obs} \times (w_{\rm 50obs}/w_{\rm 50GP})$, where $w_{\rm 50obs}$ is the observed GP width, and $w_{\rm 50GP}$ is the original GP width. We took $w_{\rm 50GP} = 10$ μs from Kinkhabwala and Thorsett (2000).

Parameters of giant pulses from the pulsar PSR B1937+214

Date of observation	Train N	$S_{\rm max\,obs}$, Jy	$w_{\rm 50obs}$, ms	$S_{\rm max\,pulse}$, Jy
June 14, 2001	01	8.5	30	26 000
June 23, 2001	23	10	42	42 000
June 23, 2001	36	8.5	44	37 000
July 10, 2001	24	10	39	38 000
Mean				38 000
$\sigma_{\rm of\ mean}$				7000

RESULTS

The table lists the observed GP parameters and the measured flux densities. The observed GP width $w_{\rm 50obs}$ is given in milliseconds.

According to extrapolated cataloged data (Taylor *et al.* 1995), the (period-averaged) flux density of this pulsar at 112 MHz is 3.8 Jy, which is 60 Jy at the pulse maximum. Thus, in the four GPs that we observed, the flux density 38 000 Jy exceeds the

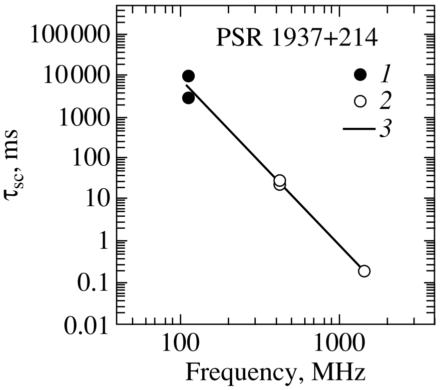

Fig. 3. The frequency dependence of pulse broadening by scattering: (*1*) our measurements; (*2*) the data of Cognard *et al.* (1996) and Kinkhabwala and Thorsett (2000); (*3*) a power-law fit to the frequency dependence $\tau_{\rm sc}(f) = 25 \times (f/100)^{-4.0 \pm 0.2}$.

average level by a factor of ∼600. GPs of such an intensity occur about once per 300 000 periods.

The brightness temperature of giant pulses is

$$T_{\rm B} = S\lambda^2/2k\Omega,$$

where λ is the wavelength of the received radio emission, k is the Boltzmann constant, and Ω is the solid angle of the radio-emitting region. Assuming the size of the radio-emitting region to be $l = cw_{50\rm GP}$, where $w_{50\rm GP} = 10\ \mu$s is the pulse width, c is the speed of light, and the pulsar distance to be $d = 3.6$ kpc (Taylor *et al.* 1995), we obtain for $S_{\rm max\ pulse} = 38\,000$ Jy $T_{\rm B} \approx 10^{35}$ K.

One of the important observational parameters of a pulsar required to determine the properties of the interstellar medium is the frequency dependence of the pulse broadening by scattering, $\tau_{\rm sc}(f)$. Measurements of this dependence over a wide frequency range using normal pulses are limited by the inability to measure them at low frequencies if the broadening by scattering exceeds the pulsar period. Using GPs separated by an interval much larger than the pulsar period makes it possible to measure the broadening by scattering larger than the period.

To determine the pulse broadening by scattering, we compared the observed pulses with the model-constructed pulse profile based on a Gaussian profile with a cataloged width of 0.1 ms (Taylor *et al.* 1995) scattered and dispersed in the interstellar medium for our receiver parameters: the channel bandwidth of 20 kHz and the post-detector RC element with the time constant $\tau = 3$ ms. The broadening by scattering determined from the pulse trailing edge is the sought-for parameter. The best agreement is achieved for a pulse broadening by scattering in the range $\tau_{\rm sc} = 3$–10 ms (Fig. 2).

Figure 3 shows the frequency dependence of the pulse broadening by scattering determined from our measurements and from measurements of this parameter at 430 and 1420 MHz, $\tau_{\rm sc430} = 25$–29 and $\tau_{\rm sc1420} = 0.2$ ms, respectively (Cognard *et al.* 1996; Kinkhabwala and Thorsett 2000). A power-law fit to this dependence corresponds to $\tau_{\rm sc}(f) = 25 \times (f/100)^{-4.0 \pm 0.2}$, where the broadening by scattering $\tau_{\rm sc}$ is in milliseconds, and the frequency f is in MHz. The derived frequency dependence $\tau_{\rm sc}(f)$ agrees with the model of a Gaussian distribution of interstellar inhomogeneities.

A close similarity between the observed GP shapes and the model pattern is a further confirmation that the observed pulses belong to the pulsar.

CONCLUSIONS

We have detected giant pulses from the millisecond pulsar PSR B1937+214 at the lowest frequency of 112 MHz. The observed flux density at the pulse maximum is 40 000 Jy, which exceeds the average level by more than two orders of magnitude. Pulses of such an intensity occur about once per 300 000 periods. The brightness temperature of the observed giant pulses is $T_{\rm B} \approx 10^{35}$ K. The pulse broadening by scattering in the interstellar medium was estimated to be 3–10 ms. We determined the frequency dependence of the pulse broadening by scattering: $\tau_{\rm sc}(f) = 25 \times (f/100)^{-4.0 \pm 0.2}$.

ACKNOWLEDGMENTS

We wish to thank V.V. Ivanova, K.A. Lapaev, and A.S. Aleksandrov for help with the observations and L.B. Potapova for help in preparing the manuscript. The work was supported in part by the Russian Foundation for Basic Research (project no. 01-02-16326).

REFERENCES

1. J. Cognard, J. A. Shrauner, J. H. Taylor, *et al.*, Astrophys. J. Lett. **457**, L81 (1996).
2. A. Kinkhabwala and S. E. Thorsett, Astrophys. J. **535**, 365 (2000).
3. S. M. Kutuzov, private communication (2000).
4. A. D. Kuzmin and B. Ya. Losovsky, Pis'ma Astron. Zh. **26**, 581 (2000) [Astron. Lett. **26**, 500 (2000)].
5. J. H. Taylor, R. N. Manchester, A. G. Lyne, *et al.*, Catalog of 706 Pulsars (1995) (unpublished work).
6. A. Wolszcan, J. M. Cordes, and D. Stinebring, *Millisecond Pulsars,* Ed. by S. P. Reynolds and D. R. Stinebring (Green Bank NRAO, 1984), p. 63.

Translated by G. Rudnitskiĭ

Astronomy Letters, Vol. 28, No. 1, 2002, pp. 24–29. Translated from Pis'ma v Astronomicheskiĭ Zhurnal, Vol. 28, No. 1, 2002, pp. 29–35.
Original Russian Text Copyright © 2002 by Alaverdyan, Arutyunyan, Vartanyan.

A Model of Low-Mass Neutron Stars with a Quark Core

G. B. Alaverdyan, A. R. Arutyunyan[*], and Yu. L. Vartanyan

Yerevan State University, Alex Manoogian ul. 1, Yerevan, 375049 Armenia

Received May 18, 2001; in final form, August 27, 2001

Abstract—We consider an equation of state that leads to a first-order phase transition from the nucleon state to the quark state with a transition parameter $\lambda > 3/2$ ($\lambda = \rho_Q/(\rho_N + P_0/c^2)$) in superdense nuclear matter. Our calculations of integrated parameters for superdense stars using this equation of state show that on the stable branch of the dependence of stellar mass on central pressure ($dM/dP_c > 0$) in the range of low masses, a new local maximum with $M_{\max} = 0.082_{\odot}$ and $R = 1251$ km appears after the formation of a toothlike kink ($M = 0.08M_{\odot}$, $R = 205$ km) attributable to quark production. For such a star, the mass and radius of the quark core are $M_{\rm core} = 0.005M_{\odot}$ and $R_{\rm core} = 1.73$ km, respectively. In the model under consideration, mass accretion can result in two successive transitions to a quark-core neutron star with energy release similar to a supernova explosion: initially, a low-mass star with a quark core is formed; the subsequent accretion leads to configurations with a radius of $\sim$1000 km; and, finally, the second catastrophic restructuring gives rise to a star with a radius of $\sim$100 km. *© 2002 MAIK "Nauka/Interperiodica".*

Key words: *low-mass neutron stars, equations of state for superdense matter*

INTRODUCTION

Given the possible formation of strange quark matter in superdense nuclear plasma (Witten 1984; Farhi and Jaffe 1984), the equation of state for superdense matter assumes the Van der Waals form. In this case, it turns out that, depending on the insufficiently accurate parameters in the strong interaction theory, the energy per baryon ε as a function of the baryon density n can have a negative and positive minimum, $\varepsilon_{\min}$. In turn, this circumstance leads to two alternatives.

For $\varepsilon_{\min} < 0$, a self-bound state of strange quark matter and, as a result, self-confined configurations that are entirely composed of such matter, the so-called "strange stars" studied by Alcock *et al.* (1986), Haensel *et al.* (1986), Kondratyuk *et al.* (1990), Weber and Glendenning (1992), and Vartanyan *et al.* (1995), are possible. For an equation of state with $\varepsilon_{\min} > 0$ and at densities above the threshold for the production of strange quark matter, a first-order phase transition with a density discontinuity takes place. In this case, according to the Gibbs condition (or the Maxwell construction), a thermodynamic equilibrium between the quark matter and the nucleon component is possible; i.e., the two phases coexist. The models with this equation of state have a core composed of strange quark matter and an envelope with the composition of matter of ordinary neutron stars; there is a density discontinuity at the interface.

In many studies, apart from those mentioned above, models of strange stars were computed and comprehensively analyzed (Martem'yanov 1994; Khadkikar *et al.* 1995; Heiselberg and Hjorth-Jensen 1999; and references therein). However, much fewer studies are devoted to configurations with a density discontinuity (Haensel 1986; Carinhas 1993; Alaverdyan *et al.* 1995). Noteworthy are the most complete calculations (Heiselberg *et al.* 1993; Lorenz *et al.* 1993; Glendenning 1997) of models with a mixed phase, which contain various quark configurations in the form of droplet, rodlike, and platelike structures; these models assume continuous pressure and density variations in the quark-phase formation region (Glendenning *et al.* 1992). The results of these authors show that the formation of the mixed phase of quark and nuclear matter may be energetically more or less favorable than an ordinary first-order nucleon-to-quark phase transition, depending on the local surface and Coulomb energies associated with the formation of mixed-phase quark and nuclear structures (Heiselberg *et al.* 1993; Lorenz *et al.* 1993).

Thus, for example, if the interface tension between quark and nuclear matter is sufficiently large, formation of a mixed phase is energetically unfavorable (Heiselberg *et al.* 1993). In this case, there is a first-order phase transition and the two phases coexist.

---

[*] E-mail: `anharutr@ysu.am`

The neutron star will then have a core of pure quark matter and a crust of nuclear matter.

Because of uncertainty in the interface tension of strange quark matter, we presently cannot unambiguously establish which of the above alternatives is actually realized. Below, we consider the case that assumes an interface tension leading to a first-order phase transition with the possible coexistence of the two phases.

To study the functional dependence of the structural and integrated parameters of stellar configurations on the form of the equation of state for superdense matter, we have considered a large set of realistic equations of state that provide the coexistence of neutron matter with strange quark matter. We found that some of these equations of state gave rise to an additional local maximum in the dependence of stellar mass M on central stellar pressure P_c in a low-mass range ($M/M_\odot \approx 0.08$); this provides the possible existence of a new family of stable equilibrium stellar configurations with interesting distinctive features. There is a quark core at the center of such stars, and the stellar radius can reach ∼1000 km, which makes them similar to white dwarfs.

Here, we report our results for one of such equations of state and focus our attention on the low-mass range.

THE EQUATION OF STATE AND CALCULATIONS

The matter density inside a neutron star varies over a wide range, from several g cm^{-3} on the periphery (in the envelope) to 10^{15} g cm^{-3} at the center. At present, there is no unified theory that would faithfully describe the state of such matter with allowance for the formation of all possible constituents over the entire density range. Therefore, different equations of state are commonly used to construct the equation of state for neutron-star matter in different density ranges; of course, continuity is provided when passing from one range to another.

Here, we use the following equations of state for densities below the normal nuclear density:

$$7.86\ \mathrm{g\,cm^{-3}} < \rho < 1.15 \times 10^3\ \mathrm{g\,cm^{-3}}$$

(FMT, Feynman *et al.* 1949),

$$1.15 \times 10^3\ \mathrm{g\,cm^{-3}} < \rho < 4.3 \times 10^{11}\ \mathrm{g\,cm^{-3}})$$

(BPS, Baym *et al.* 1971a).

Beginning from $\rho_{nd} = 4.3 \times 10^{11}$ g cm^{-3}, the matter composition changes, because neutrons are evaporated from nuclei: the so-called *Aen* structure is formed (the matter consists of nuclei, degenerate neutrons and electrons), and the state is described by the equation

$$4.3 \times 10^{11}\ \mathrm{g\,cm^{-3}} < \rho < 2.21 \times 10^{13}\ \mathrm{g\,cm^{-3}}$$

(BBP, Baym *et al.* 1971b).

At subnuclear and supranuclear densities, we used the relativistic equation of state for neutron matter that was calculated by taking into account two-particle correlations based on the Bonn meson-exchange potential (Machleidt *et al.* 1987) and tabulated by Weber *et al.* (1991). We denoted this equation by WGW-Bonn:

$$3.56 \times 10^{13}\ \mathrm{g\,cm^{-3}} < \rho < 4.81 \times 10^{14}\ \mathrm{g\,cm^{-3}}$$

(WGW-Bonn, Weber *et al.* 1991).

These equations of state, which span the density range 7.86 g cm^{-3} $< \rho < 4.81 \times 10^{14}$ g cm^{-3}, describe the matter of a neutron star with a nucleon structure.

To study the phase transition, we must know the dependence of the baryon chemical potential μ_B on pressure P or the function $\varepsilon(n)$ and the dependence of the energy per baryon on baryon density n. To this end, we added the values of the following quantities to the tabulated values of P, ρ, and n:

$$\mu_B(P) = n\frac{\partial(\rho c^2)}{\partial n} - \rho c^2 = \frac{P + \rho c^2}{n}, \qquad (1)$$

$$\varepsilon(n) = \rho c^2/n. \qquad (2)$$

To describe the quark component, we used the quark-bag model developed at the Massachusetts Institute of Technology (MIT) by Chodos *et al.* (1974). According to this model, strange quark matter consists of quarks of three flavors, u, d, and s, and of electrons that are in equilibrium relative to weak interactions. In our equation of state with a density discontinuity, the quark phase is described by phenomenological parameters of the bag model: the quark–gluon interaction constant $\alpha_c = 0.5$, the bag constant $B = 55$ MeV fm^{-3}, and the strange quark mass $m_S = 175$ MeV.

The Gibbs conditions

$$P^{(NM)} = P^{(QM)} = P_0, \qquad (3)$$
$$\mu_B^{(NM)} = \mu_B^{(QM)}$$

yield the pressure P_0, the baryon densities n_N and n_Q, and the mass densities ρ_N and ρ_Q, which characterize the coexistence of the two phases [the superscripts (NM) and (QM) and the subscripts N and Q indicate that the quantities belong to the nucleon and quark phases, respectively].

The parameters of the first-order phase transition can also be determined by the standard Maxwell construction. For the first-order phase transition, the

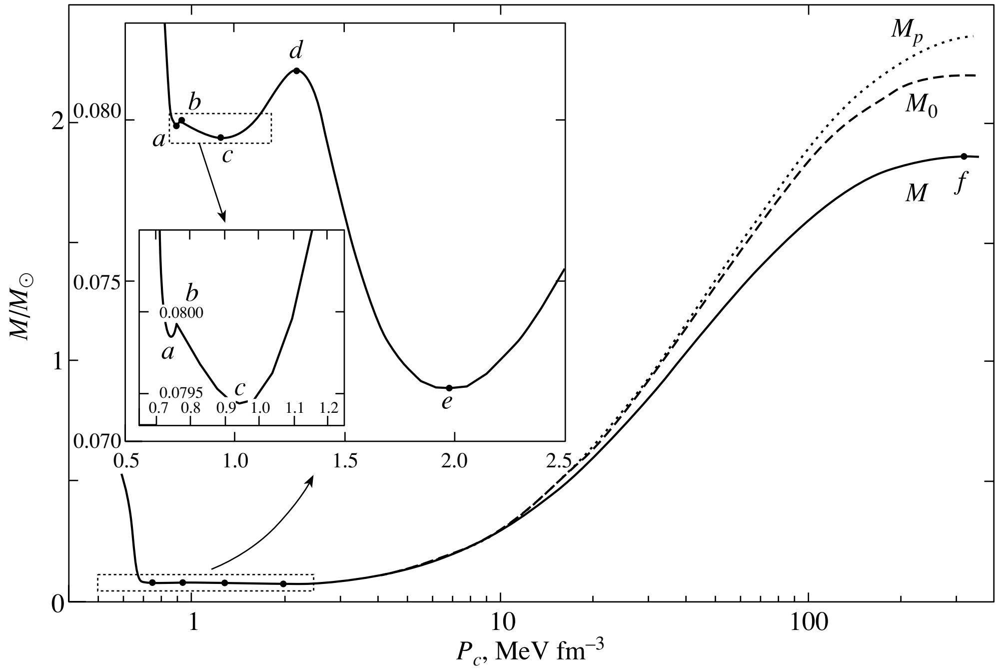

Fig. 1. Total mass M, rest mass M_0, and proper mass M_p versus central pressure. In the upper left corner, the dependence $M(P_c)$ is shown for low masses on an enlarged scale. The symbols *a, b, c, d, e, f* denote critical configurations: *a* corresponds to an ordinary minimum-mass neutron star; *b* corresponds to the quark core formation threshold.

functional dependence of the energy per baryon satisfies the relations (similar to the Gibbs conditions)

$$\frac{\partial\varepsilon^{(NM)}}{\partial(1/n^{(NM)})} = \frac{\partial\varepsilon^{(QM)}}{\partial(1/n^{(QM)})} = -P_0, \qquad (4)$$

$$\varepsilon_Q - \varepsilon_N = P_0\left(\frac{1}{n_N} - \frac{1}{n_Q}\right),$$

$$\varepsilon_{N,Q} = \rho_{N,Q}c^2/n_{N,Q},$$

which correspond to the common tangent in the plot of the energy per baryon ε against $1/n$.

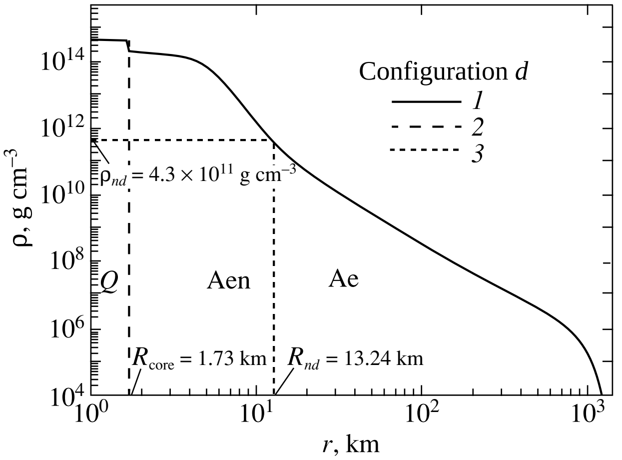

Fig. 2. Matter density ρ (*1*) versus radial coordinate r for configuration *d* (see Fig. 1 and the table); (*2*) the boundary of the strange quark core; (*3*) the *Aen* plasma formation threshold at $\rho_{nd} = 4.3 \times 10^{11}$ g cm^{-3}.

Numerical calculations with this model yielded the following parameters of the first-order phase transition: $P_0 = 0.76$ MeV fm^{-3}, $n_N = 0.12$ fm^{-3}, $n_Q = 0.26$ fm^{-3}, $\rho_N c^2 = 113.8$ MeV fm^{-3}, $\rho_Q c^2 = 250.5$ MeV fm^{-3}.

MODELS OF NEUTRON STARS WITH A CORE OF STRANGE QUARK MATTER (HYBRID STARS): RESULTS AND DISCUSSION

The integrated parameters of a spherically symmetric static superdense star can be determined by numerically integrating the system of relativistic stellar-equilibrium equations (Tolman 1939; Oppenheimer and Volkoff 1939; Zel'dovich and Novikov 1971; Shapiro and Teukolsky 1983) supplemented with the equations for the relativistic moment of inertia (Hartle 1967) for a given equation of state $\rho(P)$ and $\rho_0(P)$ ($\rho_0 = \dfrac{M(^{56}\mathrm{Fe})}{56}n$ is the rest mass density, and n is the baryon number density).

The calculated gravitational mass M, rest mass M_0, and proper mass M_p are plotted against central pressure P_c in Fig. 1. Whereas these curves have an ordinary shape in the maximum-mass range (configuration f), in the low-mass range, where the stability

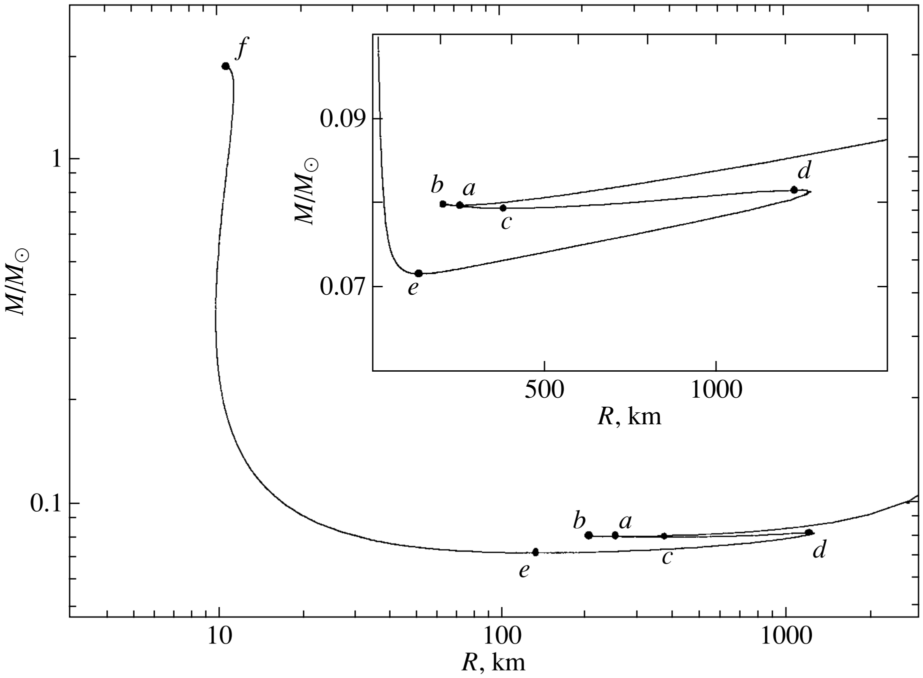

Fig. 3. Mass M of the star versus its radius R. In the upper right corner, the dependence $M(R)$ is shown for small masses on an enlarged scale. The symbols *a, b, c, d, e, f* denote the same configurations as in Fig. 1.

is again lost—the condition $dM/dP_c > 0$ is violated (configuration a)—there are several features that are absent for other equations of state. This range is shown on an enlarged scale in the upper left corner of the figure. Immediately after configuration a, there is a toothlike kink on the curve (configuration b) attributable to the production of quarks. Segment ab corresponds to stable neutron stars without a quark core. The configurations with small quark cores are unstable (segment *bc* of the curve, where $dM/dP_c < 0$). This is consistent with the results of Kaempfer (1981), who showed that if the condition

$$\lambda = \frac{\rho_Q}{\rho_N + P_0/c^2} > 3/2 \qquad (5)$$

is satisfied, the configurations with a low-mass core of the new phase are unstable. In our case, $\lambda = 2.19$, which satisfies the above condition.

In general, when condition (5) is satisfied, the toothlike kink abc takes place on the ascending branch of the curve $M(P_c)$ rather than in the low-mass range, and the curve monotonically rises after configuration c up to the maximum-mass configuration f. In our case, a local maximum is formed immediately after this kink again in the low-mass range—configuration d, for which the radius R exceeds a thousand kilometers and the mass slightly exceeds the mass of configuration b and is equal to $0.082M_\odot$. For this configuration, together with the radius, the moment of inertia I also has a pronounced maximum (see the table and Fig. 5).

The table lists the basic parameters of critical configurations *a, b, c, d, e, f* ($M_{\rm core}$ and $R_{\rm core}$ are the core mass and radius, respectively). Also given here is the packing factor α. For all critical configurations, this quantity is positive and (except for configuration f) of the same order of magnitude as for white dwarfs.

Figure 2 shows a plot of matter density ρ against coordinate r (*1*) for configuration *d*. Curve *2* indicates the boundary of the strange quark core, and curve *3* corresponds to the threshold of neutron evaporation from nuclei (the *Aen* plasma boundary). There is a density discontinuity ($\rho_Q c^2 = 250.5$ MeV fm^{-3}, $\rho_N c^2 = 113.8$ MeV fm^{-3}) at the quark core boundary.

As follows from our calculations, the radial coordinate $R_{nd} = 13.24$ km and the accumulated mass $M_{nd} = 0.07M_\odot$ correspond to the *Aen* plasma formation threshold. This configuration is similar in size to a white dwarf, but the bulk of its mass is concentrated in *Aen* plasma.

Figure 3 shows a plot of the stellar mass M against the stellar radius R. The symbols *a, b, c, d, e, f* denote the same configurations as in Fig. 1. As we see from Fig. 3, the equal-mass stars that correspond to branches *cd* and ef differ greatly in radius. While the stars of branch ef have radii ~10 km, the stars of branch *cd* have large radii ~1000 km, typical of white dwarfs.

Parameters of critical configurations

Configurations	P_c, MeV fm^{-3}	$\frac{M}{M_\odot}$	R, km	$\alpha = \frac{M_0 - M}{M_0}$	I, $M_\odot$ km^2	$\frac{M_{\rm core}}{M_\odot}$	$R_{\rm core}$, km
a	0.74	0.0798	254.7	0.00573	9.99	0	0
b	0.76	0.080	205	0.00597	6.6	0	0
c	0.94	0.079	380	0.00576	25.4	0.001	1.0
d	1.3	0.082	1251	0.00622	861.4	0.005	1.73
e	1.97	0.072	133.2	0.00596	2.4	0.016	2.59
f	321	1.86	10.8	0.15495	94.1	1.85	10.26

In Fig. 4, stellar radius R and quark-core radius $R_{\rm core}$ are plotted against central pressure P_c (*1*). Curve *2* corresponds to neutron stars without quark cores. The dependence of quark-core radius on central pressure is represented by curve *3*; curve *4* shows the distance from the stellar center to the threshold point, where, at $\rho_{nd} = 4.3 \times 10^{11}$ g cm^{-3}, *Aen* plasma is formed through the evaporation of neutrons from nuclei. A pronounced maximum is observed in the region of configuration *d*.

In Fig. 5, the relativistic moment of inertia I is plotted against central pressure P_c.

It should be noted that for the equation of state under consideration, accretion onto a neutron star will lead to two successive jumplike transitions to a quark-core neutron star; as a result, there will be two successive energy releases. First, a quark-core star that belongs to branch cd is formed; the subsequent accretion will lead to configurations with a radius of $\sim$1000 km, and, finally, a star of branch ef with a radius of $\sim$100 km is formed after the second catastrophic restructuring.

To establish whether our result is regular and that the additional (though mildly pronounced) maximum on the $M(P_c)$ curve does not appear by chance, we considered several test equations of state for neutron matter that differ from our equation in a range close to the quark phase formation threshold. Our studies confirmed the regularity of the result and showed that, in some cases, varying the equation of state in the range $9 \times 10^{13} < \rho < 1.8 \times 10^{14}$ g cm^{-3} can even enhance the features found on the $M(P_c)$ curve.

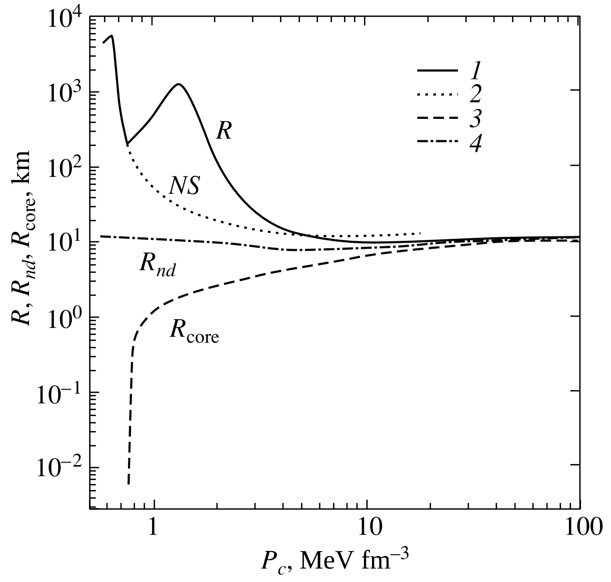

Fig. 4. (*1*) Stellar radius R versus central pressure P_c. Line (*2*) corresponds to ordinary neutron stars without quark cores; line (*4*) represents the P_c dependence of the quark core radius $R_{\rm core}$; and line (*4*) represents the dependence of coordinate R_{nd} that corresponds to the *Aen* plasma formation threshold.

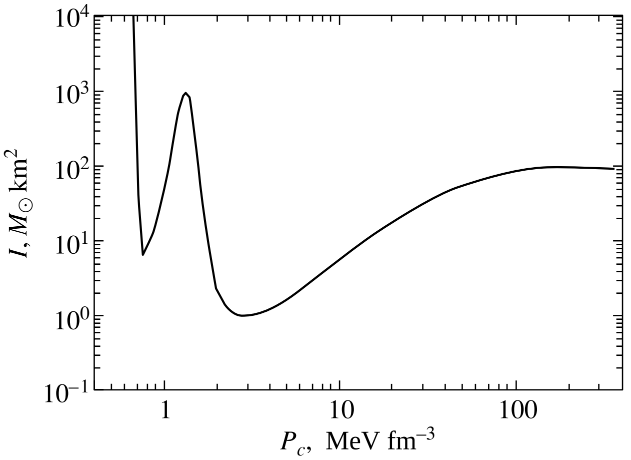

Fig. 5. Relativistic moment of inertia I versus central pressure.

CONCLUSIONS

The first-order phase transition from the nucleon component to the strange quark state with a transition parameter $\lambda > 3/2$ that occurs in superdense nuclear matter generally gives rise to a small tooth-like kink on the stable branch of the dependence of stellar mass on central pressure [curve $M(P_c)$]. In our model, where the loss of stability in the low-mass range (the violation of condition $dM/dP_c > 0$) takes place at higher densities than in other models ($\rho_c = 2 \times 10^{14}$ g cm^{-3}, the table, configuration a) and adjoins the quark production threshold ($\rho_c = 4.5 \times 10^{14}$ g cm^{-3}, the table, configuration b), a new local maximum emerges. This maximum leads to the possible existence of superdense low-mass stars with a radius of more than a thousand kilometers and with a kilometer-size quark core, in which a mere 6% of the total stellar mass is concentrated. Such stars are similar in size to white dwarfs, and the bulk of their mass is concentrated in *Aen* plasma.

ACKNOWLEDGMENT

This study was carried out as part of topic no. 2000-55 supported by the Ministry of Education and Science of the Republic of Armenia.

REFERENCES

1. G. B. Alaverdyan, A. R. Arutyunyan, Yu. L. Vartanyan, and A. K. Grigoryan, Dokl. Akad. Nauk Arm. **95**, 98 (1995).
2. C. Alcock, E. Farhi, and A. Olinto, Astrophys. J. **310**, 261 (1986).
3. G. Baym, C. Pethick, and P. Sutherland, Astrophys. J. **170**, 299 (1971a).
4. G. Baym, H. A. Bethe, and C. J. Pethick, Nucl. Phys. A **175**, 225 (1971b).
5. P. A. Carinhas, Astrophys. J. **412**, 213 (1993).
6. A. Chodos, R. L. Jaffe, K. Johnson, *et al.*, Phys. Rev. D **9**, 3471 (1974).
7. E. Farhi and R. L. Jaffe, Phys. Rev. D **30**, 2379 (1984).
8. R. P. Feynman, N. Metropolis, and E. Teller, Phys. Rev. **75**, 1561 (1949).
9. N. K. Glendenning, Phys. Rev. D **46**, 1274 (1992).
10. N. K. Glendenning, astro-ph/9706236 (1997).
11. P. Haensel, J. L. Zdunik, and R. Schaeffer, Astron. Astrophys. **160**, 121 (1986).
12. J. B. Hartle, Astrophys. J. **150**, 1005 (1967).
13. H. Heiselberg and M. Hjorth-Jensen, nucl-th/9902033 (1999).
14. H. Heiselberg, C. J. Pethick, and E. F. Staubo, Phys. Rev. Lett. **70**, 1355 (1993).
15. B. Kaempfer, Phys. Lett. B **101B**, 366 (1981).
16. S. B. Khadkikar, A. Mashra, and H. Mishra, Mod. Phys. Lett. **10**, 2651 (1995).
17. L. A. Kondratyuk, M. I. Krivoruchenko, and B. V. Martem'yanov, Pis'ma Astron. Zh. **16**, 954 (1990) [Sov. Astron. Lett. **16**, 410 (1990)].
18. C. P. Lorenz, D. G. Ravenhall, and C. J. Pethick, Phys. Rev. Lett. **70**, 379 (1993).
19. R. Machleidt, K. Holinde, and Ch. Elster, Phys. Rep. **149**, 1 (1987).
20. B. V. Martem'yanov, Pis'ma Astron. Zh. **20**, 588 (1994) [Astron. Lett. **20**, 499 (1994)].
21. J. R. Oppenheimer and G. M. Volkoff, Phys. Rev. **55**, 374 (1939).
22. S. L. Shapiro and S. A. Teukolsky, *Black Holes, White Dwarfs, and Neutron Stars: The Physics of Compact Objects* (Wiley, New York, 1983; Mir, Moscow, 1985).
23. R. C. Tolman, Phys. Rev. **55**, 364 (1939).
24. Yu. L. Vartanyan, A. R. Arutyunyan, and A. K. Grigoryan, Pis'ma Astron. Zh. **21**, 136 (1995) [Astron. Lett. **21**, 122 (1995)].
25. F. Weber and N. K. Glendenning, LBL-33066 (1992).
26. F. Weber, N. K. Glendenning, and M. K. Weigel, Astrophys. J. **373**, 579 (1991).
27. E. Witten, Phys. Rev. D **30**, 272 (1984).
28. Ya. B. Zel'dovich and I. D. Novikov, *Gravitational Theory and Stellar Evolution* (Nauka, Moscow, 1971).

Translated by G. Rudnitskiĭ

Astronomy Letters, Vol. 28, No. 1, 2002, pp. 30–33. Translated from Pis'ma v Astronomicheskiĭ Zhurnal, Vol. 28, No. 1, 2002, pp. 36–40.
Original Russian Text Copyright © 2002 by Afonina, Shestakova.

Interferometric Observations of the H II Region Around ξ Per

V. V. Afonina and L. I. Shestakova[*]

Fesenkov Astrophysical Institute, Academy of Sciences of Kazakhstan,
Kamenskoe Plato, Almaty, 480068 Kazakhstan

Received June 21, 2001

Abstract—A Fabry–Perot spectrometer was used to map the H II region around the O star ξ Per in the $H\beta$ emission line. The angular size of the region is $9\overset{\circ}{.}1 \times 6\overset{\circ}{.}0$. The region-boundary contour drawn at the double background level is centered on the star. The accuracy of our emission intensity measurements is 0.2 rayleigh. The proximity of the nebula NGC 1499 has virtually no effect on the measured emission measure toward the star. The star excitation parameter derived from observations corresponds to the spectral type O7.5 III and is $U(\mathrm{Sp}) = 56.0 \pm 8.4$ pc cm^{-2}; the mean electron density in the region is $n_\mathrm{e} = 3.1 \pm 0.4$ cm^{-3}. © *2002 MAIK "Nauka/Interperiodica".*

Key words: *interstellar medium, gaseous nebulae*

INTRODUCTION

The H II region around the O star ξ Per has been repeatedly observed interferometrically in the $H\alpha$ line (Reynolds and Ogden 1982; Reynolds 1988). The region appears highly inhomogeneous, because there is a bright diffuse nebula, NGC 1499 (California Nebula), northeast of it. We undertook this study, because the region had not been mapped and measurements had been carried out only at selected points. We obtained a map of the $H\beta$ emission distribution (see the figure) for eight radial directions from the star at ~45° intervals, at steps of 1° in δ and 5^m in α, which allowed the radius of the ionization zone (r_s) to be determined more accurately. Knowing r_s and the spectral type of the star, we can calculate the mean electron density in the region (n_e) irrespective of the emission intensity toward the star, which may be affected by the nebula NGC 1499.

OBSERVATIONS AND ANALYSIS

We observed the $H\beta$ emission intensity by using a Fabry–Perot spectrometer (Shestakova *et al.* 1990) with a $2\overset{\circ}{.}4$ field of view. Its instrumental profile was within $\delta\lambda_{1/2} = 1\overset{\circ}{.}4$–$1\overset{\circ}{.}6$ Å. The accuracy of our emission intensity measurements was ~20%. The spectrum near $H\beta$ was taken by a pneumatic scanning within 10–20 Å at 0.4 Å intervals and with an accumulation time of 150^s at each point of the spectrum. The measurements were carried out in the direction of the star and its neighborhood within $\alpha = \alpha_0 \pm 40^m$ and $\delta = \delta_0 \pm 7°$, where α_0 and δ_0 are the coordinates of the star. The position of the $H\beta$ emission peak on the pressure scale and the instrumental profile were checked by using a Geissler hydrogen tube. After subtracting the sky background, we reduced the measured emission intensities to zenith at a mean transparency $p \approx 0.8$. Rayleigh was used as the unit of intensity: 1 R = $10^6/4\pi$ phot. cm^{-2} s^{-1} sr^{-1}. Since the energy of the $H\beta$ photon is 4.086×10^{-12} erg, 1 R = 3.252×10^{-7} erg cm^{-2} s^{-1} sr^{-1}. According to Kaplan and Pikel'ner (1979), the $H\beta$ emission intensity is related to the emission measure EM by

$$I(H\beta) = 3 \times 10^{-8} \times 10^4/T \times EM,$$
$$\mathrm{erg\ cm^{-2} s^{-1} sr^{-1}};$$

therefore, 1 R = 7.6 EM for $T = 7000$ K, where EM is in units of pc cm^{-6}. Using the extraatmospheric $H\beta$ flux for the gaseous nebulae NGC 7000 and M 42, we obtained a relationship between this flux and the measured count rate, in counts per second, which can be easily expressed in Rayleighs when the instrumental field of view is completely filled. As in Shestakova *et al.* (1988), the emission measure corrected for interstellar absorption is

$$EM = 7.6(I_0 - I_\mathrm{bg}) \exp(3.3E(B-V)), \quad (1)$$

where $E(B-V)$ is the color excess of the star; I_0 and I_bg are the emission intensities, in Rayleighs, toward the object and the background, respectively. When deriving Eq. (1), we used the standard total-to-selective absorption ratio $R = A_V/E(B-V) = 3.1$ from The *et al.* (1989). The rms value of n_e, in cm^{-3},

---

[*] E-mail: `shest@afi.south-capital.kz`

Parameters of ξ Per

Parameter	Value	References
Sp	O7.5 III (n)(f)	Walborn (1982); Garrison *et al.* (1977)
M_V	$-5\overset{m}{.}1$	Garmany *et al.* (1982); Howarth and Prinja (1989)
m_V	$4\overset{m}{.}03$	Cruz-Gonzalez *et al.* (1974); Bohlin *et al.* (1978)
d	400 pc	Cruz-Gonzalez *et al.* (1974); Bohlin *et al.* (1978)
$T_{\rm eff}$	37 100 K	Chlebowski and Garmany (1991)
$R/R_\odot$	12	Lamers and Leitherer (1993)
$^*U(\rm Sp)$	56.2	Panagia (1973)
$E(B-V)$	$0\overset{m}{.}33$	Diplas and Savage (1994)
A_V	$1\overset{m}{.}02$	The *et al.* (1989) (for standard $R = 3.1$)

and the stellar excitation parameter, in pc cm^{-2}, were determined from the relations

$$n_{\rm e} = (EM/2r_s)^{1/2}, \qquad (2)$$

$$U(\rm Sp) = EM^{1/3}(2r_s)^{2/3}/2.$$

The stellar parameters derived by different authors differ.

Thus, for example, when studying O stars in the $H\alpha$ line using the 15-cm Fabry–Perot spectrometer of the Wisconsin University with a 49′ field of view in the sky and with a radial-velocity resolution of 12 km s^{-1}, Reynolds and Ogden (1982) assumed that the spectral type of the star was O7.5 I, its color excess was $E(B-V) = 0\overset{m}{.}31$, and $d = 400$ pc. They obtained the ionization-zone radius $R_{\rm obs} = 30$ pc and $n_{\rm e} = 0.94$ cm^{-3}. These authors estimated the contribution of the nebula NGC 1499 to the stellar emission. Data on the star were taken from Cruz-Gonzalez *et al.* (1974).

Later, Reynolds (1988) studied the ξ Per region with the same instrument and detected a faint H II region around the star. He believed it to be an O7 III star and assumed that it had a faint outer halo extending to 13° (90 pc east of the star). This author also took into account the influence of the bright nebula NGC 1499. Taking the color excess $E(B-V) = 0\overset{m}{.}36$ and $d = 400$ pc, Reynolds obtained the ionization-zone size of 90 pc and the mean line-of-sight density $n_{\rm e} = 0.5$ cm^{-3}. In addition, based on observations of the pulsar PSR 0320+39, which lies on the line of sight behind the H II region at the distance $d = 880$ pc, and using the dispersion measure DM of the pulsar and the emission measure in its direction, he estimated the electron density of the ionized gas to be $n_{\rm e} = 0.06$ cm^{-3}. However, according to our estimates, the line of sight of the pulsar does not cross the H II region, because the region size is slightly smaller.

Subsequently, several authors estimated the line-of-sight densities of the Galactic interstellar neutral hydrogen by analyzing the interstellar $Ly\alpha$ absorption line toward the hot stars observed with a high resolution from the IUE satellite (Shull and Van Steenberg 1985; Groenewegen *et al.* 1989; Diplas and Savage 1994).

Thus, for example, Shull and Van Steenberg (1985) assumed the spectral type of the star to be O7.5 III (Garmany *et al.* 1982), its color excess to be $E(B-V) = 0\overset{m}{.}36$, and its distance to be $d = 398$ pc. Based on IUE data, these authors surveyed the interstellar densities, abundances, and cloud structure in the Galaxy. Using high-resolution (0.1 Å) spectra, they obtained the line-of-sight densities of the interstellar hydrogen, n(H I) $= 0.93$ cm^{-3}. The authors note that their data agree with the Copernicus results.

Groenewegen *et al.* (1989) analyzed the IUE spectra of early-type stars. They derived the color excess, $E(B-V) = 0\overset{m}{.}35$, by comparing the intrinsic colors of unreddened stars (Schmidt-Kaler 1982) with the observed colors from Garmany *et al.* (1987). The temperature scale and the bolometric corrections were taken from Chlebowski and Garmany (1991), and the masses were determined from evolutionary tracks (Maeder and Meynet 1987) ($T_{\rm eff} = 37\,068$ K, $\log L = 5.32$, $R(R_\odot) = 11$, $\log M = 1.5$, $\log N_{\rm H} = 21.08$, $n_{\rm H} = 0.98$ cm^{-3}). The authors believe that the star evolves away from the main sequence rather than returns from the red supergiant phase; accordingly, they assumed the spectral type of the star to be O7.5 III (n)(f).

Diplas and Savage (1994) determined the line-of-sight densities of the Galactic interstellar neutral hydrogen by analyzing archival data on the interstellar Lyα absorption line toward the 554 B2 or hotter stars observed with a high resolution from the IUE satellite. They give the following parameters for the star: spectral type O7.5 III (n)(f) (Walborn 1972), color excess $E(B-V) = 0\overset{m}{.}33$, distance $d = 398$ pc, and n(H I) $= 0.91$ cm^{-3}.

Lamers and Leitherer (1993) investigated the rates of mass loss from bright Galactic OB stars by using thermal radio emission and $H\alpha$ emission. They

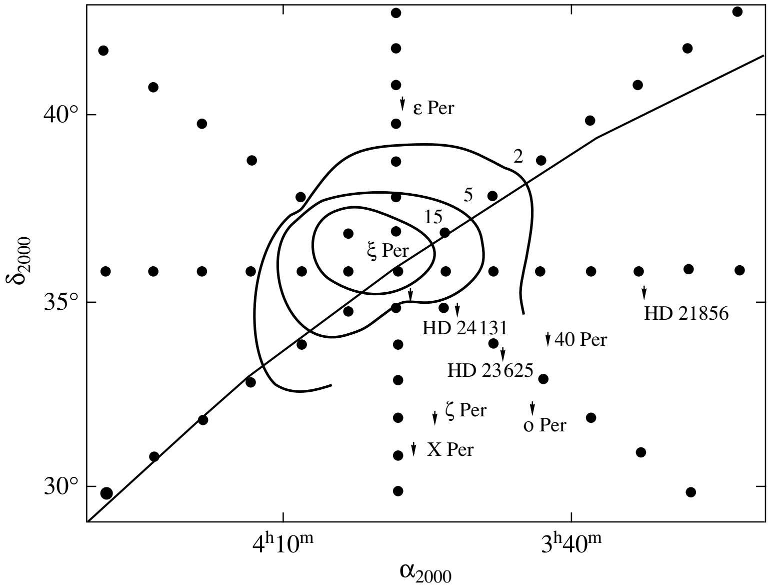

$H\beta$ emission intensity countours (in Rayleighs) in the H II region around the star ξ Per.

took the following parameters for the star: the spectral type O7.5 III (from the catalog by Garmany *et al.* 1987), $T_{\text{eff}} = 37\,100$ K, and bolometric correction BC $= 3.55$ were derived from the relations between these quantities and the spectral type from Chlebowski and Garmany (1991); $M_V = -5.10$ and $d = 400$ pc were taken from the catalog by Garmany *et al.* (1987); $\log L/L_\odot = 5.38$, which is in good agreement with its values from Groenewegen *et al.* (1989). The stellar mass $M/M_\odot = 31$ was determined from evolutionary tracks (Maeder 1990) by using T_{eff} and L. We calculated the radius $R/R_\odot = 12$ from T_{eff} and L and the gravity $\log g_{\text{eff}} = 3.68$ from R and M; the helium abundance 0.18 was taken from Kudritzki *et al.* (1991) and Herrero *et al.* (1992).

Thus, the spectral types determined for ξ Per by different authors slightly differ: O7.5 I, O7.5 III, and O7 III. Uncertainty in the spectral type and luminosity class leads to an inaccurate determination of many other quantities. The spectral-type differences have virtually no effect on the emission measure EM, because the color excess lies within the range $0^m\!.31$–$0^m\!.36$, as determined by different authors for the two luminosity classes. The differences in absolute magnitude M_V can reach more than 1^m, which leads to errors in the photometric distance of the star d and in all the dependent parameters: r_s, U(Sp), and n_{e}.

The table gives the fundamental parameters that we used for ξ Per. The parameter U(Sp) marked by an asterisk was reduced to our assumed $R/R_\odot$ using the data from Panagia (1973). All parameters in the table were reconciled. Since the star ξ Per belongs to the Per OB2 association, its distance is close to our assumed value and corresponds to the distance modulus $m_V - M_V = 8^m\!.0$ corrected for interstellar absorption. In this case, according to Walborn (1972) and Panagia (1973), the star's absolute magnitude must be $5^m\!.5$ for Sp O7.5 III. The corresponding photometric distance is 538 pc (Bohlin *et al.* 1978). The spectral type O7.5 I from Conti and Leep (1974) and from the catalog by Cruz-Gonzalez *et al.* (1974) completely disagrees with the model value of $M_V = -6^m\!.5 \pm 0^m\!.5$ (Panagia 1973; Walborn 1972) and with the corresponding photometric distance, $d = 800 \pm 200$ pc.

RESULTS

The results of our observations for the H II region around ξ Per are the following.

$I_0 - I_{\text{bg}}$	EM, pc cm^{-6}	r_{s}, pc	U(Sp), pc cm^{-2}	n_{e}, cm^{-3}	n_{e} (from r_{s}), cm^{-3}	n_{e} (from EM), cm^{-3}
22.6	510 ± 10.2	26.4 ± 5.3	$56. \pm 8.4$	3.1 ± 0.4	3.1	3.1

The excitation parameter of the star U(Sp)(2) derived from observations is seen to be close to its theoretical value in the table. Since n_{e} calculated using the theoretical U(Sp) and one of the observed parameters, r_s or EM (the last two columns), virtually coincide, we conclude that the effect of the nebula NGC 1499 on the EM value towards the star is marginal.

The results of our measurements of the $H\beta$ emission intensity in the region around the star are shown in the Figure. The circles are the field-of-view centers for those directions in which our measurements were carried out. The circle at the center of the figure is the direction toward ξ Per. The background outside the region is $\sim$1 Rayleigh. The location of the Galactic plane that passes through the star ($b'' = -13\overset{\circ}{.}1$) is indicated; the positions of O–B stars from the Per OB2 association are shown. The region contours at 15 and 5 Rayleigh levels are centered not at the star but at the diffuse gaseous nebula California. The boundary of the H II region drawn at the double background level is symmetric about the star, but it is not closed in the southwest because of the proximity of a group of OB stars. The latter circumstance does not hinder the estimation of r_s for two directions, along and across the Galaxy. We use the mean r_s.

Our results differ greatly from those of the measurements of the H II region around the star that were obtained in $H\alpha$ with a Fabry–Perot spectrometer by Reynolds and Ogden (1982) and Reynolds (1988). Nevertheless, based on the above studies, recalculating the direct emission intensity measurements toward the star yielded EM close to our estimate ($EM \approx 480$ pc cm^{-2}). The difference can be explained by an arbitrary allowance for the contribution of the nebula NGC 1499 by these authors. The presence of a distant halo, as noted by Reynolds (1988), is ruled out, and the faint H II region observed by him can be explained by the influence of the Per OB2 association.

CONCLUSIONS

The hydrogen optical emission in the H II region near ξ Per has been mapped in detail for the first time. The mean electron densities toward the star derived from observations by two different methods are in excellent agreement (almost equal), which suggests a marginal effect of the nebula NGC 1499 on the inferred mean electron densities. The difference between our results and those of Reynolds (1988) can be explained by an arbitrary allowance for the contribution of the nebula NGC 1499.

REFERENCES

1. R. C. Bohlin, B. D. Savage, and J. F. Drake, Astrophys. J. **224**, 132 (1978).
2. T. Chlebowski and C. D. Garmany, Astrophys. J. **368**, 241 (1991).
3. P. S. Conti and E. M. Leep, Astrophys. J. **196**, 113 (1974).
4. C. Cruz-Gonzales, E. Recillas-Cruz, R. Costero, *et al.*, Rev. Mex. Astron. Astrofis. **1**, 211 (1974).
5. A. Diplas and B. D. Savage, Astrophys. J., Suppl. Ser. **93**, 211 (1994).
6. C. D. Garmany, P. S. Gonti, and C. Chiosi, Astrophys. J. **263**, 777 (1982).
7. C. D. Garmany *et al.*, Astron. J. **93**, 1070 (1987).
8. R. F. Garrison, W. A. Hiltner, and R. E. Schild, Astrophys. J., Suppl. Ser. **35**, 111 (1977).
9. M. A. T. Groenewegen, H. J. G. L. M. Lamers, and A. W. A. Pauldrach, Astron. Astrophys. **221**, 78 (1989).
10. A. Herrero, R. P. Kudritzki, J. M. Vilchez, *et al.*, Astron. Astrophys. **261**, 209 (1992).
11. I. D. Howarth and R. K. Prinja, Astrophys. J., Suppl. Ser. **69**, 527 (1989).
12. S. L. Kaplan and S. B. Pikel'ner, *Physics of Interstellar Medium* (Nauka, Moscow, 1979).
13. H. J. G. M. Lamers and C. Leitherer, Astrophys. J. **412**, 771 (1993).
14. A. Maeder, Astron. Astrophys., Suppl. Ser. **84**, 139 (1990).
15. A. Maeder and G. Meynet, Astron. Astrophys. **182**, 243 (1987).
16. N. Panagia, Astron. J. **78**, 922 (1973).
17. R. J. Reynolds, Astron. J. **96**, 670 (1988).
18. R. J. Reynolds and P. M. Ogden, Astron. J. **87**, 306 (1982).
19. T. Schmidt-Kaler, in *Landolt-Bornstein: Numerical Data and Functional Relationships in Science and Technology, New Series,* Ed. by K. Schaifers and H. H. Voigt (Springer-Verlag, Berlin, 1982), Group IV, Vol. 2b, p. 1.
20. L. I. Shestakova, A. S. Kutyrev, and A. Sh. Ataev, Pis'ma Astron. Zh. **14**, 60 (1988) [Sov. Astron. Lett. **14**, 24 (1988)].
21. L. I. Shestakova, A. A. Semenikin, and V. V. Afonina, Pis'ma Astron. Zh. **16**, 1078 (1990) [Sov. Astron. Lett. **16**, 462 (1990)].
22. J. M. Shull and M. E. Van Steenberg, Astrophys. J. **294**, 599 (1985).
23. P. S. Thè, D. de Winter, M. Arens, *et al.*, Astron. Astrophys., Suppl. Ser. **81**, 115 (1989).
24. N. R. Walborn, Astron. J. **77**, 312 (1972).
25. N. R. Walborn, Astron. J. **87**, 1300 (1982).

Translated by N. Samus'

Astronomy Letters, Vol. 28, No. 1, 2002, pp. 34–48. Translated from Pis'ma v Astronomicheskiĭ Zhurnal, Vol. 28, No. 1, 2002, pp. 41–55.
Original Russian Text Copyright © 2002 by Mashonkina, Ryabtsev, Ryabchikova.

Eu III Oscillator Strengths and Europium Abundances in Ap Stars

L. I. Mashonkina[1], **A. N. Ryabtsev**[2], and **T. A. Ryabchikova**[3,4,*]

[1]*Kazan State University, ul. Lenina 18, Kazan, 420008 Tatarstan, Russia*
[2]*Institute of Spectroscopy, Russian Academy of Sciences,*
Troitsk, Moscow oblast, 142092 Russia
[3]*Institute of Astronomy, Russian Academy of Sciences,*
Pyatnitskaya ul. 48, Moscow, 109017 Russia
[4]*Institute of Astronomy, Vienna University, Vienna, Austria*

Received July 3, 2001

Abstract—We present our calculations of the spectrum and oscillator strengths for the $4f^7 - (4f^6 5d + 4f^6 6s)$ Eu III transitions. The calculations were performed with Cowan's RCN–RCG–RCE codes in the single-configuration approximation. A comparison of computed level lifetimes with experimental data for three levels shows that the scale of theoretical oscillator strengths could be overestimated by a factor of 3. The theoretical oscillator strengths of red Eu III lines are two orders of magnitude smaller than their astrophysical oscillator strengths derived by Ryabchikova *et al.* (1999) from the condition of ionization balance. The new oscillator strengths were tested by analyzing the Eu abundance using Eu II and Eu III lines in the spectra of hot peculiar stars (α^2 CVn is a typical representative) and cool peculiar stars (β CrB is a typical representative). First, we computed non-LTE corrections, which proved to be significant for α^2 CVn. We also analyzed the Eu II λ6645.11-Å line as well as ultraviolet and optical Eu III lines. We show that the new oscillator strengths together with the non-LTE corrections allow the contradiction between the Eu abundances derived by Ryabchikova *et al.* (1999) separately from optical Eu II and Eu III lines in α^2 CVn to be resolved. The new Eu abundance, $\log(\mathrm{Eu}/N_{\mathrm{tot}}) = -6.5$, also faithfully describes the blended near-ultraviolet resonance Eu III lines. Using the new Eu III oscillator strengths to analyze the spectrum of the cool Ap star β CrB, we found a significant deviation of the $n(\mathrm{Eu\ II})/n(\mathrm{Eu\ III})$ ratio from its equilibrium value. For a chemically homogeneous model atmosphere, to obtain the observed intensity of the Eu III λ6666.35-Å line, the Eu abundance must be increased by two orders of magnitude compared to that required to describe the Eu II λ6645.11-Å line. We discuss the possibility of explaining the observed intensities of Eu II and Eu III lines in the spectrum of β CrB by the presence of an inhomogeneous atmosphere with Eu concentrated in its uppermost layers. In such atmospheres, the role of non-LTE effects becomes dominant. *© 2002 MAIK "Nauka/Interperiodica".*

Key words: *stars—variable and peculiar*

1. INTRODUCTION

Europium is known to be one of the most anomalous chemical elements in the atmospheres of magnetic peculiar (Ap) stars. Ryabchikova *et al.* (1999) identified and investigated red Eu III lines in several Ap stars. They also determined the Eu abundance from the Eu II λ6645.11-Å line by taking into account magnetic-field effects and hyperfine structure. Using the derived abundances and assuming the hypothesis of local thermodynamic equilibrium (LTE) in the atmospheres of the cooler stars under study to be valid, the authors determined the astrophysical oscillator strengths for four subordinate red Eu III lines. However, using these oscillator strengths to analyze the Eu abundance based on the same lines in the atmosphere of the hot Ap star α^2 CVn, they found a deviation of the ratio $n(\mathrm{Eu\ III})/n(\mathrm{Eu\ II})$ from its equilibrium value. This deviation suggests that the scale of astrophysical oscillator strengths may be incorrect and that there are effects of departures from LTE (non-LTE effects). A nonuniform Eu distribution because of diffusion under radiation pressure in a magnetically stabilized stellar atmosphere (Michaud 1970) cannot be ruled out either.

To test the scale of astrophysical oscillator strengths, we performed theoretical calculations of the Eu III spectrum, whose results are presented in Section 1. In Section 2, we consider non-LTE effects for Eu II and Eu III lines and compute the

---

[*] E-mail: `ryabchik@inasan.rssi.ru`

1063-7737/02/2801-0034$22.00 © 2002 MAIK "Nauka/Interperiodica"

corrections for two stars, α^2 CVn ($T_{\rm eff} = 11500$ K, $\log g = 4.0$) and β CrB ($T = 7750$ K, $\log g = 4.3$), which are typical representatives of the hot and cool Ap stars, respectively. In Section 3, we analyze Eu II and Eu III lines in the spectra of these stars.

2. THEORETICAL CALCULATIONS OF THE Eu III SPECTRUM

We computed the Eu III spectrum by using the RCN–RCG–RCE software package (Cowan 1981). At the first stage, the RCN subroutine determines the wave functions of the specified configurations by the Hartree–Fock single-configuration method with relativistic corrections. These wave functions are used to compute the mean configuration energies, the Slater integrals of intra-configuration electrostatic interactions, the integrals of electric dipole transitions and inter-configuration electrostatic interactions, as well as spin–orbit interaction parameters. Using these quantities, the RCG subroutine computes the wavelengths, transition probabilities, and other characteristics of the spectrum in question. However, the spectrum computed by the Hartree–Fock single-configuration method is known to significantly differ from the experimental spectrum, because some interactions between configurations are disregarded. By fitting the computed and experimental energy levels with the RCE subroutine, the energy-matrix parameters are modified *ab initio*; these parameters are again used by the RCG subroutine to compute a semiempirically refined spectrum. This is the general computational scheme.

The lower levels in doubly ionized europium belong to the 4f^7 configuration with the ^{8}S$_{3.5}$ ground state. The first excited configurations with astrophysically interesting transitions are 4f^{6}5d and 4f^{6}6s. Nine levels that belong to three terms were experimentally measured in the 4f^7 configuration, while in the 4f^{6}5d and 4f^{6}6s configurations, only levels that belong to the parent term 4f^6(^{7}F) were found (Sugar and Spector 1974; Wyart and Bauche-Arnould 1981), which severely limits the number of energy parameters that can be varied when fitting. To estimate the fixed parameters, we computed the 4f^3 and (4f^{2}5d + 4f^{2}6s) configurations in Pr III with the same set of parameters as in Eu III. These configurations have been best studied (Martin *et al.* 1978; Palmeri *et al.* 2000) in doubly ionized lanthanides with the 4f^N ($2 < N < 12$) lower configuration. Fitting their levels yields well-defined energy parameters, which, as their ratio to the *ab initio* Hartree–Fock values, change only slightly in the second and third lanthanide spectra (Wyart 1978; Wyart and Bauche-Arnould 1981) and which can be reliably extrapolated from Pr III to Eu III.

Table 1 presents our fitting results for Eu III levels in comparison with the Hartree–Fock calculations. Since three terms are known in the 4f^7 configuration, we varied the following electrostatic parameters: the mean energy E$_{\rm mean}$4f^7 and Slater parameter F^2(4f, 4f), as well as parameters F^4(4f, 4f) and F^6(4f, 4f); the latter are related as the corresponding Hartree–Fock values. The effective parameters α and β, which describe interactions with remote configurations, were fixed at extrapolated values. In the 4f^{6}5d and 4f^{6}6s configurations, we fixed all the electrostatic parameters that belong to the 4f^6 core and the interaction integrals R^2(4f5d, 4f6s) and R^3(4f5d, 6s4f). Apart from the spin–orbit parameters, we varied the electrostatic parameters that describe the 4f–5d and 4f–6s interactions; to increase the fitting reliability, some of them were coupled by the above method. The final rms deviations of the computed energy levels from their experimental values were 24 and 154 cm^{-1} for the 4f^7 and 4f^6(5d + 6s) configurations, respectively.

Table 2 gives Eu III energy levels (if the level is unknown, its computed values are given in parentheses), Lande factors g, and the first two components in the wave function computed in the LS-coupling approximation. The list of even levels is limited by the three lower known terms; the odd levels are limited by the energy 53000 cm^{-1}.

Table 3 presents the results of our spectrum calculations for transitions between these energy levels. For each transition, the table gives lower- and upper-level energies with five significant figures, level designations, wavelengths, the transition probabilities g_uA, and the logarithm of oscillator strength $\log g_l f$ (g_l and g_u are the statistical weights of the lower and upper levels). The wavelengths were computed from the listed energy levels. If a given transition was known, its wavelength was taken from Sugar and Spector (1974) and it is marked by the letter S. Table 3 contains only those lines for which the transition probabilities g_uA exceed 10^4 s^{-1}. The level designations correspond to the first component of the wave function in Table 2. In several cases, they are ambiguous. For example, the 5d levels with $J = 2.5$ and $E = 39769$ and 40898 cm^{-1} have (^{7}F)^{8}P with contributions of 47 and 48%, respectively, as the first component. Indicating the energy level along with the level designation eliminates this ambiguity.

The measured level lifetimes of the 5d ^{8}P term (Zhang *et al.* 2000) can be used to estimate the possible computational error of the transition probabilities. The experimental values are 65 ± 7, 46 ± 5, and 36 ± 4 ns, while the corresponding computed values are 24, 15, and 11 ns. The ratio of the experimental and computed values is 3.0 ± 0.3. Thus, the relative

Table 1. Semiempirical (SE) and Hartree–Fock (HF) parameters (cm^{-1}) of the 4f^7 and 4f^{6}5d + 4f^{6}6s Eu III configurations and their ratios

Parameter	SE	HF	SE/HF	
$E_{mean}4f^7$	79250(82)	96402	17151*	–
F^2(4f,4f)	85590(390)	104872	0.816	–
F^4(4f,4f)	54688(185)	65418	0.836	r1
F^6(4f,4f)	39255(133)	46956	0.836	r1
α(4f)	30	0	–	f
β(4f)	−900	0	–	f
ζ(4f)	1107(32)	1294	0.856	–
$E_{mean}4f^6 5d$	103559(42)	106580	3023*	–
F^2(4f,4f)	84435	112625	0.750	f
F^4(4f,4f)	60043	70639	0.850	f
F^6(4f,4f)	43191	50813	0.850	f
α(4f)	20	0	–	f
ζ(4f)	1305(22)	1405	0.927	–
ζ(5d)	1025(41)	983	1.041	–
F^2(4f,5d)	19796(215)	25828	0.767	r2
F^4(4f,5d)	9528(103)	12422	0.767	r2
G^1(4f,5d)	8270(79)	11893	0.695	r3
G^3(4f,5d)	6630(64)	9535	0.695	r3
G^5(4f,5d)	5034(48)	7239	0.695	r3
$E_{mean}4f^6 6s$	110309(77)	114213	3901*	–
F^2(4f,4f)	84949	113265	0.750	f
F^4(4f,4f)	60411	71072	0.850	f
F^6(4f,4f)	43463	51133	0.850	f
α(4f)	20	0	–	f
ζ(4f)	1319(33)	1410	0.937	–
G^3(4f,6s)	2073(98)	2770	0.745	–
R^2(4f5d,4f6s)	−239	−281	0.850	f
R^3(4f5d,6s4f)	1819	2141	0.850	f

Note. *The differences SE–HF are given for the mean configuration energies; r1, r2, and r3 are the parameters that are related to the Hartree–Fock ratios during the fitting; f is a fixed parameter during the fitting.

lifetimes of these three levels agree with the measurements, within the experimental error limits. It should be noted that the level compositions significantly differ, 42084 cm^{-1} ($J = 4.5$)—94% ^{8}P, 40870 cm^{-1} ($J = 3.5$)—72% ^{8}P, while the complex situation with $^8P_{2.5}$ has already been discussed above. This example, along with the available computational experience, leads us to conclude that the relative transition probabilities (oscillator strengths) computed in the approximation under consideration must be highly accurate. Because of inadequate allowance for correlations and, possibly, because of the neglect of core polarization (Quinet *et al.* 1999), the absolute transition probabilities could be overestimated by a factor of 3.

Table 2. Level energies for the $4f^7$ and $4f^6(5d + 6s)$ Eu III configurations

E, cm^{-1}	$E - E_{\text{theor}}$, cm^{-1}	g	Configuration	J	Composition
Even levels					
0.00	0	1.996	$4f^7$	3.5	98% $4f^7\,(^8S)\,^8S$ 2% $4f^7\,(^6P)\,^6P$
28200.06	−23	1.688	$4f^7$	3.5	81% $4f^7\,(^6P)\,^6P$ 10% $4f^7\,(^6D)\,^6D$
28628.54	23	1.852	$4f^7$	2.5	88% $4f^7\,(^6P)\,^6P$ 10% $4f^7\,(^6D)\,^6D$
28972.00*	0	2.363	$4f^7$	1.5	93% $4f^7\,(^6P)\,^6P$ 6% $4f^7\,(^6D)\,^6D$
31745.99	31	0.457	$4f^7$	3.5	94% $4f^7\,(^6I)\,^6I$ 3% $4f^7\,(^4H)\,^4H2$
31954.21	−6	0.834	$4f^7$	4.5	96% $4f^7\,(^6I)\,^6I$ 2% $4f^7\,(^4H)\,^4H2$
32073.30	−52	1.291	$4f^7$	8.5	97% $4f^7\,(^6I)\,^6I$ 2% $4f^7\,(^4K)\,^4K1$
32179.55	12	1.037	$4f^7$	5.5	97% $4f^7\,(^6I)\,^6I$ 1 % $4f^7\,(^4H)\,^4H2$
32307.78	−0	1.238	$4f^7$	7.5	98% $4f^7\,(^6I)\,^6I$ 1% $4f^7\,(^4K)\,^4K1$
32314.14	16	1.159	$4f^7$	6.5	98% $4f^7\,(^6I)\,^6I$
Odd levels					
33856.22	171	−0.379	5d	1.5	95% $5d\,(^7F)\,^8H$ 3% $5d\,(^5D)\,^6G1$
34394.41	174	0.692	5d	2.5	95% $5d\,(^7F)\,^8H$ 2% $5d\,(^5D)\,^6G1$
35108.86	177	1.049	5d	3.5	96% $5d\,(^7F)\,^8H$ 2% $5d\,(^5D)\,^6G1$
35627.36	−59	2.586	5d	1.5	51% $5d\,(^7F)\,^8D$ 40% $5d\,(^7F)\,^6P$
35972.13	178	1.211	5d	4.5	96% $5d\,(^7F)\,^8H$ 1% $5d\,(^7F)\,^6H$
36962.29	176	1.298	5d	5.5	96% $5d\,(^7F)\,^8H$ 1% $5d\,(^7F)\,^6H$
37068.00*	0	2.000	5d	2.5	72% $5d\,(^7F)\,^8D$ 20% $5d\,(^7F)\,^6P$
38050.11	−78	1.774	5d	0.5	51% $5d\,(^7F)\,^8F$ 36% $5d\,(^7F)\,^8G$
38067.33	166	1.350	5d	6.5	96% $5d\,(^7F)\,^8H$ 2% $5d\,(^7F)\,^6H$
38229.07	−66	1.795	5d	3.5	90% $5d\,(^7F)\,^8D$ 4% $5d\,(^7F)\,^6P$
38316.66	−66	1.508	5d	1.5	44% $5d\,(^7F)\,^8F$ 41% $5d\,(^7F)\,^8G$
38508.00*	0	0.877	5d	0.5	54% $5d\,(^7F)\,^8G$ 37% $5d\,(^7F)\,^8F$
38828.56	−90	1.498	5d	2.5	43% $5d\,(^7F)\,^8G$ 41% $5d\,(^7F)\,^8F$
39014.36	−2	1.450	5d	1.5	49% $5d\,(^7F)\,^8G$ 41% $5d\,(^7F)\,^8F$
39225.71	−50	1.688	5d	4.5	95% $5d\,(^7F)\,^8D$ 2% $5d\,(^7F)\,^6F$
39289.69	145	1.385	5d	7.5	95% $5d\,(^7F)\,^8H$ 2% $5d\,(^7F)\,^6H$
39574.00	0	2.533	5d	1.5	49% $5d\,(^7F)\,^6P$ 42% $5d\,(^7F)\,^8D$
39579.66	−134	1.485	5d	3.5	46% $5d\,(^7F)\,^8G$ 42% $5d\,(^7F)\,^8F$
39636.88	−10	1.497	5d	2.5	48% $5d\,(^7F)\,^8G$ 41% $5d\,(^7F)\,^8F$
39769.05	−263	2.070	5d	2.5	47% $5d\,(^7F)\,^8P$ 34% $5d\,(^7F)\,^6P$
40133.12	−12	1.626	5d	5.5	94% $5d\,(^7F)\,^8D$ 3% $5d\,(^7F)\,^6F$
40371.65	−13	1.494	5d	3.5	47% $5d\,(^7F)\,^8F$ 46% $5d\,(^7F)\,^8G$
40518.43	−192	1.480	5d	4.5	51% $5d\,(^7F)\,^8G$ 43% $5d\,(^7F)\,^8F$
40659.41	97	1.409	5d	8.5	97% $5d\,(^7F)\,^8H$ 1% $5d\,(^5G)\,^6I1$
40870.60	−225	1.869	5d	3.5	72% $5d\,(^7F)\,^8P$ 21% $5d\,(^7F)\,^6P$
40897.66	−325	2.087	5d	2.5	48% $5d\,(^7F)\,^8P$ 34% $5d\,(^7F)\,^6P$
41159.52	−30	1.497	5d	4.5	52% $5d\,(^7F)\,^8F$ 43% $5d\,(^7F)\,^8G$
41573.22	−230	1.475	5d	5.5	55% $5d\,(^7F)\,^8G$ 39% $5d\,(^7F)\,^8F$
41987.90	−50	1.499	5d	5.5	57% $5d\,(^7F)\,^8F$ 37% $5d\,(^7F)\,^8G$

Table 2. (Contd.)

E, cm^{-1}	$E - E_{\text{theor}}$, cm^{-1}	g	Configuration	J	Composition
42084.25	−239	1.766	5d	4.5	94% 5d (^{7}F) ^{8}P 2% 5d (^{7}F) ^{6}D
42530.91	−276	1.760	5d	3.5	63% 5d (^{7}F) ^{6}P 23% 5d (^{7}F) ^{8}P
42658.20	−224	1.447	5d	6.5	77% 5d (^{7}F) ^{8}G 12% 5d (^{7}F) ^{8}F
42850.07	−68	1.519	5d	6.5	82% 5d (^{7}F) ^{8}F 11% 5d (^{7}F) ^{8}G
43395.75	161	0.308	5d	2.5	89% 5d (^{7}F) ^{6}H 2% 5d (^{5}D) ^{4}G1
43658.96	−152	1.437	5d	7.5	77% 5d (^{7}F) ^{8}G 17% 5d (^{7}F) ^{6}H
43885.27	141	0.842	5d	3.5	88% 5d (^{7}F) ^{6}H 2% 5d (^{7}F) ^{6}G
44553.80	186	1.084	5d	4.5	87% 5d (^{7}F) ^{6}H 2% 5d (^{7}F) ^{6}G
45313.75	222	1.216	5d	5.5	85% 5d (^{7}F) ^{6}H 4% 5d (^{7}F) ^{8}G
45844.00*	0	2.338	5d	0.5	58% 5d (^{7}F) ^{6}D 20% 5d (^{7}F) ^{6}F
45851.00*	0	1.480	5d	1.5	41% 5d (^{7}F) ^{6}D 35% 5d (^{7}F) ^{6}F
46096.40	−8	3.905	6s	0.5	92% 6s (^{7}F) ^{8}F 3% 6s (^{5}D) ^{6}D1
46108.79	−128	1.441	5d	2.5	44% 5d (^{7}F) ^{6}F 33% 5d (^{7}F) ^{6}D
46150.85	234	1.299	5d	6.5	80% 5d (^{7}F) ^{6}H 9% 5d (^{7}F) ^{8}G
46519.26	2	1.976	6s	1.5	93% 6s (^{7}F) ^{8}F 2% 6s (^{5}D) ^{6}D1
46793.38	−110	1.450	5d	3.5	49% 5d (^{7}F) ^{6}F 29% 5d (^{7}F) ^{6}D
47013.00*	0	0.359	5d	0.5	62% 5d (^{7}F) ^{6}F 22% 5d (^{7}F) ^{6}D
47069.87	208	1.357	5d	7.5	72% 5d (^{7}F) ^{6}H 20% 5d (^{7}F) ^{8}G
47173.34	5	1.702	6s	2.5	94% 6s (^{7}F) ^{8}F 2% 6s (^{7}F) ^{6}F
47591.00*	0	1.316	5d	1.5	38% 5d (^{7}F) ^{6}F 38% 5d (^{7}F) ^{6}D
47714.74	−61	1.464	5d	4.5	51% 5d (^{7}F) ^{6}F 30% 5d (^{7}F) ^{6}D
47993.76	6	1.612	6s	3.5	95% 6s (^{7}F) ^{8}F 2% 6s (^{7}F) ^{6}F
48259.62	26	−0.590	6s	0.5	92% 6s (^{7}F) ^{6}F 3% 6s (^{5}D) ^{4}D1
48496.43	198	1.415	5d	2.5	46% 5d (^{7}F) ^{6}D 24% 5d (^{7}F) ^{6}F
48828.91	5	1.050	6s	1.5	90% 6s (^{7}F) ^{6}F 3% 5d (^{7}F) ^{6}G
48925.15	4	1.571	6s	4.5	96% 6s (^{7}F) ^{8}F 2% 6s (^{7}F) ^{6}F
49086.13	−272	1.436	5d	5.5	74% 5d (^{7}F) ^{6}F 15% 5d (^{7}F) ^{6}G
49165.00*	0	0.207	5d	1.5	75% 5d (^{7}F) ^{6}G 11% 5d (^{7}F) ^{6}F
49292.56	263	1.450	5d	3.5	50% 5d (^{7}F) ^{6}D 20% 5d (^{7}F) ^{6}G
49610.81	−58	1.266	6s	2.5	81% 6s (^{7}F) ^{6}F 11% 5d (^{7}F) ^{6}G
49905.64	18	1.036	5d	2.5	58% 5d (^{7}F) ^{6}G 17% 5d (^{7}F) ^{6}F
49925.96	−3	1.548	6s	5.5	97% 6s (^{7}F) ^{8}F 1% 6s (^{7}F) ^{6}F
49956.73	316	1.473	5d	4.5	54% 5d (^{7}F) ^{6}D 18% 5d (^{7}F) ^{6}G
50426.33	−105	1.251	5d	3.5	54% 5d (^{7}F) ^{6}G 17% 5d (^{7}F) ^{6}F
50805.58	54	1.374	6s	3.5	79% 6s (^{7}F) ^{6}F 9% 5d (^{7}F) ^{6}G
50965.29	−13	1.534	6s	6.5	96% 6s (^{7}F) ^{8}F 2% 6s (^{5}G) ^{6}G1
51111.48	62	1.321	5d	4.5	64% 5d (^{7}F) ^{6}G 20% 5d (^{7}F) ^{6}F
51650.07	19	1.358	5d	5.5	74% 5d (^{7}F) ^{6}G 14% 5d (^{7}F) ^{6}F
51848.18	22	1.431	6s	4.5	94% 6s (^{7}F) ^{6}F 2% 6s (^{7}F) ^{8}F
52099.87	183	1.382	5d	6.5	88% 5d (^{7}F) ^{6}G 3% 5d (^{7}F) ^{8}F
52960.08	−7	1.450	6s	5.5	95% 6s (^{7}F) ^{6}F 1% 6s (^{5}G) ^{4}G1

* Unknown levels with theoretical values.

Table 3. Transition probabilities and oscillator strengths for Eu III

Transition	λ, Å	g_u, A	log[$g_l f$]
0 4f^7 ^{8}S$_{3.5}$−49957 5d (^{7}F) ^{6}D$_{4.5}$	2001.084	9.622E+06	−2.233
0 4f^7 ^{8}S$_{3.5}$−49293 5d (^{7}F) ^{6}D$_{3.5}$	2028.051	1.721E+06	−2.969
0 4f^7 ^{8}S$_{3.5}$−47715 5d (^{7}F) ^{6}F$_{4.5}$	2095.123	1.105E+07	−2.139
0 4f^7 ^{8}S$_{3.5}$−46793 5d (^{7}F) ^{6}F$_{3.5}$	2136.381	1.956E+06	−2.875
0 4f^7 ^{8}S$_{3.5}$−42531 5d (^{7}F) ^{6}P$_{3.5}$	2350.512 S	1.493E+08	−0.913
0 4f^7 ^{8}S$_{3.5}$−42084 5d (^{7}F) ^{8}P$_{4.5}$	2375.461 S	8.935E+08	−0.126
0 4f^7 ^{8}S$_{3.5}$−41160 5d (^{7}F) ^{8}F$_{4.5}$	2428.834 S	1.192E+06	−2.978
0 4f^7 ^{8}S$_{3.5}$−40898 5d (^{7}F) ^{8}P$_{2.5}$	2444.382 S	2.273E+08	−0.698
0 4f^7 ^{8}S$_{3.5}$−40871 5d (^{7}F) ^{8}P$_{3.5}$	2445.992 S	5.277E+08	−0.329
0 4f^7 ^{8}S$_{3.5}$−40518 5d (^{7}F) ^{8}G$_{4.5}$	2467.267	9.222E+05	-3.079
0 4f^7 ^{8}S$_{3.5}$−40372 5d (^{7}F) ^{8}F$_{3.5}$	2476.238 S	4.290E+06	−2.404
0 4f^7 ^{8}S$_{3.5}$−39769 5d (^{7}F) ^{8}P$_{2.5}$	2513.759 S	2.471E+08	−0.636
0 4f^7 ^{8}S$_{3.5}$−39637 5d (^{7}F) ^{8}G$_{2.5}$	2522.143 S	6.908E+06	−2.181
0 4f^7 ^{8}S$_{3.5}$−39580 5d (^{7}F) ^{8}G$_{3.5}$	2525.791	2.706E+06	−2.590
0 4f^7 ^{8}S$_{3.5}$−39226 5d (^{7}F) ^{8}D$_{4.5}$	2548.586 S	2.445E+06	−2.624
0 4f^7 ^{8}S$_{3.5}$−38829 5d (^{7}F) ^{8}G$_{2.5}$	2574.653 S	1.902E+06	−2.725
28200 4f^7 ^{6}P$_{3.5}$−51173* 5d (^{7}F) ^{6}G$_{4.5}$	4351.7	4.366E+04	−3.906
28200 4f^7 ^{6}P$_{3.5}$−50426 5d (^{7}F) ^{6}G$_{3.5}$	4497.919	6.473E+04	−3.710
28629 4f^7 ^{6}P$_{2.5}$−50426 5d (^{7}F) ^{6}G$_{3.5}$	4586.336	2.904E+04	−4.043
28200 4f^7 ^{6}P$_{3.5}$−49957 5d (^{7}F) ^{6}D$_{4.5}$	4595.009 S	1.668E+06	−2.263
28200 4f^7 ^{6}P$_{3.5}$−49906 5d (^{7}F) ^{6}G$_{2.5}$	4605.820	1.865E+04	−4.225
28629 4f^7 ^{6}P$_{2.5}$−49906 5d (^{7}F) ^{6}G$_{2.5}$	4698.574	4.218E+04	−3.855
28200 4f^7 ^{6}P$_{3.5}$−49293 5d (^{7}F) ^{6}D$_{3.5}$	4739.696	8.982E+05	−2.507
28629 4f^7 ^{6}P$_{2.5}$−49293 5d (^{7}F) ^{6}D$_{3.5}$	4837.977 S	8.991E+05	−2.491
28200 4f^7 ^{6}P$_{3.5}$−48496 5d (^{7}F) ^{6}D$_{2.5}$	4925.615	2.061E+05	−3.115
28629 4f^7 ^{6}P$_{2.5}$−48496 5d (^{7}F) ^{6}D$_{2.5}$	5031.844	9.663E+05	−2.428
32314 4f^7 ^{6}I$_{6.5}$−52100 5d (^{7}F) ^{6}G$_{6.5}$	5052.739	1.358E+04	−4.276
28972* 4f^7 ^{6}P$_{1.5}$−48496 5d (^{7}F) ^{6}D$_{2.5}$	5120.362	2.900E+05	−2.934
28200 4f^7 ^{6}P$_{3.5}$−47715 5d (^{7}F) ^{6}F$_{4.5}$	5122.920	2.417E+06	−2.023
32180 4f^7 ^{6}I$_{5.5}$−51650 5d (^{7}F) ^{6}G$_{5.5}$	5134.539	1.414E+04	−4.252
32314 4f^7 ^{6}I$_{6.5}$−51650 5d (^{7}F) ^{6}G$_{5.5}$	5170.279	3.087E+04	−3.907
31954 4f^7 ^{6}I$_{4.5}$−51173* 5d (^{7}F) ^{6}G$_{4.5}$	5201.8	1.094E+04	−4.352
32180 4f^7 ^{6}I$_{5.5}$−51173* 5d (^{7}F) ^{6}G$_{4.5}$	5263.5	3.198E+04	−3.877
28629 4f^7 ^{6}P$_{2.5}$−47591* 5d (^{7}F) ^{6}F$_{1.5}$	5272.1	3.348E+05	−2.856
28972* 4f^7 ^{6}P$_{1.5}$−47588* 5d (^{7}F) ^{6}D$_{1.5}$	5370.2	5.562E+05	−2.619
28200 4f^7 ^{6}P$_{3.5}$−46793 5d (^{7}F) ^{6}F$_{3.5}$	5376.780	1.131E+06	−2.313
31954 4f^7 ^{6}I$_{4.5}$−50426 5d (^{7}F) ^{6}G$_{3.5}$	5412.059	2.173E+04	−4.025
28629 4f^7 ^{6}P$_{2.5}$−46793 5d (^{7}F) ^{6}F$_{3.5}$	5503.612	1.527E+06	−2.165
31746 4f^7 ^{6}I$_{3.5}$−49906 5d (^{7}F) ^{6}G$_{2.5}$	5505.185	1.205E+04	−4.262
28972* 4f^7 ^{6}P$_{1.5}$−47013* 5d (^{7}F) ^{6}F$_{0.5}$	5541.4	2.807E+05	−2.888

Table 3. (Contd.)

Transition	λ, Å	g_u, A	log[$g_l f$]
28200 4f^7 ^{6}P$_{3.5}$ − 46109 5d (^{7}F) ^{6}F$_{2.5}$	5582.318	3.539E+05	−2.786
32180 4f^7 ^{6}I$_{5.5}$ − 49957 5d (^{7}F) ^{6}D$_{4.5}$	5623.628	1.995E+04	−4.009
28629 4f^7 ^{6}P$_{2.5}$ − 46109 5d (^{7}F) ^{6}F$_{2.5}$	5719.155	1.485E+06	−2.145
31954 4f^7 ^{6}I$_{4.5}$ − 49293 5d (^{7}F) ^{6}D$_{3.5}$	5765.962	1.829E+04	−4.026
28629 4f^7 ^{6}P$_{2.5}$ − 45851* 5d (^{7}F) ^{6}D$_{1.5}$	5804.8	6.300E+05	−2.498
28972* 4f^7 ^{6}P$_{1.5}$ − 46109 5d (^{7}F) ^{6}F$_{2.5}$	5833.8	5.466E+05	−2.561
28972* 4f^7 ^{6}P$_{1.5}$ − 46096 6s (^{7}F) ^{8}F$_{0.5}$	5838.0	2.222E+04	−3.945
28972* 4f^7 ^{6}P$_{1.5}$ − 45845* 5d (^{7}F) ^{6}D$_{1.5}$	5925.0	1.117E+06	−2.230
28972* 4f^7 ^{6}P$_{1.5}$ − 45844* 5d (^{7}F) ^{6}D$_{0.5}$	5925.3	1.066E+06	−2.251
32314 4f^7 ^{6}I$_{6.5}$ − 49086 5d (^{7}F) ^{6}F$_{5.5}$	5960.671	1.720E+04	−4.053
32180 4f^7 ^{6}I$_{5.5}$ − 47715 5d (^{7}F) ^{6}F$_{4.5}$	6435.220	2.190E+04	−3.870
32073 4f^7 ^{6}I$_{8.5}$ − 47070 5d (^{7}F) ^{6}H$_{7.5}$	6666.347 S	1.504E+07	−0.984
31954 4f^7 ^{6}I$_{4.5}$ − 46793 5d (^{7}F) ^{6}F$_{3.5}$	6737.061	1.651E+04	−3.955
32308 4f^7 ^{6}I$_{7.5}$ − 47070 5d (^{7}F) ^{6}H$_{7.5}$	6772.247 S	6.251E+05	−2.354
32314 4f^7 ^{6}I$_{6.5}$ − 47070 5d (^{7}F) ^{6}H$_{7.5}$	6775.158	1.633E+04	−3.938
28200 4f^7 ^{6}P$_{3.5}$ − 42531 5d (^{7}F) ^{6}P$_{3.5}$	6976.018 S	2.352E+06	−1.780
32180 4f^7 ^{6}I$_{5.5}$ − 46151 5d (^{7}F) ^{6}H$_{6.5}$	7155.559	2.861E+04	−3.644
28629 4f^7 ^{6}P$_{2.5}$ − 42531 5d (^{7}F) ^{6}P$_{3.5}$	7191.036	1.166E+06	−2.062
28200 4f^7 ^{6}P$_{3.5}$ − 42084 5d (^{7}F) ^{8}P$_{4.5}$	7200.451	1.059E+05	−3.098
32308 4f^7 ^{6}I$_{7.5}$ − 46151 5d (^{7}F) ^{6}H$_{6.5}$	7221.838 S	1.070E+07	−1.062
32314 4f^7 ^{6}I$_{6.5}$ − 46151 5d (^{7}F) ^{6}H$_{6.5}$	7225.151 S	8.903E+05	−2.143
31954 4f^7 ^{6}I$_{4.5}$ − 45314 5d (^{7}F) ^{6}H$_{5.5}$	7483.226	3.014E+04	−3.582
32180 4f^7 ^{6}I$_{5.5}$ − 45314 5d (^{7}F) ^{6}H$_{5.5}$	7611.623 S	8.901E+05	−2.097
32314 4f^7 ^{6}I$_{6.5}$ − 45314 5d (^{7}F) ^{6}H$_{5.5}$	7690.435 S	7.697E+06	−1.152
31746 4f^7 ^{6}I$_{3.5}$ − 44554 5d (^{7}F) ^{6}H$_{4.5}$	7805.590	1.824E+04	−3.767
28200 4f^7 ^{6}P$_{3.5}$ − 40898 5d (^{7}F) ^{8}P$_{2.5}$	7873.330 S	8.650E+05	−2.115
28200 4f^7 ^{6}P$_{3.5}$ − 40871 5d (^{7}F) ^{8}P$_{3.5}$	7890.152	6.184E+05	−2.252
31954 4f^7 ^{6}I$_{4.5}$ − 44554 5d (^{7}F) ^{6}H$_{4.5}$	7934.561 S	7.161E+05	−2.156
32180 4f^7 ^{6}I$_{5.5}$ − 44554 5d (^{7}F) ^{6}H$_{4.5}$	8079.071 S	5.620E+06	−1.247
28629 4f^7 ^{6}P$_{2.5}$ − 40898 5d (^{7}F) ^{8}P$_{2.5}$	8148.304	2.862E+04	−3.569
28629 4f^7 ^{6}P$_{2.5}$ − 40871 5d (^{7}F) ^{8}P$_{3.5}$	8166.314	1.458E+05	−2.853
28200 4f^7 ^{6}P$_{3.5}$ − 40372 5d (^{7}F) ^{8}F$_{3.5}$	8213.595	1.537E+04	−3.807
31746 4f^7 ^{6}I$_{3.5}$ − 43885 5d (^{7}F) ^{6}H$_{3.5}$	8235.458	4.246E+05	−2.357
31954 4f^7 ^{6}I$_{4.5}$ − 43885 5d (^{7}F) ^{6}H$_{3.5}$	8379.212 S	4.211E+06	−1.342
28972* 4f^7 ^{6}P$_{1.5}$ − 40898 5d (^{7}F) ^{8}P$_{2.5}$	8383.0	4.150E+05	−2.382
31746 4f^7 ^{6}I$_{3.5}$ − 43396 5d (^{7}F) ^{6}H$_{2.5}$	8581.510 S	3.272E+06	−1.432
32073 4f^7 ^{6}I$_{8.5}$ − 43659 5d (^{7}F) ^{8}G$_{7.5}$	8628.990	1.192E+06	−1.883
28200 4f^7 ^{6}P$_{3.5}$ − 39769 5d (^{7}F) ^{8}P$_{2.5}$	8641.423	8.924E+05	−2.018

Note: S is the wavelength from Sugar and Spector (1974).

* Computed levels.

3. NON-LTE CALCULATIONS FOR THE Eu II λ6645 Å AND Eu III λ6666 Å LINES

3.1. Model Atom

In our calculations, we used the Eu II model atom that was first developed by one of us (Mashonkina 2000); it was used to analyze Eu II lines in cool stars (Mashonkina and Gehren 2000). The model atom includes all the Eu II levels known from laboratory measurements (Martin *et al.* 1978). Data are available for the levels with excitation energies E_i less than 8.3 eV. The high-excitation levels close to the continuum, for which no data are available, have virtually no effect on the population of the Eu II ground state and low-excitation levels in the atmospheres of cool stars, where Eu II is a dominant ionization stage and where the departures from LTE are attributable to radiative transitions between lower terms (Mashonkina 2000; Mashonkina and Gehren 2000). However, when passing to hotter A-type stars, the kinetic equilibrium of Eu II begins to increasingly depend on the processes that couple Eu II and Eu III levels and the high-excitation levels increase in importance. In this study, we attempted to take into account these levels in the model atom and to include the excited Eu III levels in the model atom that are required to compute the Eu III λ6666-Å line under study.

Below, we briefly describe changes in the model atom. All the known Eu II levels belong to the $4f^7$ nl and $4f^6$ 5d nl electronic configurations. The lower level of the $4f^7$ atomic core is $^8S_{3.5}$, with the next level $^6P_{3.5}$ lying higher at a distance of ≈ 3.5 eV. Consequently, the known levels of the configurations with a single excited electron have a quasi-two-particle structure: $4f^7(^8S_{3.5})$nl, where nl = (6–8)s, 6p, 5d, 6d, 4f; their structure resembles that of the Ba II terms. We noticed that the ionization-energy ratios $\chi(6s) : \chi(7s) : \chi(8s)$ and $\chi(5d) : \chi(6d)$ for Eu II were close to those for Ba II, but the level energies for Ba II are known up to $n = 12$ (Roigand and Tondello 1975). We extended the patterns in the behavior of ionization energies for the series of Ba II ns, np, nd, and nf levels to the corresponding series of Eu II levels and computed the energies of the Eu II ns, np, nd levels up to $n = 10$ and of the nf levels up to $n = 8$. Clearly, the derived energies of the high-excitation levels do not claim to be very accurate. We incorporate these levels in the model atom only for a more accurate allowance for all the collisional and radiative processes that couple Eu II and Eu III. The ionization thresholds of all the computed levels are in the visible or infrared spectral ranges between $\lambda =$ 4000 and 15000 Å, and the rates of b–f transitions depend very weakly on the exact threshold wavelength. The oscillator strengths f_{ij} for transitions from the levels with laboratory energies to the computed levels and for transitions between the computed levels were taken by analogy with Ba II. Below, we discuss the effects of uncertainty in f_{ij} for these transitions on the results of non-LTE calculations.

Since one of the lines studied is Eu III λ6666 Å formed during the $4f^7\ ^6I^0_{8.5}$–$4f^6 5d\,^6H_{7.5}$ transition, apart from the ground state, the model atom includes excited Eu III levels from the list of Sugar and Spector (1974). These are the metastable $4f^7\,^6P^0$ and $4f^7\,^6I^0$ levels and all the known terms of the $4f^6$ 5d configuration. The levels of the $4f^6$ 6s and $4f^6$ 6p configurations cannot play a major role in the mechanism of departures from the equilibrium Eu III level population due to the weak radiative coupling with the ground state, because the $4f^7$–$4f^6$ 6s, 6p, $4f^6$ 5d–$4f^6$ 6s transitions are forbidden. Therefore, the $4f^6$ 6s and $4f^6$ 6p terms were not included in the model atom, but they are taken into account in the conservation equation for the number of particles. Finally, the model atom incorporates the Eu IV ground state. The Eu II + Eu III model atom used here is shown in Fig. 1 (the Eu IV ground level is not shown in the figure, because its energies significantly differ from the energies of the remaining levels; the ionization energy of the Eu III ground state is 24.9 eV).

For Eu III lines, we used the oscillator strengths from Section 1. As in our previous non-LTE studies of Eu II (Mashonkina 2000; Mashonkina and Gehren 2000), we computed the photoionization cross sections for the np levels by the quantum-defect method; for the remaining levels, they are hydrogen-like. For permitted transitions, the collision excitation rates can be calculated using the formula of Van Regemorter (1962). For forbidden transitions, the line strength Ω_{ij} is assumed to be equal to unity, except for the Eu II 6s–5d transitions. Having analyzed Eu II lines in the solar spectrum, Mashonkina and Gehren (2000) showed that the collisional coupling of the metastable 5d levels with the 6s ground state must be stronger than that for $\Omega_{ij} = 1$. Therefore, the collision rates for these transitions can be calculated using the formula of Van Regemorter (1962) with f_{ij} that are 1/10 of f_{ij} for the corresponding 6s–6p transitions. The collision ionization rates can be calculated using the formula of Drawin (1961).

3.2. Mechanisms of Departures from LTE

We performed our non-LTE calculations by using the NONLTE3 code (Sakhibullin 1983), which is based on the complete linearization method in the version of Auer and Heasley (1976).

Eu II is a dominant ionization stage in the atmospheres of cooler stars from the sample under

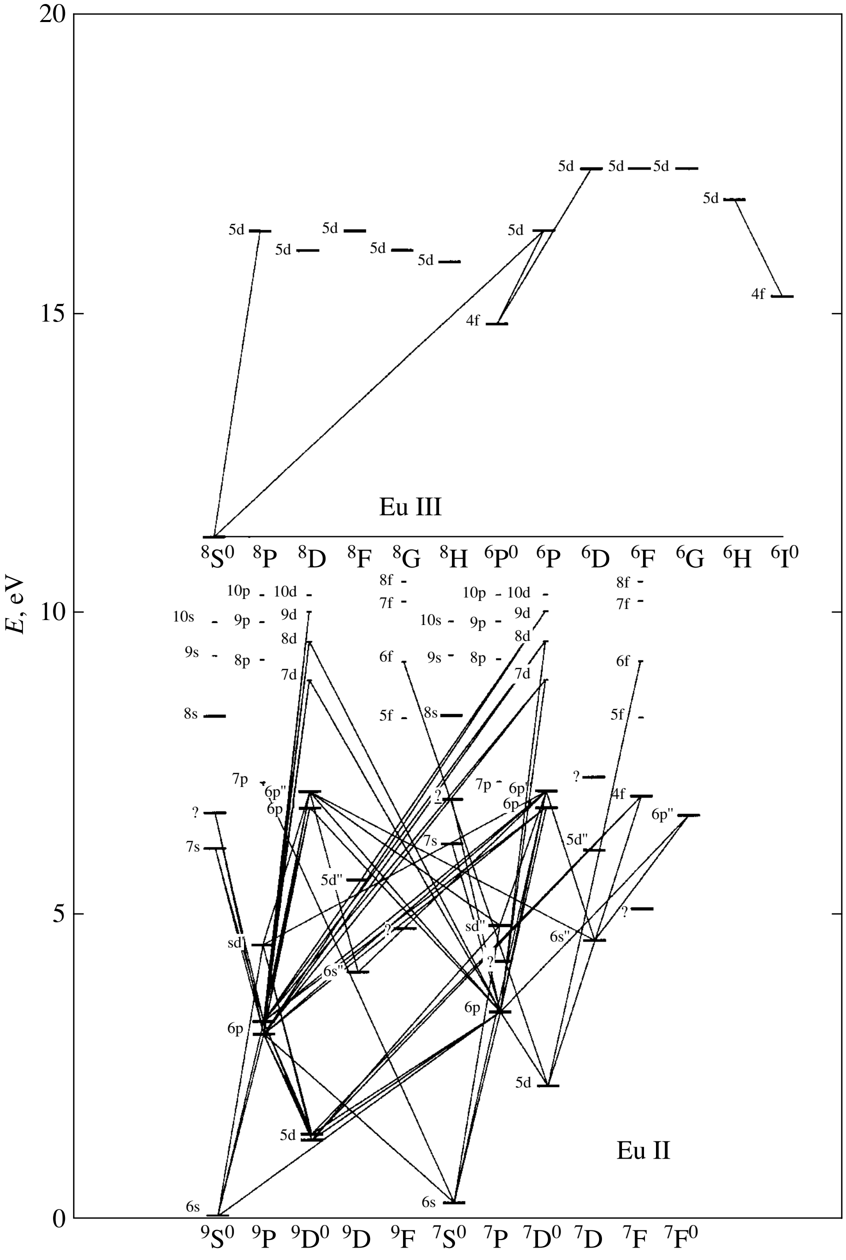

Fig. 1. Eu II+Eu III model atom. The Eu IV ground state is not shown. The solid lines represent linearizable transitions. The computed Eu II levels are indicated by bars.

study ($T_{\rm eff} < 8000$ K), so n(Eu II)/n(Eu III) > 10. However, at higher temperatures, the roles of Eu II and Eu III are interchanged, and Eu III becomes a dominant ionization stage. As a result, the mechanisms of departures from LTE for Eu II and Eu III are different for cool and hot stars. Consider this difference by using two stars as an example: β CrB ($T_{\rm eff} = 7750$ K, $\log g = 4.3$, [Fe/H] $= 0.5$) and α^2 CVn ($T_{\rm eff} = 11500$ K, $\log g = 4.0$, [Fe/H] $= 1$). Figure 2 shows b-factors for the lower Eu II and Eu III levels in the atmospheres of these stars. Here, $b_i = n_i/n_i^*$, where n_i and n_i^* are the populations of level i computed by using the non-LTE approach and the Boltzmann–Saha formulas.

Since Eu II is a dominant ionization stage at $T_{\rm eff} = 7750$ K, the departures from LTE in the Eu II level population are produced mainly by radiative transitions between low-excitation states. Radiative pumping in the 6s–6p (λ4129 Å, λ3820 Å) transitions results in a modest depopulation of the ground state, and b(6s) < 1 in the line formation region. Subsequently, radiative pumping in the 6p–8s and

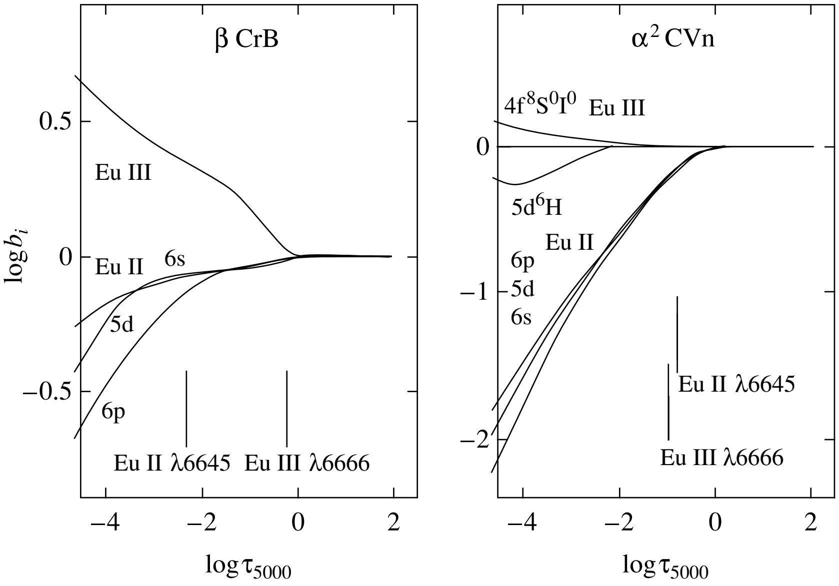

Fig. 2. b factors for the lower Eu II and Eu III levels in the atmospheres of the stars β CrB ($T_{\rm eff} = 7750$ K, $\log g = 4.3$, [Fe/H] = 0.5, [Eu/H] = 3) and α^2 CVn ($T_{\rm eff}$=11500 K, $\log g = 4.0$, [Fe/H] = 1, [Eu/H] = 5). The vertical bars indicate the formation depths for the cores of the lines under study.

6p–6d transitions and photoionization from the 8s and 6d levels take place. We indicate only the main chain of the processes that lead to a continuum overpopulation. The 6p levels are additionally depopulated in spontaneous transitions to the 5d levels and during photoionization in layers that are transparent to radiation at the corresponding frequencies. It follows from the behavior of the b-factors that b(6p) $<$ b(5d) in the formation region of the Eu II λ6645-Å line (5d^{9}D$_6$–6p^{9}P$^0_5$). As a result, the source function in the line S_{ij} becomes smaller than the Planck function $B_\nu(T)$, because $S_{ij} \simeq b_j/b_i B_\nu(T)$ for transitions with $h\nu_{ij} > kT_e$, and the Eu II λ6645-Å line is enhanced compared to the LTE. For the star β CrB, the non-LTE correction to the europium abundance, $\Delta_{\rm NLTE} = \log\varepsilon_{\rm NLTE} - \log\varepsilon_{\rm LTE}$, is negative and equal to -0.17 dex.

Since the Eu II number density accounts for a mere tenth of the Eu III number density in the atmosphere of α^2 CVn, any disbalance in the rates of the b–f transitions strongly affects the Eu II level populations. The dominance of photoionization from the lower Eu II levels (6s, 5d, 6p) over the inverse processes results in a depopulation of the Eu II levels. This is a typical example of overionization, a phenomenon that was discovered in the atmospheres of cool stars for easily ionizable atoms, such as Fe I (Boyarchuk *et al.* 1985), Ca I (Drake 1991), Mg I (Mashonkina *et al.*1996), and others. Since b(5d) < 1 in the line formation region, the λ6645-Å line is weakened compared to LTE and the non-LTE correction to the abundance is positive and equal to $\Delta_{\rm NLTE} = 0.43$. The departures from the LTE in the Eu III level population are attributable to radiative b–b transitions. The Eu III 5d levels are depopulated during spontaneous transitions to 4f in layers that are transparent to radiation at the corresponding frequencies. As a result, $b_j < b_i$ and $S_{ij} < B_\nu(T)$ in the formation region of the Eu III λ6666 Å line. The line is slightly enhanced compared to LTE and $\Delta_{\rm NLTE} = -0.10$.

Although we made some assumptions when developing our model atom and when choosing the atomic data, we performed test calculations to check the effect of these assumptions on the results of our non-LTE calculations.

Since there is Eu II overionization in the atmospheres of stars with $T_{\rm eff} > 8000$ K, it is of crucial importance to include the computed high-excitation Eu II levels in the model atom. They provide close coupling with the continuum (Eu III) and reduce the depopulation of the low-lying Eu II levels caused by photoionization through photorecombination and subsequent cascade transitions. Our calculations for α^2 CVn with a model atom that did not include the computed high-excitation levels yielded an increase in $\Delta_{\rm NLTE}$ (Eu II λ6645 Å) to 0.6 dex. For the cooler star β CrB, $\Delta_{\rm NLTE}$ (Eu II λ6645 Å) varies only slightly.

Changing f_{ij} for Eu III transitions by a factor of 5 causes an insignificant transformation (0.01 dex) of the non-LTE correction to the europium abundance derived from the Eu III λ6666-Å line.

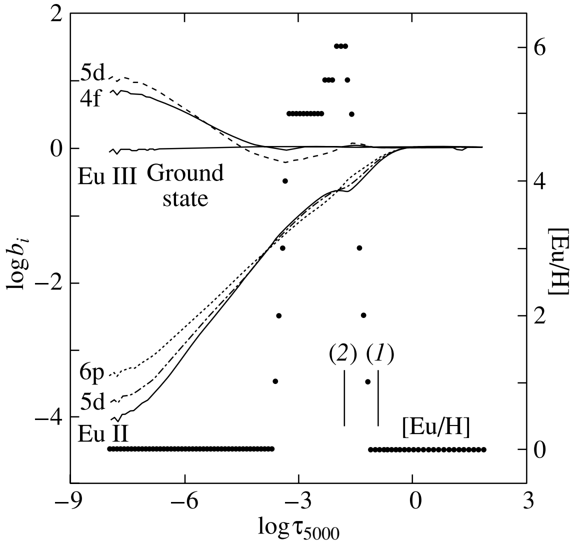

Fig. 3. b-factors for the lower Eu II and Eu III levels in the atmosphere of α^2 CVn in the presence of a layer. The Eu distribution in the stellar atmosphere is indicated by the dotted line; the corresponding scale is given on the right vertical axis. The vertical bars indicate the formation depths of the Eu II λ6645(*1*) and Eu III λ6666 (*2*) lines.

4. Eu ABUNDANCES IN THE STARS α^2 CVn AND β CrB

Ryabchikova *et al.* (1999) analyzed the Eu abundance in the atmospheres of several Ap stars, including α^2 CVn and β CrB. The authors used the same lines as those considered here. All calculations were performed by including a magnetic field in the line transfer equation. The astrophysical oscillator strength of the Eu III line was determined from the spectra of several cool Ap stars with a very intense Eu II λ6645.11 Å line and an intense Eu III λ6666.35 Å line: $\log(gf) = +1.18$; the standard assumption of LTE ionization balance and a uniform distribution of elements in the atmosphere were used. However, the authors noted that when analyzing the atmospheric europium abundance in the hot Ap star α^2 CVn, using the astrophysical oscillator strength of the Eu III line was incompatible with the condition of ionization balance. They attributed this incompatibility to possible non-LTE effects and/or to Eu stratification in the atmospheres of peculiar stars. The authors also emphasized that theoretical calculations or laboratory measurements of the transition probabilities for Eu III lines are required to test the astrophysical oscillator strengths.

4.1. α^2 CVn

As our calculations show, the intensity of the Eu III 6666.35 Å depends weakly on temperature in the range 11000 K $< T_{\rm eff} <$ 12000 K, and the non-LTE effects for it are marginal over the entire atmospheric depth of α^2 CVn. From this viewpoint, the atmosphere of α^2 CVn is convenient for testing the atomic parameters of Eu III λ6666.35 Å. If we take the oscillator strength of Eu III λ6666.35 Å computed here ($\log(gf) = -0.98$) and the corresponding non-LTE corrections to the abundance derived from Eu II (+0.43) and Eu III (−0.10), then the atmospheric europium abundance in α^2 CVn from Ryabchikova *et al.* (1999) can be corrected. The corresponding results are presented in Table 4.

The last two columns in Table 4 contain the equivalent widths of Eu II λ6645.11 Å and Eu III λ6666.35 Å computed in the non-LTE and LTE approximations for a homogeneous atmosphere with a Eu overabundance ([Eu/H] = +5 dex) and for the case where Eu is concentrated in the $-3.6 < \log \tau_{5000} < -1.2$ layer. The Eu overabundance in the layer reaches +6 dex; in the remaining atmosphere, its abundance is solar. The Eu distribution and the corresponding b-factors for the stratified atmosphere of α^2 CVn are shown in Fig. 3. Since the program of our non-LTE calculations does not include a magnetic field, its effect is taken into account by introducing a pseudomicroturbulence, which we estimated to be 4 km s^{-1}.

It should be noted that for a peculiar star with a temperature close to that of α^2 CVn, the non-LTE effects for Eu II lines are enhanced in a stratified atmosphere, whereas the non-LTE correction for Eu III lines is the same as that for a homogeneous atmosphere.

The data from Table 4 suggest that for α^2 CVn, we obtained matched abundances from Eu II and Eu III lines both in a homogeneous atmosphere and in the presence of a Eu layer, within the accuracy determined by the total errors in the line atomic parameters and the model atmosphere.

The computed oscillator strengths of Eu III lines were also tested by analyzing ultraviolet spectra of α^2 CVn. The star was observed as part of G. Wahlgren's program with the Goddard High Resolution Spectrograph (GHRS) aboard the Hubble Space Telescope. The 2300–2640-Å spectra were retrieved from the European Southern Observatory Archive (spectral resolution of the order of 30000) and reduced to the continuum at 2495 Å, which gives the highest peak in the entire observed spectral range (Wahlgren 1998). Synthetic spectra near the Eu III λ2375.461, 2444.382, and 2445.992-Å lines were computed using the SYNTHMAG code (Piskunov 1999) with a magnetic field for the phase of the magnetic and lanthanide

Table 4. Equivalent widths of the Eu II λ6645.11-Å and Eu III λ6666.35-Å lines in the spectrum of α^2 CVn and the europium abundance. The values in the third column were taken from Ryabchikova *et al.* (1999) for phase 0.976 (Eu peak) and corrected for non-LTE effects and for the difference between the astrophysical and computed oscillator strengths for the Eu III line

Line	W_λ, mÅ (observations)	log(Eu/H) homogeneous atmosphere, non-LTE	$W_{\rm NLTE}/W_{\rm LTE}$	
			log(Eu/H) = −6.50	layer
Eu II λ6645.11 Å	50	−6.47	51/92	56/122
Eu III λ6666.35 Å	61	−6.32	64/56	77/67

Table 5. The equivalent widths of the Eu II λ6645.11-Å and Eu III λ6666.35-Å lines observed in the spectrum of β CrB and computed in the non-LTE and LTE approximations

Line, Å	W_λ, mÅ (observations)	Homogeneous atmosphere,	$W_{\rm NLTE}/W_{\rm LTE}$ Layer		
		[Eu/H] = 3	[Eu/H] = 4	[Eu/H] = 5	[Eu/H] = 6
Eu II λ6645.11	225	237/225	10.7/104.3	52/252	114/325
Eu III λ6666.35	66	1.2/0.7	–	2.7/0.07	8.7/0.3

peaks at the following abundances of the major chemical elements that contribute to the spectral range under study: $\log({\rm Si}/N_{\rm tot}) = -4.2$, $\log({\rm Cr}/N_{\rm tot}) = -5.8$, $\log({\rm Fe}/N_{\rm tot}) = -4.1$, $\log({\rm Eu}/N_{\rm tot}) = -6.5$, $\log({\rm Pr}/N_{\rm tot}) = -7.2$, $\log({\rm Er}/N_{\rm tot}) = -6.2$, where $N_{\rm tot}$ is the total number of atoms of all elements. Below, we also use $\log(N/H)$. For stars with a solar helium abundance, $\log(N/N_{\rm tot}) - \log(N/H) = -0.04$; for peculiar stars with a helium underabundance, this difference can be even smaller. The Si and Cr abundances and the magnetic vector magnitude at the peak phase ($B_{\rm s} = 3850$ G) were taken from Kochukhov *et al.* (2001). We estimated the remaining abundances by analyzing an optical portion of the spectrum; they match the estimates that were obtained by Wahlgren (1998) from an analysis of optical spectra for α^2 CVn. The oscillator strengths were taken from the D.R.E.A.M. database (http://www.umh.ac.be/~astro/dream.shtml) for the Pr III line and from VALD (Kupka *et al.* 1999) for the remaining lines. The rotational velocity of the star was assumed to be 17 km s^{-1} (Khokhlova and Pavlova 1984). The observed spectra are compared with the synthetic spectra computed in the LTE approximation in Figs. 4 and 5. Only the strongest lines that fall within the spectral range under consideration are shown, although a total of 79 spectral lines were chosen to compute synthetic spectra for each of the portions. The solid line represents the synthetic spectrum computed with $\log({\rm Eu}/N_{\rm tot}) = -6.5$ and with the oscillator strengths of Eu III lines from this paper; the dashed line indicates the synthetic spectrum without Eu III lines. It can be immediately concluded that, despite the large atmospheric Eu overabundance in α^2 CVn, the Eu III lines do not dominate. Lines of the iron-peak elements, mostly Fe II, mainly contribute to the absorption in the spectral ranges under consideration. Nevertheless, comparison with observations shows that, within the above accuracy, the oscillator strengths of ultraviolet lines provide a Eu abundance close to our value obtained by analyzing visible Eu II and Eu III lines. The non-LTE equivalent widths of ultraviolet Eu III lines (≈150 mÅ) exceed their LTE values by a mere 5%.

4.2. β CrB

β CrB belongs to the group of cool magnetic peculiar stars with intense Eu II lines and an unexpectedly strong (for these effective temperatures) Eu III λ6666.35-Å line. An LTE analysis of Eu II and Eu III lines in the spectra of these stars yielded an astrophysical oscillator strength of the Eu III λ6666.35-Å line, $\log(gf) = +1.18.$, which exceeds its theoretical value from Table 3 by two orders of magnitude. Since the non-LTE corrections for a homogeneous atmosphere of β CrB are small both for Eu II λ6645.11 Å and for Eu III λ6666.35 Å (see subsection "Mechanisms of Departures from LTE"), the observed intensities of these lines in the spectra of cool Ap stars cannot be explained in terms of the model with a homogeneous chemical composition if we use the theoretical oscillator strengths of Eu III lines whose correctness was confirmed by an analysis of the α^2 CVn spectrum. Since the departures from LTE in the atmosphere of β CrB during the formation of Eu II and Eu III lines are opposite in sign and increase in the upper atmosphere, it would be natural to assume that we deal with the Eu number density in the upper stellar atmosphere.

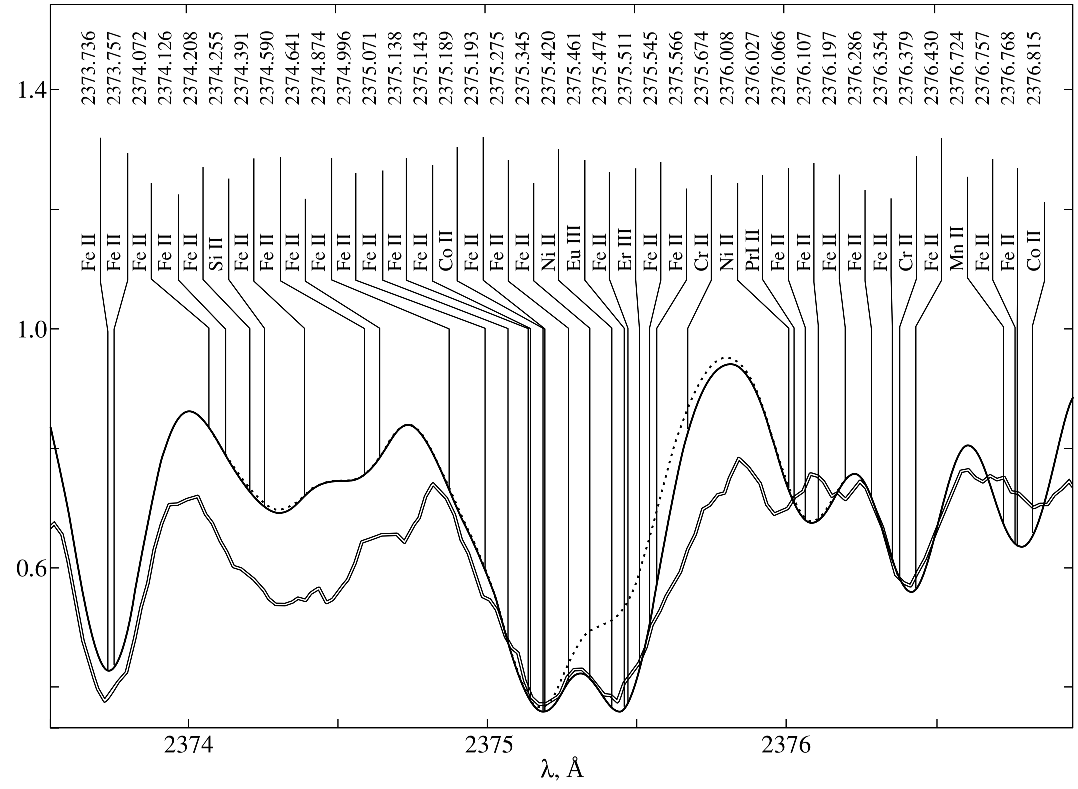

Fig. 4. Comparison of the observed (double line) and synthetic spectra for α^2 CVn near the resonance Eu III λ2375.461 line. The dashed line represents the synthetic spectrum computed without the Eu III line.

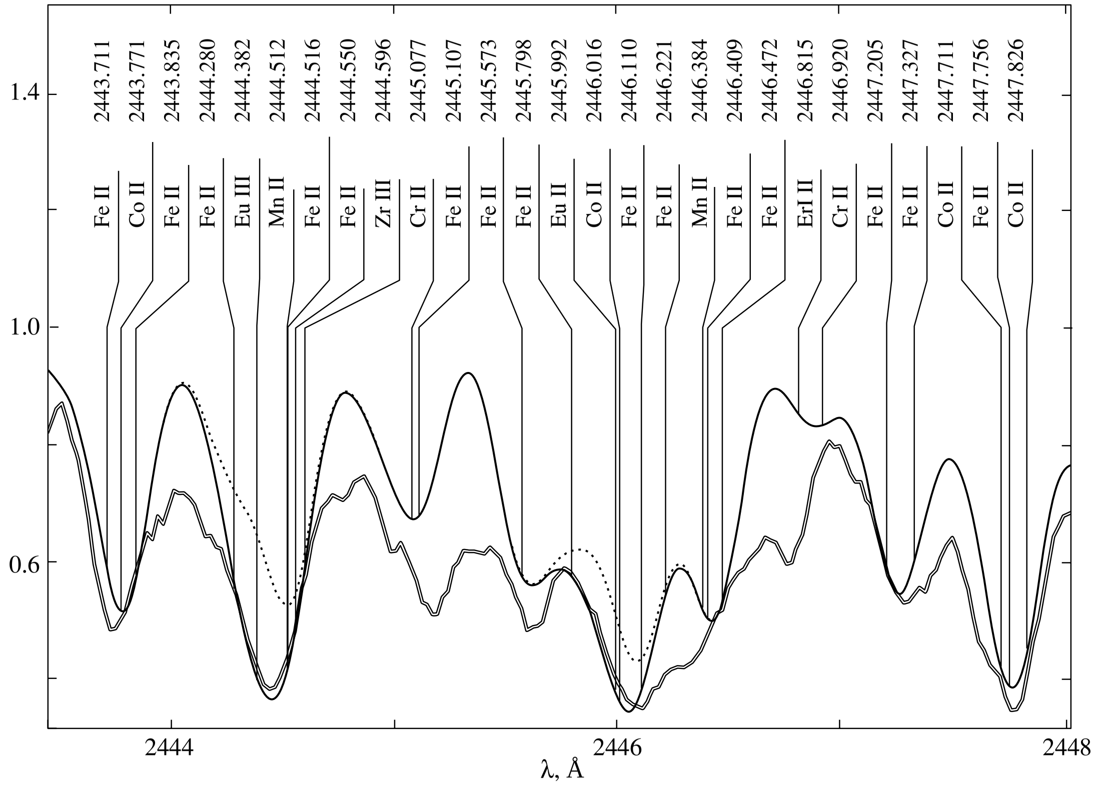

Fig. 5. Same as Fig. 4 for the Eu III $\lambda\lambda$2444.382 and 2445.992 lines.

We performed non-LTE calculations for a nonuniform europium distribution in depth, in which we ran into purely computational difficulties. In the relatively cool atmosphere of β CrB, the number density of Eu IV in the line formation region is almost ten orders of magnitude lower than that of Eu II and Eu III; as a result, very small terms related to Eu IV recombinations appear in the equations of kinetic equilibrium. The matrix of coefficients for the equations of kinetic equilibrium is ill-conditioned, and about 20 iterations are required to obtain the solution of the non-LTE problem even for a homogeneous atmosphere. For comparison, note that the solution for the hotter star α^2 CVn is obtained after six iterations. Abandoning LTE implies that the population of a particular level at some depth depends not only on all the processes that take place in the atom at this depth but also on all transitions at all other depths. When we introduce a layer with a europium abundance that is five to six orders of magnitude higher than that in the remaining atmosphere, the difference between the terms in the equations of kinetic equilibrium increases still further and the convergence of the solution proves to be very sensitive to the location of the layer in depth, its size, and the peak overabundance in the layer.

As a result, we were able to obtain the solution only for one layer with the peak concentration $[\mathrm{Eu/H}] = +4, +5, +6$ located at optical depths $-7.3 < \log(\tau_{5000}) < -4.3$. When displacing the layer upward or downward and when further increasing the concentration in the layer, the non-LTE solution diverges. The non-LTE corrections are found to be very large. Table 5 gives the observed equivalent widths of the lines under study in the spectrum of β CrB and the line equivalent widths computed in the non-LTE and LTE approximations for a homogeneous atmosphere with the europium abundance derived from Eu II lines [$\log(\mathrm{Eu/H}) = -8.50$, $[\mathrm{Eu/H}] = +3$ (Ryabchikova *et al.* 1999)] and for a layer with the above three concentrations.

Although in none of our solutions for an inhomogeneous atmosphere did we obtain equivalent widths close to their observed values, the results presented in Table 5 suggest that non-LTE calculations can be reconciled with observations by varying the layer location and thickness and the Eu concentration in the layer.

5. CONCLUSIONS

We have computed the theoretical oscillator strengths of Eu III lines to interpret the observed spectra of magnetic peculiar stars. For the hot Ap star α^2 CVn, we showed that when taking into account the departures from LTE and when using the theoretical oscillator strengths, we obtained the same europium abundances from Eu II and Eu III lines. Thus, we conclude that the scale of oscillator strengths for Eu III lines computed here faithfully describes the observed lines over a wide spectral range of the hot peculiar star α^2 CVn. We also conclude that the overestimated astrophysical oscillator strengths result from the violation of ionization balance in the spectra of cool peculiar star, whose typical representative is β CrB.

The newly obtained atomic data can be used to compute the diffusion of Eu atoms and ions in the atmospheres of magnetic stars. Diffusion calculations are needed to test the hypothesis of the Eu concentration in the upper atmospheres of cool magnetic stars, which can account for the observed intensities of optical Eu II and Eu III lines in these stars.

ACKNOWLEDGMENTS

We are grateful to the HST Scientific Data Archive and the ESO/ST-ECF Archive for the opportunity to use ultraviolet spectra of α^2 CVn. Our non-LTE calculations were performed on a computer at the Kazan Astronomogeodesic Society. We wish to thank the Russian Foundation for Basic Research (project no. 99-02-17488a), the State Science and Technology Program "Astronomy" (project no. 2.2.1.5), and the Austrian Fonds zur Förderung der wissenschaftlichen Forschung (S7303-AST)" for partial support of this study.

REFERENCES

1. L. H. Auer and J. Heasley, Astrophys. J. **205**, 165 (1976).
2. A. A. Boyarchuk, L. S. Lyubimkov, and N. A. Sakhibullin, Astrofizika **22**, 339 (1985).
3. R. D. Cowan, *The Theory of Atomic Structure and Spectra* (Univ. of California Press, Berkeley, 1981).
4. H.-W. Drawin, Z. Phys. **164**, 513 (1961).
5. J. J. Drake, Mon. Not. R. Astron. Soc. **251**, 369 (1991).
6. V. L. Khokhlova and V. M. Pavlova, Pis'ma Astron. Zh. **10**, 377 (1984) [Sov. Astron. Lett. **10**, 158 (1984)].
7. O. Kochukhov, N. Piskunov, I. Ilyin, S. Ilyina, and I. Tuominen, in *Magnetic Fields Across the Hertzprung-Russel Diagram,* Ed. by G. Mathys, S. K. Solanki, and T. Wickramasinghe (Santiago, Chile, 2001) (in press).
8. F. Kupka, N. Piskunov, T. A. Ryabchikova, *et al.*, Astron. Astrophys., Suppl. Ser. **138**, 119 (1999).
9. W. C. Martin, R. Zalubas, and L. Hagan, *Atomic Energy Levels—The Rare-Earth Elements* (National Bureau of Standards, Washington, 1978), NSRDS-NBS 60.
10. L. I. Mashonkina, Astron. Zh. **77**, 630 (2000) [Astron. Rep. **44**, 558 (2000)].

11. L. I. Mashonkina and T. Gehren, Astron. Astrophys. **364**, 249 (2000).
12. L. I. Mashonkina, N. A. Sakhibullin, and N. N. Shimanskaya, Astron. Zh. **73**, 212 (1996) [Astron. Rep. **40**, 187 (1996)].
13. G. Michaud, Astrophys. J. **160**, 641 (1970).
14. P. Palmeri, P. Quinet, Y. Frémat, *et al.*, Astrophys. J., Suppl. Ser. **129**, 367 (2000).
15. N. E. Piskunov, in *Proceedings of the 2nd Workshop on Solar Polarization,* Ed. by J. Stenflo and K. N. Nagendra (Kluwer, Dordrecht, 1999), p. 515.
16. P. Quinet, P. Palmeri, and E. Biémont, J. Quant. Spectrosc. Radiat. Transf. **62**, 625 (1999).
17. R. A. Roigand and G. Tondello, J. Opt. Soc. Am. **65**, 829 (1975).
18. H. van Regemorter, Astrophys. J. **136**, 906 (1962).
19. T. Ryabchikova, N. Piskunov, I. Savanov, *et al.*, Astron. Astrophys. **343**, 229 (1999).
20. N. A. Sakhibullin, Tr. Kazan. Gor. Astron. Obs. **48**, 9 (1983).
21. J. Sugar and N. Spector, J. Opt. Soc. Am. **64**, 1484 (1974).
22. G. M. Wahlgren, Contrib. Astron. Obs. Skalnate Pleso **27**, 368 (1998).
23. J.-F. Wyart, J. Opt. Soc. Am. **68**, 197 (1978).
24. J.-F. Wyart and C. Bauche-Arnould, Phys. Scr. **22**, 583 (1980).
25. Z. Zhang, Z. S. Li, H. Lundberg, *et al.*, J. Phys. B **33**, 521 (2000).

Translated by V. Astakhov

Astronomy Letters, Vol. 28, No. 1, 2002, pp. 49–62. Translated from Pis'ma v Astronomicheskiĭ Zhurnal, Vol. 28, No. 1, 2002, pp. 56–70.
Original Russian Text Copyright © 2002 by Klochkova, Panchuk, Tavolzhanskaya.

HD 331319: A Post-AGB F Supergiant with He I Lines

V. G. Klochkova[*], **V. E. Panchuk**, and **N. S. Tavolzhanskaya**

Special Astrophysical Observatory, Russian Academy of Sciences,
Nizhnii Arkhyz, Stavropolskiĭ krai, 357147 Russia

Received April 26, 2001; in final form, August 8, 2001

Abstract—Based on CCD spectra taken with an echelle spectrometer attached to the 6-m telescope, we have determined for the first time the fundamental parameters and detailed chemical composition of HD 331319, an optical counterpart of the infrared source IRAS 19475+3119, by the model-atmosphere method. Helium lines were detected in the spectrum of this luminous ($Mv < -8^m$) object with the effective temperature $T_{\rm eff} = 7200$ K. This detection can be interpreted as a significant helium overabundance in the observed atmospheric layers and may be considered as a manifestation of helium synthesis during the preceding evolution. Nitrogen and oxygen were found to be overabundant, $[{\rm N/Fe}]_\odot = +1.30$ dex and $[{\rm O/Fe}]_\odot = +0.64$ dex, with the carbon overabundance being modest. The metallicity of the stellar atmosphere, $[{\rm Fe/H}]_\odot = -0.25$, differs only slightly from its solar value. The s-process metals are not overabundant but most likely underabundant relative to iron: $[X/{\rm Fe}]_\odot = -0.68$ for Y and Zr. Barium is also underabundant relative to iron: $[{\rm Ba/Fe}]_\odot = -0.47$. The heavier elements La, Ce, Nd, and Eu are slightly enhanced relative to iron: the mean $[X/{\rm Fe}]_\odot = +0.16$ for them. In general, the elemental abundances confirm that IRAS 19475+3119 is a post-AGB object. The metallicity in combination with the radial velocity $V_r = -3.4$ km s^{-1} and Galactic latitude $|b| = 2\overset{\circ}{.}7$ of the object suggest that it belongs to the Galactic disk population. The envelope expansion velocity, $V_{\rm exp} \approx 21$ km s^{-1}, was determined from the positions of the absorption bands that originate in the circumstellar envelope. A comparison of our results for the comparison star HD 161796 = IRAS 17436+5003, a typical post-AGB object, with previously published data revealed an evolutionary increase in the effective temperature of HD 161796 at a mean rate of ≥50° per year. © *2002 MAIK "Nauka/Interperiodica".*

Key words: *post-AGB supergiants, abundance determination*

1. INTRODUCTION

Nuclear reactions proceed in the interiors of stars as they evolve, which result, in particular, in the synthesis of helium nuclei. Therefore, it would be natural to use the spectra of evolved stars with various masses to determine the helium abundance. Determining the helium abundance for stars at various evolutionary stages has been the subject of many studies. However, as yet, there is insufficient information on the helium enrichment of the atmospheric surface layers in post-AGB stars. Since these stars have already traversed a long evolutionary path (hydrogen and helium core and shell burning, mixing, and dredge-up) and passed through the stage of mass loss in the form of stellar wind on the asymptotic giant branch (AGB), there is every reason to expect a changed helium abundance in their atmospheres. Stars at the evolutionary stage of transition from AGB to a planetary nebula are commonly called post-AGB objects or protoplanetary nebulae (PPN).

We present the results of our spectroscopic analysis for the supergiant HD 331319, an optical counterpart of the IR source IRAS 19475+3119 (below referred to as IRAS 19475) whose spectrum was classified by Bidelman as F3 Ib [see the reference in Likkel *et al.* (1991)]. The energy distribution for HD 331319 has a double-peaked shape typical of post-AGB objects, which is attributable to an excess of the infrared flux emitted by the detached circumstellar envelope. The IRAS survey failed to resolve the nebula around HD 331319 (Young *et al.* 1993).

As a comparison object, we consider the well-known high-latitude superginat HD 161796, whose optical spectrum (F3 Ib) is similar to the spectrum of HD 331319. The supergiant HD 161796 is an optical counterpart of the IR source IRAS 17436+5003 (below referred to as IRAS 17436). Both these objects belong to reliable PPN candidates (Likkel *et al.* 1991). In the IR color–color diagram, IRAS 19475 and IRAS 17436 lie in region V (Loup *et al.* 1993).

Here, we determine the fundamental parameters, effective temperature $T_{\rm eff}$ and surface gravity $\log g$,

---

[*] E-mail: `valenta@sao.ru`

Table 1. A log of observations and the heliocentric radial velocities of IRAS 19475 measured from various features in its optical spectra

Spectrum	JD 2450000+	$V_\odot$, km s^{-1}						
		Metals, n	$H\alpha$			Na D1, D2	DIB (n)	
			blueward emission	abs	redward emission		IS	CS
s13203	0651.409	−2.0(187)	−41.4	+2.8	+57.2	−8.4	−11.2(4)	−24.3(1)
s26813	1651.575	−2.2(177)	−45.2	+1.8	+48.4	−8.6	−10.7(3)	−21.7(5)
s27323	1658.517	−4.6(33)	−41.0	+1.6	+42.0	−8.6	−11.8(6)	−21.3(1)
s27608	1708.451	−4.7(158)	−40.4	+2.3	+55.1	−7.4	−11.9(5)	−26.8(6)
Average, km s^{-1}		−3.4	−42.0	+2.1	+50.7	−8.2	−11.4	−24.2
$V_{\rm lsr}$, km s^{-1}		14.4	−24.2	+19.9	+68.5	+9.6	+6.4	−6.4

Note: The numbers in parentheses are the numbers of measured lines. The last row gives the velocities averaged over four spectra and corrected for solar motion toward the apex.

and compute the chemical composition (Section 2). We also analyze the elemental abundances and the pattern of the radial velocities measured from various spectral features for the PPN candidate whose optical spectrum has not been studied previously (Section 3). Our main conclusions are briefly summarized in Section 4.

2. OBSERVATIONS, REDUCTION, AND ANALYSIS OF SPECTRA

We obtained the spectroscopic data at the prime focus of the 6-m (BTA) telescope using the PFES echelle spectrometer. The spectrometer and its capabilities were briefly described by Panchuk *et al.* (1998). The mean epochs of observations are given in Table 1. An echelle spectrum of the comparison star HD 161796 was taken on August 3, 1993. The signal-to-noise ratio for all the spectra used here significantly exceeds 100, which makes it possible to reliably measure the equivalent widths of weak lines up to 5–7 mÅ. The PFES echelle spectrometer is equipped with the 1160 × 1040-pixel CCD array (16 × 16 μm pixel size) designed at the Special Astrophysical Observatory. The PFES spectrometer provides a spectral resolution of ∼15000 simultaneously in the wavelength range 4550–7930 Å; the range limits can be changed. The reduction of two-dimensional images (the standard procedures of dark-current subtraction, cosmic-ray-particle hit removal, stray-light subtraction, and echelle-order extraction) was performed using the ECHELLE context of the MIDAS system (1998 version). We carried out spectrophotometric and position measurements on one-dimensional spectra with the DECH20 package (Klochkova and Galazutdinov 1991; Galazutdinov 1992).

The radial velocities measured from individual spectrograms of HD 331319 are given in Table 1. First, we singled out unblended lines by comparing the observed and synthetic spectra. The position zero point for each spectrogram was determined by the standard method, by tying in to the positions of ionospheric emissions of the night sky and the absorption telluric spectrum, which are observed against the background of the object's spectrum. When the number of lines exceeded 100, the error of the mean was typically $\delta = 0.3$ km s^{-1}, with the error of a single-line measurement being $\sigma \approx 2.5$ km s^{-1}. The average velocity derived from metal lines $Vr(\text{met}) = -3.4$ km s^{-1}, which may be considered as the systemic velocity, is in good agreement for four epochs of observations. Consequently, the radial velocity of HD 331319 may be assumed to be nonvariable, within the limits of the measurement errors.

We found the main peculiarity, a complex absorption–emission $H\alpha$ profile, even in the first spectrum of HD 331319 (see Fig. 1). The second peculiarity of the HD 331319 spectrum is the presence of absorption features that coincide in position with the He I lines (Fig. 2), which are normally absent in the spectra of such cool supergiants. The spectrum of HD 331319 is also remarkable in that the C I and O I lines belong to the strongest absorption features.

2.1. Determining the Model Parameters and Computing the Chemical Composition

To determine the fundamental parameters of model stellar atmospheres, effective temperature $T_{\rm eff}$ and surface gravity $\log g$, and to compute the chemical composition and synthetic spectra, we used the grid of model stellar atmospheres computed by Kurucz

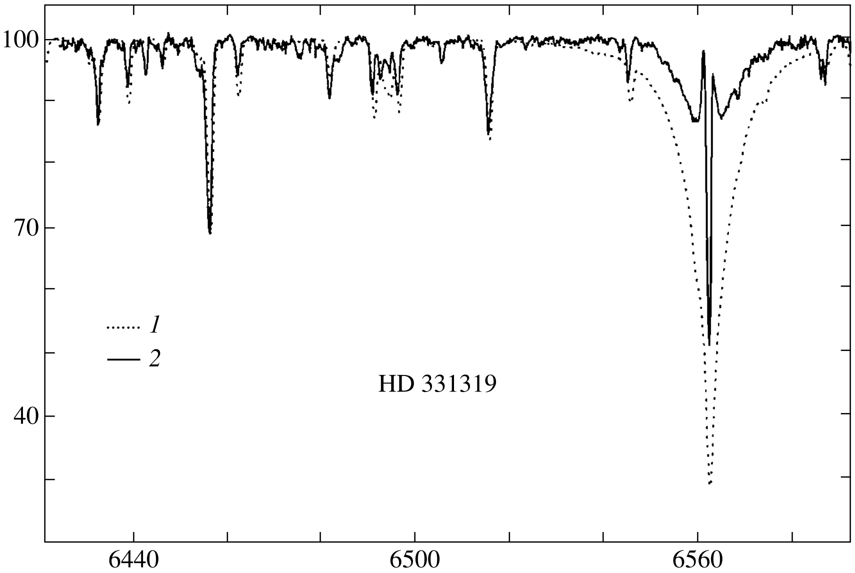

Fig. 1. Comparison of the theoretical (*1*) and observed, s26813, (*2*) spectra for HD 331319 near the $H\alpha$ line. The theoretical spectrum was computed with the parameters and chemical composition from Table 2. The helium abundance is solar.

(1993) in the hydrostatic approximation for various metallicities.

The effective temperature was determined by the standard method from the condition of the Fe I abundance being independent of the excitation potential for the corresponding lines. We chose the surface gravity from the condition of ionization balance for iron atoms and the microturbulence from the condition of the iron abundance being independent of the line intensity.

When determining the model-atmosphere parameters, we used low- and moderate-intensity lines with equivalent widths $W \leq 0.25$ mÅ. The approximation of a steady-state plane-parallel atmosphere may be inaccurate in describing the strongest spectral features. In addition, some of the strong absorption features could be distorted by the influence of the circumstellar envelope; at an insufficient spectral resolution, the intensities of the envelope components are included in the intensities of the atmospheric components.

The oscillator strengths gf of the spectral lines involved in determining the model parameters and elemental abundances were taken from Klochkova and Panchuk (1996) and Klochkova *et al.* (2000).

Thus, we determined the effective temperatures from the condition of the iron abundance being independent of the lower-level excitation potential for the lines used. An additional reliability criterion for the method is the lack of the same dependence for other chemical elements, which are also represented in the spectra by numerous lines (e.g., Si I, Ca I, Sc II, Ti II, Cr II, Ni I). In addition, for a reliable microturbulence determination, there is no dependence of individual abundances on the equivalent widths of the lines used in our calculations. The silicon

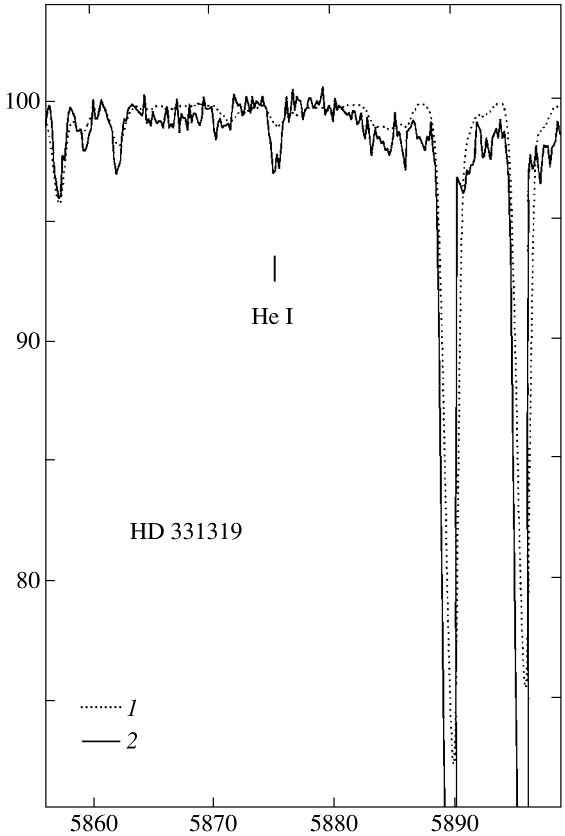

Fig. 2. Same as Fig. 1 for a wavelength range with the He 5876-Å line and the sodium doublet. The difference in the sodium-doublet intensities is attributable to the contribution of interstellar lines to the observed profile.

Table 2. The chemical composition $\log \epsilon(X)$ of HD 331319 for two spectra and of the comparison star HD 161796 at $\log \epsilon(\mathrm{H}) = 12.0$

E	$\epsilon(E)^*$	HD 331319							HD 161796		
		X	s26813 7200K, 0.5, 5.0 km s^{-1},			s27608 7300K, 0.5, 6.0 km s^{-1}			s06401 7100K, 0.5, 6.0 km s^{-1}		
			$\epsilon(X)$	n	σ	$\epsilon(X)$	n	σ	$\epsilon(X)$	n	σ
He	10.99	He I	12.69	6	0.12	12.55	5	0.32	–	–	–
C	8.55	C I	8.39	22	0.24	8.50	20	0.24	8.52	5	0.14
N	7.97	N I	8.99	2	0.20	9.04	3	0.17	8.39	3	0.17
O	8.87	O I	9.41	3	0.12	9.17	3	0.12	9.15	2	–
Na	6.33	Na I	6.37	5	0.16	6.47	4	0.13	6.40	4	0.12
Mg	7.58	Mg I	7.31	3	0.24	7.16	3	0.25	7.26	1	–
Al	6.47	Al I	6.02	3	0.21	5.90	3	0.10	6.20	2	–
Si	7.55	Si I	7.80	22	0.23	7.73	20	0.18	–	–	–
		Si II	7.95	1	–	7.85	1	–	–	–	–
S	7.21	S I	7.38	6	0.20	7.36	5	0.08	7.46	6	0.20
Ca	6.36	Ca I	5.87	15	0.17	6.04	15	0.21	6.02	17	0.16
Sc	3.17	Sc II	2.43	12	0.21	2.44	8	0.18	2.43	6	0.26
Ti	5.02	Ti II	4.37	12	0.26	4.36	13	0.18	–	–	–
V	4.00	V II	3.36	3	0.18	3.42	3	0.14	–	–	–
Cr	5.67	Cr I	5.23	4	0.17	5.33	5	0.19	–	–	–
		Cr II	5.46	16	0.20	5.62	15	0.19	–	–	–
Mn	5.39	Mn I	5.59**	2	0.17	5.43**	4	0.33	–	–	–
Fe	7.50	Fe I	7.25	128	0.25	7.29	131	0.26	7.25	63	0.16
		Fe II	7.25	23	0.20	7.34	19	0.12	7.27	13	0.14
Ni	6.25	Ni I	6.10	13	0.23	6.35	26	0.29	6.28	12	0.37
Cu	4.21	Cu I	4.28	2	0.21	4.20	1	–	4.23	1	–
Zn	4.60	Zn I	4.41	3	0.25	4.41	3	0.35	4.63	1	–
Y	2.24	Y II	1.06	6	0.20	1.43	5	0.34	–	–	–
Zr	2.60	Zr II	1.79	3	0.21	1.80	1	–	–	–	–
Ba	2.13	Ba II	1.40	3	0.14	1.48	3	0.15	1.62	3	0.10
La	1.22	La II	1.22	5	0.25	1.31	4	0.03	–	–	–
Ce	1.55	Ce II	1.45	2	0.11	1.44	2	0.05	–	–	–
Nd	1.50	Nd II	0.91	3	0.08	1.72	4	0.27	1.58	1	–
Eu	0.51	Eu II	0.41	2	0.20	0.70	2	0.11	0.02**	1	–

Note: n is the number of lines used, and σ is the dispersion of the abundance derived for a given number of lines. Model parameters are given under the spectrum number.

* Data for the Sun from Grevesse *et al.* (1996).

** Uncertain values.

abundances determined from lines of neutral atoms and ions are in agreement, within the accuracy of the method, suggesting that the atmospheric surface gravity was correctly estimated from the condition of ionization balance for iron atoms. The internal agreement between the parameters suggests that the homogeneous model atmospheres used are suitable for computing weak lines in the LTE approximation.

The derived model-atmosphere parameters $T_{\rm eff}$, $\log g$, $\xi_{\rm t}$, and elemental abundances $\epsilon(X)$ for each individual spectrum of the stars under study are given in Table 2. The elemental abundances relative to iron $[X/{\rm Fe}]_\odot$ are given in Table 3.

The low surface gravity, $\log g = 0.5$, agrees with the status of an F3 Ib supergiant obtained for HD 331319 from the spectral classification. We estimated the absolute magnitude M_V of the star from the equivalent width of the IR O I$\lambda \approx$ 7773-Å triplet. The equivalent width of this triplet, W(O I), can serve as a good criterion for the absolute luminosity of supergiants over a wide temperature range. In the spectrum of HD 161796, $W({\rm O\,I}) = 2.2$ Å, which yields $M_V = -8^m$ when using the calibration of Slowik and Peterson (1995). In the spectrum of the star HD 331319 under study, the mean for three spectra is $W({\rm O\,I}) = 2.6$ Å, which belongs to the extremely high observed values of W(O I). An even higher absolute magnitude $M_V < -8^m$ corresponds to this value. Unfortunately, since the set of UBV data required to estimate the color excesses is incomplete, we cannot determine the distance to the star. Clearly, the interstellar reddening in HD 331319 can be significant, because its Galactic latitude is low.

The typical accuracy of determining the model parameters (on average) for a star with a temperature of ≈7500 K is $\Delta T_{\rm eff} \approx 100$ K, $\Delta \log g \approx 0.3$ dex, and $\Delta\xi_{\rm t} \approx 0.5$ km s^{-1}. Most of the lines used to compute the chemical composition have equivalent widths less than 100 mÅ, which makes heavy demands on the accuracy of the observational data. The scatter of the elemental abundances derived from the set of lines is modest: the rms deviation σ typically does not exceed 0.25 dex (Table 2). All our calculations were performed with the WIDTH9 software package developed by Tsymbal (1996) in the LTE approximation. The corrections for hyperfine structure and isotopic shifts, which broaden the Ni I, Mn I, and Ba II lines, were disregarded.

To check the reliability of our determination of the model-atmosphere parameters for HD 331319, we compared the observed spectrum of the object with its synthetic spectrum computed by using the STARSP code (Tsymbal 1996). The observed and theoretical spectra are compared in Fig. 1. For low- and medium-intensity absorption features, the agreement is satisfactory.

Table 3. Relative elemental abundances $[X/{\rm Fe}]$ in the atmospheres of the stars under study

Species	*HD* 331319	HD 161796	
	[Fe/H] = −0.25	−0.25	−0.32*
He I	+1.63	–	–
C I	+0.12	+0.21	+0.21
N I	+1.30	+0.90	+1.19
O I	+0.64	+0.53	+0.40
Na I	+0.31	+0.32	+0.51
Mg I	−0.12	−0.07	+0.75
Al I	−0.29	−0.02	–
Si I	+0.44	–	+0.45
Si II	+0.57	–	–
S I	+0.38	+0.50	+0.73
Ca I	−0.18	−0.09	−0.04
Sc II	−0.52	−0.49	−0.40
Ti II	−0.44	–	−0.47
V II	−0.39	–	–
Cr I	−0.16	–	–
Cr II	+0.08	–	+0.41
Mn I	−0.34**	–	–
Ni I	+0.19	+0.28	+0.53
Cu I	+0.25	+0.27	–
Zn I	+0.03	+0.28	+0.56
Y II	−0.78	–	−0.32
Zr II	−0.58	–	+0.12
Ba II	−0.47	−0.26	–
La II	+0.26	–	–
Ce II	+0.11	–	–
Nd II	+0.03	+0.33	+0.18
Eu II	+0.26	−0.24**	+0.15

* The data from Luck *et al.* (1990).

** Uncertain values.

3. DISCUSSION

3.1. Chemical Composition

For an enhanced helium abundance, the term 'elemental abundance' must be refined. In our algorithm for determining the chemical composition (Kurucz 1970; Tsymbal 1996), the abundance of a given element by the number of particles is normalized to the total number of atoms of all elements. Therefore, replacing a considerable fraction of hydrogen atoms with helium atoms does not lead to a renormalization of the abundances of the remaining chemical elements. The only case where a stipulation is required

Table 4. Atmospheric light-element abundances $\epsilon(X)$ for HD 331319

λ	W, mÅ	$\log gf$	$\epsilon(X)$
He I 4471.473	64	−0.28	12.61
4713.140	28	−1.23	12.85
4921.930	20	−0.44	12.01
5875.620	38	0.41	12.55
7065.180	6	−0.46	12.73
C I 4775.900	37	−2.15	8.28
4817.370	15	−2.51	8.21
5039.050	38	−2.10	8.23
5041.660	111	−1.99	8.73
5052.150	103	−1.51	8.35
5380.320	56	−1.76	8.23
6014.840	11	−1.71	8.15
6108.530	6	−2.58	8.91
6587.620	59	−1.22	8.41
6605.800	9	−2.31	8.83
6711.300	8	−2.47	8.70
6828.120	33	−1.51	8.41
7085.470	4	−2.31	8.33
7100.300	45	−1.60	8.74
7108.940	45	−1.68	8.82
7111.480	64	−1.32	8.65
7113.180	87	−0.93	8.45
7115.190	92	−0.90	8.45
7116.990	92	−1.08	8.64
7119.670	58	−1.31	8.58
N I 7423.640	175	−0.61	9.09
7442.290	183	−0.31	8.85
7468.310	251	−0.13	9.17
O I 6155.980	131	−0.66	9.31
6156.770	144	−0.44	9.18
6158.180	151	−0.29	9.08

Note: The results of our calculations using spectrum s27608: $T_{\rm eff} = 7300$ K, $\log g = 0.5$, $\xi_t = 6.0$ km s^{-1}.

is the use of the designation [Fe/H] for HD 331319: it implies the Fe abundance measured for HD 331319 relative to the total number of H and He atoms, i.e., [Fe/H + He], but considered relative to Fe/H in the solar atmosphere. The meaning of all [X/Fe], which characterize the shape of the abundance curve, remains as before.

The elemental abundances $\log \epsilon(X) \pm \sigma$ averaged over the set of measured lines for the stars under study are given in Table 2. The second column in this table contains the corresponding data from Grevesse *et al.* (1996) for the solar atmosphere; we used these data to determine the relative abundances

$$[X/\mathrm{Fe}] = [\log \epsilon(X) - \log \epsilon(Fe)]_\star$$
$$= [\log \epsilon(X) - \log \epsilon(\mathrm{Fe})]_\odot,$$

required to analyze the abundance curve. Below, we consider the abundance pattern in the atmospheres of the two stars under study (see Tables 2 and 3).

Helium. The He I λ5876-Å line in the spectrum of HD 331319 was reliably measured for all epochs of observations: the mean equivalent width is $W = 38$ mÅ. We also detected other He I lines. Table 4 gives data on the measured He I lines in spectrum s27608 together with the computed abundances. All the parameters of He I lines and lines of other elements in the vicinity of the He I lines that are required for our calculations were taken from the VALD database (Piskunov *et al.* 1995). The average helium abundance, $\epsilon(\mathrm{He}) = 12.69$, for HD 331319 significantly exceeds its solar value, $\epsilon(\mathrm{He})_\odot = 10.99$. This result needs to be comprehensively verified.

First, note that helium lines have been repeatedly observed in the spectra of post-AGB stars. Waelkens *et al.* (1992) detected the He I λ4471-Å line with the equivalent width $W = 23$ mÅ in the spectrum of HD 44179 (the central star of the Red Rectangle Nebula), which led the authors to conclude that the atmospheric helium is significantly enhanced. Van Winckel *et al.* (1996a) detected the He I $\lambda = 5876$-Å line with the equivalent width $W = 38$ mÅ in the spectrum of HD 187885. The helium abundance in the atmosphere of HD 187885 with an effective temperature of ≈7700 K is significantly enhanced compared to its solar value. The above authors also ascribed a photospheric origin to the line. We measured the equivalent width of He I λ5876 Å in the spectrum of HD 187885, $W = 40$ mÅ, which is in excellent agreement with the data of Van Winckel *et al.* (1996a). Waelkens *et al.* (1991) reported on their measurement of the equivalent width $W = 15$ mÅ for He I λ4471 Å in the spectrum of HR 4049 with an effective temperature $T_{\rm eff} \approx 7500$ K. Van Winckel *et al.* (1996b) detected a very weak He I λ5876-Å line in the spectrum of the hotter ($T_{\rm eff} \approx 7800$ K) post-AGB star HD 133656, which led these authors to conclude that the helium abundance was solar. Having detected this line in the spectrum of HD 44179, we confirmed the result of Waelkens *et al.* (1992). Portions of the spectra for HD 187885, HD 331319, and HD 44179 with the $\lambda = 5876$-Å line are shown in Fig. 3. Since we took the spectrum of HD 187885 ($\delta < -17°$) on June 5, 1996, with the PFES spectrometer at a large zenith distance, apart from stellar lines, numerous telluric lines are seen near the Na I doublet.

A conventional explanation of why there are helium lines in the spectra of cool stars is the assumption of an elevated excitation temperature, including the chromospheric hypothesis. The excitation temperature (or the effective temperature of a model atmosphere) can be estimated from line intensity ratios: if the lines are weak, then these ratios are only slightly sensitive to the elemental abundance. An extrapolation of the results by Auer and Mihalas (1973) to lower temperatures can be used to roughly estimate the equilibrium temperature. By analyzing the ratios of the singlet/triplet (4921/4471, 4921/5876, 4921/7065) equivalent widths and the triplet/triplet (5876/4471, 7065/4471) ratios, we conclude that the observed equivalent-width ratios correspond to temperatures that are no higher than 9000 K. The 4921/4713 and 4713/4471 ratios that contain the $\lambda = 4713$-Å line intensity give an uncertainty. An analysis of the catalog of He I lines in the spectra of 492 stars (Klochkova and Panchuk 1987, 1989) shows that the $\lambda = 4713$-Å line is unsatisfactorily described by the calculations of Auer and Mihalas (1973) in the LTE and non-LTE approximations (the observed values are almost twice the theoretical ones); therefore, we excluded the $\lambda = 4713$-Å line from our analysis. Thus, we find from the line intensity ratios that the He I level excitation temperature cannot exceed 9000 K in the LTE approximation, i.e., the hypothesis of a photospheric origin for the He I lines in HD 331319 is not rejected.

He I lines are enhanced in several massive A supergiants, which can be interpreted in terms of the model with a temperature inversion in the chromosphere [an estimate of the effect for the A0 Ia supergiant HD 7583 can be found in Wolf (1973)]. As applied to the low-mass F supergiant HD 331319, this hypothesis raises objections. First, even in the A2 Ia supergiant HD 160529, the variable Fe II lines that show splitting and the appearance of an emission component (Wolf 1974) are considered to be evidence of a chromosphere, which is not observed in the A0 Ia supergiant. When passing to an F supergiant, the chromospheric Fe II components must grow. However, both in disk F supergiants (Klochkova and Panchuk 1988a) and in HD 331319, we observe only normal photospheric Fe II lines. Second, the presence of a chromosphere in the A3 Ia supergiant HD 33579 is accompanied by the asymmetry of all absorption lines that was found by Wolf (1972) with a spectral resolution lower than that in our study. For HD 331319, we found neither a line asymmetry nor a radial-velocity gradient. Third, line variability is considered to be evidence of the chromospheric contribution to the He I 5876-Å intensity, which is not observed in the spectra of HD 331319. Thus, there is no reason to suggest the presence in HD 331319 of a chromosphere similar to that discovered in A supergiants. Fourth, in the solar chromosphere, the triplet He I levels are an order of magnitude overpopulated compared to the singlet levels (Thomas and Athay 1961). By contrast, we observe an equilibrium population of the triplet and singlet levels in HD 331319 (see above) or at least equal singlet and triplet excitation temperatures. The observation of singlets with a highly reduced chromospheric contribution is the strongest evidence for the photospheric origin of the He I line.

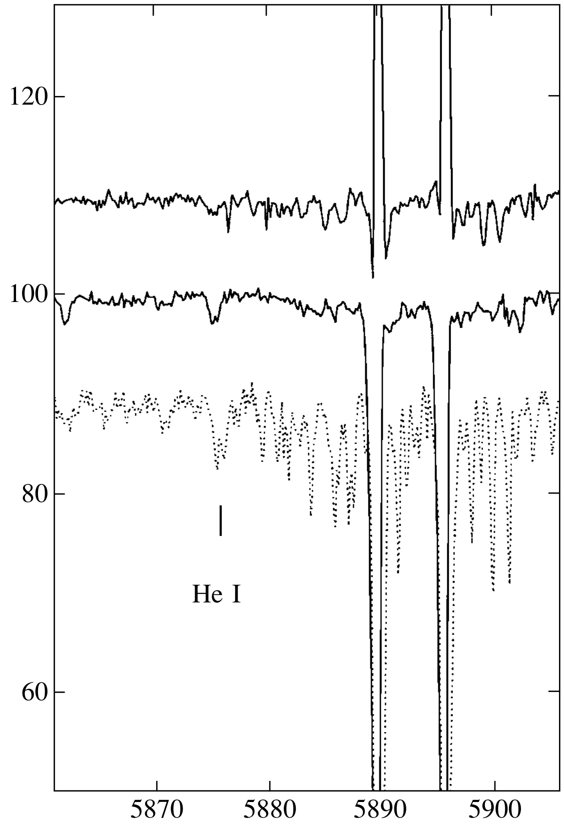

Fig. 3. A wavelength range with the He 5876-Å line and the sodium doublet in the spectra of three post-AGB stars, as constructed from our observations, from top to bottom: HD 187885, HD 331319, and HD 44179 (Red Rectangle). The spectrum of HD 187885 exhibits many telluric lines because of the large zenith distance of the star during our observations with the 6-m telescope.

Light elements. There is no Li I 6707-Å line in the spectrum of HD 331319, which can apparently be explained by the total lithium destruction under convection conditions. In the spectrum of HD 161796, this line is very weak, but its equivalent width is measurable, $W = 3$ mÅ.

We reliably determined the carbon abundance [C/Fe] = +0.12 in the spectrum of HD 331319 from 22 C I lines. For He and CNO lines, Table 4 gives the measured and computed abundances for individual lines in one of the spectra (s27608). The derived carbon and helium abundances for HD 331319 are in good agreement with the [C/H]–[He/H] relation for B and A supergiants [see Fig. 12 in Takeda and Takada-Hidai (2000)]. The data of Waelkens *et al.* (1991) for the post-AGB star HD 52961 agree with this relation.

The N I 7423, 7442, and 7468-Å lines are also strong in the spectrum of HD 331319. Since their equivalent widths reach 200 mÅ, the nitrogen overabundance was determined reliably.

The oxygen abundance ([O/Fe] = +0.64) was computed by using the reliably measured O I lines at 6155 Å (see Table 4). The IR triplet lines are very strong in the spectrum of HD 331319, with their total equivalent width being $W = 2.6$ Å. Therefore, we did not use the triplet lines to determine the mean oxygen abundance, because in the LTE approximation, the oxygen abundance is derived from these lines for F supergiants with a very large systematic error (Gratton *et al.* 1999).

The revealed overabundances of the helium-burning products (carbon and oxygen) confirm the post-AGB stage for the two stars HD 161796 and HD 331319 under study. Note that our derived ratio $O/C > 1$ for HD 331319 is inconsistent with the absence of an OH band, as follows from radio observations of IRAS 19475 (Likkel 1989). According to the chronological sequence of Lewis (1989), the absence of an OH band in the spectrum of IRAS 19475 suggests that the object is close to the planetary nebula stage. At the same time, IRAS 17436 radiates in the masing OH 1667-MHz line, which is consistent with the atmospheric oxygen overabundance in the central star and which may point to an earlier time on the evolutionary path toward a planetary nebula. The presence of OH bands indicates an oxygen enrichment of the envelope. However, as Omont *et al.* (1993) emphasized, the absence of these bands only suggests a carbon enrichment of the envelope but cannot serve as its evidence.

Element separation in the envelope. The object IRAS 19475 under study may be at the stage of intense mass transfer between the atmosphere and the circumstellar gas–dust envelope. The mere fact of a nearly solar iron abundance suggests that there are no severe distortions of the elemental abundances by condensation onto dust grains, because iron belongs to the elements with the most efficient settling on grains (Bond 1992). The CNO-group elements, sulfur, and zinc, which are essentially not subject to fractionation, exhibit a normal abundance (Bond 1992). Since the CNO abundances can change through nuclear reactions in the course of stellar evolution, the behavior of zinc and sulfur is critical in estimating the efficiency of selective separation.

A normal (relative to iron) zinc abundance, [Zn/Fe] = +0.03, was derived for HD 331319 from three lines, while in HD 161796, zinc is overabundant. The zinc abundance, which does not change during the stellar nucleosynthetis in the interiors of low- and intermediate-mass stars, varies by the same amount as the iron abundance over a wide metallicity range (Wheeler *et al.* 1989). Consequently, the conclusion regarding a zinc overabundance does not depend on the scale on which it was obtained (differential or absolute). This fact in combination with the normal ratio [Zn/Fe] = +0.03 leads us to conclude that there is no selective separation in the circumstellar envelope of IRAS 19475.

The sulfur abundance in the spectra of evolved stars seems to be a problem of its own. Bond and Luck (1987) found a large ([S/Fe] = +1.2) sulfur overabundance in the atmosphere of the metal-poor post-AGB star HD 46703 and explained it by the probable synthesis of sulfur through the attachment of α particles to C^{12} nuclei. However, Klochkova (1995) also discovered a sulfur overabundance in the atmosphere of the normal massive supergiant α Per. This star, on the one hand, has no circumstellar envelope and no condensation and, on the other hand, it would be unreasonable to expect any manifestations of the sulfur synthesis at such an early evolutionary stage. A sulfur overabundance seems to be a stable feature in the abundance pattern of evolved stars. In the atmospheres of unevolved stars, sulfur is also enhanced relative to iron (Timmes *et al.* 1995).

Light metals. Consider the behavior of the light-metal abundances for HD 331319. Sodium is slightly enhanced in the atmosphere of HD 331319, [Na/Fe] = +0.31, which could be a manifestation of the sodium synthesis during hydrogen burning. Mashonkina *et al.* (2000) showed that for a luminous star with $T_{\rm eff} \approx 7200$ K, allowance for sodium overionization results in sodium-abundance corrections of ≈ -0.15 dex compared to the LTE approximation for subordinate lines.

From the α-process elements, apart from sulfur, we determined the silicon, calcium, and titanium abundances. The abundance pattern in the atmospheres of HD 331319 and HD 161796 (Table 3) clearly shows a slightly reduced calcium abundance and a more significant underabundance of scandium and titanium with differences in the zinc abundance.

The silicon overabundance, [Si/Fe] = +0.5, was reliably determined for HD 331319 from two ionization states. Since only one, very strong Si II 6347-Å line was measured in the spectrum of HD 161796, the Si abundance was not determined for this star. However, Luch *et al.* (1990) give [SiI/Fe] = +0.45 for HD 161796, which is close to our value for HD 331319. Since the relative silicon abundance $[\mathrm{Si/Fe}]_\odot$ in the atmospheres of unevolved stars with solar metallicity is nearly solar (Timmes *et al.* 1995), our data suggest that silicon is enhanced in HD 161796 and HD 331319. The anomalous abundances of silicon, calcium, scandium, and titanium can be a manifestation of the initial chemical peculiarities in HD 331319.

Iron-peak elements. For the iron-group metals, the two stars have a similar abundance pattern (Table 3). The mean abundance of the iron-group metals (vanadium, chromium, nickel) differs little from the iron abundance: [Met/Fe] = −0.07 for HD 331319. At the same time, individual iron-group elements exhibit significant overabundances and underabundances relative to iron. The chromium abundance agrees with its solar value. However, nickel, whose abundance was determined from a large set of Ni I lines, is slightly overabundant relative to iron, which corresponds to available data for unevolved stars with a nearly solar metallicity (Timmes *et al.* 1995). Copper is slightly enhanced in both stars, [Cu/Fe] ≈ −0.25; since this ratio was determined from one or two lines, its significance is low.

Heavy elements. It is generally believed (Blöcker 2001) that heavy metals could be overabundant in the atmospheres of post-AGB stars through neutronization, mixing, and dredge-up of the material that passed through these processes in the stellar interiors to the surface. However, contrary to the expected overabundance, the atmospheric barium abundance in HD 331319 reliably determined from three lines was found to be reduced. The relative abundances of the lighter s-process metals Y and Zr was determined with a lower accuracy because of the limited set of lines, but, in general, these metals can be said to be underabundant relative to iron, [s/Fe] = −0.68. For HD 161796, the light s-process metals Y and Zr (Luck *et al.* 1990) and Ba (our data) are also underabundant.

An underabundance of the s-process elements in the atmospheres of supergiants, including those at the post-AGB stage, is observed much more commonly than their overabundance (Klochkova and Panchuk 1988a, 1988b; Bond and Luck 1989; Van Winckel 1997; Klochkova 1998; Klochkova *et al.* 2001). We believe the observed lack of heavy-metal dredge-up manifestations to be real rather than the result of systematic errors in our analysis of the supergiant spectra by the model-atmosphere method. The presence or absence of an s-process underabundance is most likely to be somehow related to such fundamental stellar parameters as the initial stellar mass and mass-loss rate, which determine the course of evolution for a specific star. In the opinion of García *et al.* (1999), the most massive and, hence, rapidly evolving post-AGB stars do not necessary have any s-process overabundances.

As for the group of heavier metals with $Z > 70$ (La, Ce, Nd, and Eu), which are predominantly synthesized in the r-process, our accuracy of determining their abundances is low because of the small number of weak lines. In general, however, these elements can be said to be slightly overabundant relative to iron, [heavy/Fe] = +0.16, in both stars.

Evolutionary manifestations of the chemical composition. Thus, neither lithium nor s-process elements were found to be overabundant in HD 331319. The only manifestation of the third dredge-up are the CNO-group overabundances. In general, the abundance pattern in the atmosphere of HD 331319 virtually coincides with that for the post-AGB standard HD 161796; except for an underabundance of the s-process metals, it is in good agreement with the views of a relatively massive star at the time of its post-AGB evolution. A substantial difference between HD 331319 and its counterpart is the presence of a significant helium overabundance in the atmosphere of this star. The high-latitude IR source IRAS 18095 + 2704, which Hrivnak *et al.* (1988) called the most likely PPN candidate, has similar characteristics [a similar abundance pattern (Klochkova 1995) and a featureless IR spectrum (Hrivnak *et al.* 1994)].

The spectral type of HD 331319 matches the spectral type F2–3 I determined by Parthasarathy *et al.* (1988) for HD 187885. These stars differ in metallicity only slightly: Van Winckel *et al.* (1996a) found iron to be slightly underabundant in HD 187885, [Fe/H] = −0.4. In addition, the atmospheres of both stars exhibit the same oxygen overabundance: [O/Fe] = +0.64, as inferred from our data for HD 331319, and [O/Fe] = +0.60 for HD 187885 from Van Winckel *et al.* (1996). This similarity is illustrated by Fig. 4, where portions of the spectra for HD 331319 and HD 187885 are compared.

While HD 331319 and HD 187885 are similar in metallicity and in helium and oxygen overabundances, there are also fundamental differences in the chemical compositions of these objects. HD 187885 has an atmosphere enriched with carbon (C/O > 1)

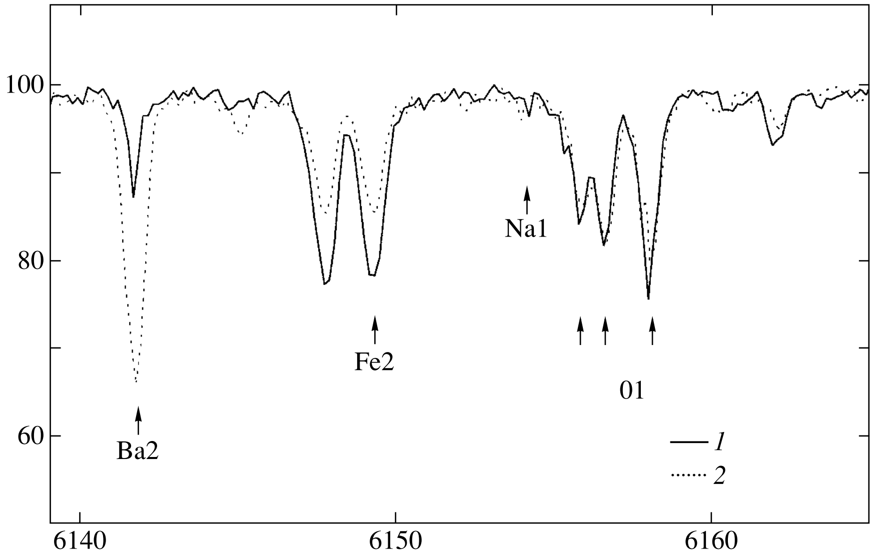

Fig. 4. A wavelength range with the O I ∼6155-Å line in the spectra of two post-AGB stars: HD 331319 (*1*) and HD 187885 (*2*).

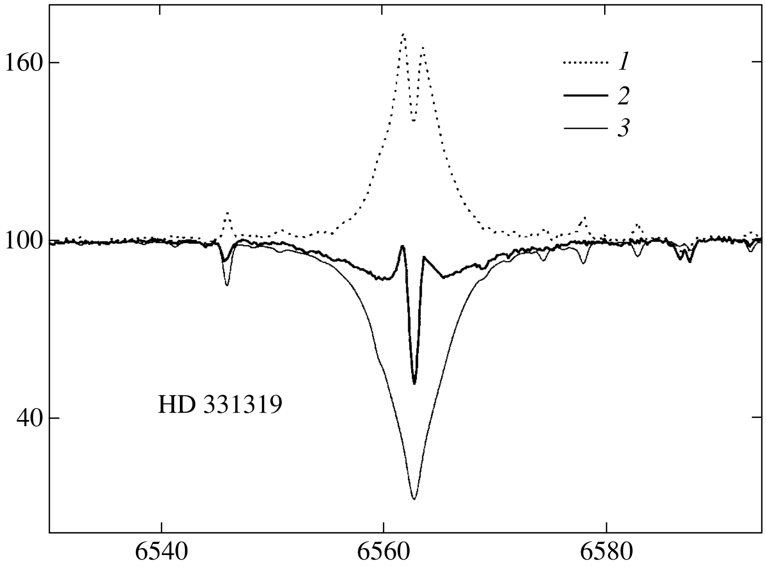

Fig. 5. Separating the emission (*1*) $H\alpha$ profile from the observed (*2*) spectrum of HD 331319. The synthetic spectrum is represented by a thin line.

and s-process metals. HD 187885 may be considered to be a standard post-AGB star whose atmosphere exhibits all the evolutionary changes in chemical composition that are expected at this stage. The IR spectra for the two compared stars also differ. The spectrum of the IR source IRAS 19500–1709, which is identified with HD 187885, shows a band near 21 μm that is absent in the spectrum of IRAS 19475. As was shown by Decin *et al.* (1998), Klochkova (1998), and Klochkova *et al.* (1999), there is a clear, but as yet incomprehensible relationship between the presence of the 21 μm band in the IR spectrum attributable to the circumstellar envelope and the existence of an atmospheric s-process overabundance in the central star.

3.2. Radial Velocities

To determine which type of Galactic population the object belongs to and to refine its evolutionary status requires additional information on its systemic velocity and on the velocity pattern in its atmosphere and envelope.

IRAS 19475 is a source of CO emission that originates in the expanding circumstellar envelope. Based on CO-band ($J = 1$–0) observations, Likkel *et al.* (1987) determined the systemic velocity of this source, $V_{\mathrm{lsr}} = 12$ km s^{-1}; Likkel *et al.* (1991) obtained $V_{\mathrm{lsr}} = 17.7$ km s^{-1} from CO-band ($J =$ 2–1) observations. These values are close to the mean $V_{\mathrm{lsr}}(\mathrm{met}) = 14.9$ km s^{-1} that we measured from metal lines. The derived equality between the radial velocities calculated for epochs separated by more than 10 years confirms our conclusion that the radial velocity of IRAS 19475 is nonvariable.

The $H\alpha$ line has a complex emission–absorption profile with absorption wings and two emission peaks with velocities that differ from the systemic velocity by -38 and $+54$ km s^{-1} (see Fig. 5 and Table 1). The velocity determined for the center of the $H\alpha$ emission profile is equal to the velocity of the narrow absorption component.

As we see from Fig. 2, the profiles of the resonance Na D1 and 2 doublet lines are an unresolvable (at our spectral resolution) blend that includes stellar and interstellar components. We emphasize that the velocity measured from the He I 5876-Å line is equal to the mean velocity, which confirms its formation in the stellar photosphere.

Apart from photospheric absorption lines, we also detected several strong absorption features in the spectrum of HD 331319 whose positions allowed them to be identified with diffuse interstellar bands (DIBs). The equivalent widths of the most easily identifiable λ5780 and λ6613-Å bands are $W = 262$ and 80 mÅ, respectively. The band identification technique is the same as that used by Klochkova *et al.* (2000). The mean radial velocities measured from several features of this kind in each spectrum of HD 331319 are given in Table 1; there are two sets of bands in the spectrum of HD 331319, one is interstellar in origin (IS in Table 1) and the other (CS in Table 1) originates with a high probability in the circumstellar envelope. The velocity determined from the interstellar component and corrected for solar motion toward the apex is $V_{\mathrm{lsr}}(\mathrm{IS}) = 6.4$ km s^{-1}. This value agrees with the results of Munüch (1957) for this direction in the Galaxy. Thus, the circumstellar absorption bands that were previously detected for several evolved stars (Cohen and Jones 1987; Le Bertre and Lequeux 1993; Klochkova *et al.* 2000 and references therein) were identified in the optical spectrum of yet another object (PPN candidate).

The difference between the radial velocities measured in the spectrum of HD 331319 from lines that originate in the photosphere and in the circumstellar envelope gives an envelope expansion velocity relative to the central star $V_{\mathrm{exp}} = 20.8$ km s^{-1}, which is a typical value for post-AGB stars. Our data on the expansion velocity obtained from optical lines and radio observations (Likkel *et al.* 1987, 1991) suggest that there is a velocity gradient in the circumstellar neighborhood of HD 331319, which is characteristic of low-mass post-AGB supergiants.

3.3. $H\alpha$ Profile

Even far from the core, where the distortion by emission features does not show up clearly, the $H\alpha$ profile completely disagrees with the theoretical profile that was computed with the model parameters T_{eff} and $\log g$ determined from the "metallic" spectrum of the star (Fig. 1). To explain such weak $H\alpha$ wings by the absorption alone requires lowering the effective temperature to the extent that the stellar metallicity will be one or two orders of magnitude larger than its solar value. Therefore, we propose to consider the observed $H\alpha$ profile as a superposition of two lines of different origin: a photospheric absorption component and an intense emission component with velocities in a wide range that originates in the circumstellar structure. In this case, the emission component can be separated from the observed profile by subtracting the theoretical photospheric profile from the observed one. If the photospheric profile computed using a model with a solar H/He ratio (indicated by the dotted line in Fig. 1) is subtracted from the observed profile, then the wings of the emission profile derived in this way extend to the radial velocities of ± 1300 km s^{-1}. If we subtract the photospheric profile computed for an enhanced helium abundance, as shown in Fig. 5, then velocities of ± 450 km s^{-1} correspond to the farthest parts of the emission wings.

The double-peaked shape of the $H\alpha$ emission component suggests that the star is surrounded by a rotating disk, as in Be stars. If the emission wings are assumed to be Doppler ones, then we reach the absurd conclusion that the envelope (disk) rotates faster than the star. The intensity of the $H\alpha$ emission statistically weakens when passing from Be- to Ae-stars simultaneously with decreasing mean projected rotational velocity, and the presence of $H\alpha$ emission in F stars is an exotic case. The emission-line width in the spectra of Be-stars correlates with the absorption-line width; $H\alpha$ whose excessive width is commonly explained by electron scattering (Marlborough 1969; Poeckert and Marlborough 1979) constitutes an exception. At a temperature of 10 000 K, the mean thermal electron velocity is ± 400 km s^{-1}. By combining this estimate with the disk projected rotational velocity, which we estimated from the radial velocities of emission peaks to be 40 km s^{-1}, we obtain the observed wing width ± 440 km s^{-1}.

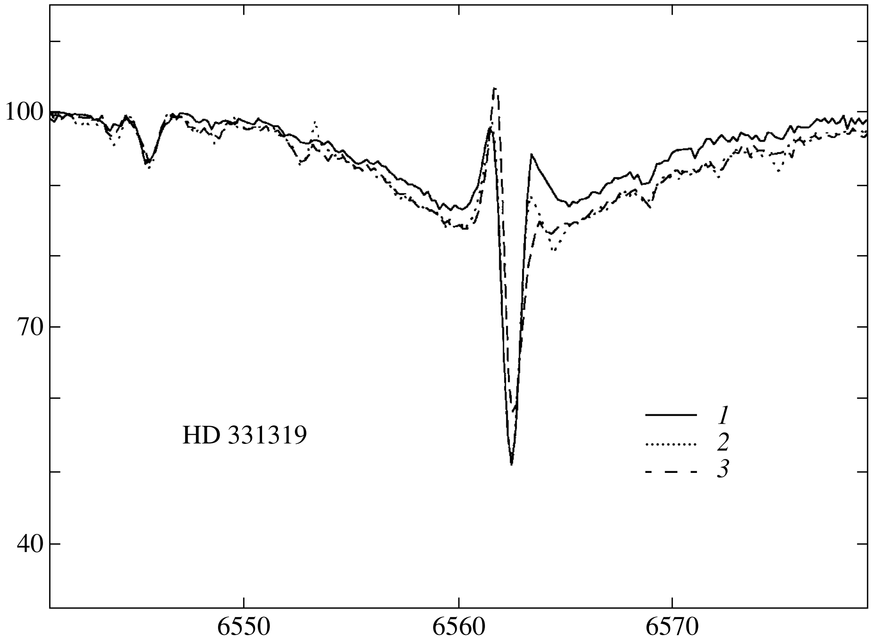

Fig. 6. Comparison of the $H\alpha$ profiles in the spectra of HD 331319 for three epochs of observations: (*1*) spectrum s261813, (*2*) spectrum s27323, and (*3*) spectrum s27608.

Observations show that the $H\alpha$ profile in the spectrum of HD 331319 changes with time: it follows from a comparison of the $H\alpha$ profiles for three dates in Fig. 6 that the intensity of the short-wavelength emission component increases simultaneously with decreasing intensity of the long-wavelength component.

3.4. Helium Atmosphere of an F Supergiant

The atmospheric structure of evolved stars with a changed H/He ratio has been previously considered by Sonneborn *et al.* (1979) in connection with the helium abundance in Cepheid envelopes and by Böhm-Vitense (1979) in connection with molecular-band intensity variations in globular-cluster giants. Since a changed helium abundance in the atmosphere of a post-AGB star is a reasonable assumption, we made some estimates.

For the temperature and luminosity of HD 331319, we used algorithms of solving the system of atomic ionization and molecular dissociation equations (Panchuk 1974) and algorithms of computing the continuum absorption coefficients (Panchuk 1975) for a gas mixture of 31 chemical elements. As a result, we obtained the following: when the helium abundance increases approximately by an order of magnitude, the combined effect on negative ions consists in reducing the absorption by two orders of magnitude at $\lambda < 1.67$ μm (at which the contribution of bound–free transitions to H^-) is largest and by one and a half orders of magnitude at $\lambda > 1.67$ μm, with the contribution from free–free transitions to He^- being triple the H^- contribution. The contribution of absorption by neutral hydrogen is minor. The Thompson scattering decreases in importance by an order of magnitude because of the reduction in electron density. The Rayleigh scattering by helium atoms, with a small addition of scattering by carbon atoms, will dominate, but the total scattering coefficient will decrease approximately by a factor of 4 and will be insignificant compared to absorption even in the ultraviolet.

Our synthetic-spectrum calculations show that a general increase in the photospheric transparency causes the effective formation depths of weak lines and the wings of strong lines to increase. When gradually increasing the helium abundance, the wings of the Balmer hydrogen lines first strengthen (the Stark effect is stronger in denser atmospheric layers) and then weaken. Since denser layers are added to the line-forming region, the strengthening rates for metal and ionic lines are different. Our calculations indicate that the increase in mass of the absorbing layer above the photosphere, which results from the atmosphere becoming optically thin, is a few tenths of dex, and in no way can it offset the helium overabundance (1.6 dex) derived, to a first approximation, by using a model atmosphere with a solar H/He ratio. The computational effect of line strengthening clearly shows up for atomic lines of those elements that are predominantly in the ionized state (Li, Na). It may well be that some of the individual chemical differences between post-AGB stars in the abundances of easily ionizable elements are attributable to variations in the atmospheric helium abundance of these stars.

3.5. The Temperature of HD 161796

We derived the same metallicity, [Fe/H] $= -0.25$, for both stars, HD 331319 and HD 161796. Based on the photographic spectrum of HD 161796 taken on August 1986, Klochkova and Panchuk (1988b) obtained $T_{\text{eff}} = 6200$ K. Using a similar (spectroscopic) method of determining model parameters, Luck *et al.* (1990) derived the effective temperature $T_{\text{eff}} = 6600$ K and metallicity [Fe/H] $= -0.32$ for HD 161796 from 1983–1986 spectrograms. The echelle spectrum taken on August 1993 yielded $T_{\text{eff}} = 7100$ K, which significantly differs from the results for the mid-1980s. Thus, while the metallicities of HD 161796 are equal, within the accuracy of the method, the effective temperatures at different epochs differ significantly. This difference points to an evolutionary manifestation of the central star in IRAS 17436 when passing from AGB to a planetary-nebula nucleus. We believe that the effective temperature of the central star in IRAS 17436 increases at a mean rate of at least 50° per year.

4. CONCLUSIONS

We have presented the results of our spectroscopic analysis for the supergiant HD 331319, an optical counterpart of the IR source IRAS 19475 + 3119: we determined the model-atmosphere parameters, computed the detail chemical composition, and measured the radial velocities from various spectral features. The most important peculiarity of the optical spectrum for HD 331319 is a strong emission feature in the $H\alpha$ line and the presence of the reliably measured He I λ5876-Å absorption line with the mean equivalent width $W = 38$ mÅ in all spectra, which at a low temperature of the star suggests a large atmospheric helium overabundance, [He/Fe] $= +1.63$.

The detected small iron underabundance in the atmosphere of HD 331319, [Fe/H] $= -0.25$, reflects the initial chemical composition of the star, because the selective separation of elements in its circumstellar envelope was shown to be inefficient. The revealed overabundances of the helium-burning products (carbon and oxygen) suggest that the star HD 331319, whose optical spectrum has been studied for the first time, is at the post-AFB stage.

The metallicity in combination with the radial velocity and Galactic latitude of the object indicate that it belongs to the Galactic disk population. The envelope expansion velocity was found from the positions of the absorption bands originating in the circumstellar envelope to be $V \approx 21$ km s^{-1}.

For HD 161796, which we consider as a typical and well-studied PPN candidate with parameters similar to those of the object under study, we found an evolutionary increase in the stellar effective temperature at a mean rate of 50° per year.

ACKNOWLEDGMENTS

The program of spectroscopic research on objects evolving away from AGB stars toward planetary nebulae with the 6-m telescope was supported by the Russian Foundation for Basic Research (project no. 99-02-18339) and the Federal Program "Astronomy" (project nos. 1.4.1.1 and 2.1.5.5). We used the SIMBAD, CDS, and VALD databases. The study whose results are presented here was supported, in particular, by the American CRDF Foundation (project no. RP1-2264).

REFERENCES

1. L. H. Auer and D. Mihalas, Astrophys. J., Suppl. Ser. **25**, 433 (1973).
2. E. Böhm-Vitense, Astrophys. J. **234**, 521 (1979).
3. T. Blöcker, Astrophys. Space Sci. **275**, 241 (2001).
4. H. E. Bond, Nature **356**, 474 (1992).
5. H. E. Bond and R. E. Luck, Astrophys. J. **312**, 203 (1987).
6. H. E. Bond and R. E. Luck, Astrophys. J. **342**, 476 (1989).
7. M. Cohen and B. F. Jones, Astrophys. J. Lett. **321**, L151 (1987).
8. L. Decin, H. Van Winckel, C. Waelkens, *et al.*, Astron. Astrophys. **332**, 928 (1998).
9. G. A. Galazutdinov, Preprint No. 92 (Spets. Astrofiz. Obs., 1992).
10. P. García, F. D'Antona, J. Lub, B. Plez, and H. J. Habing, in *Proceedings of the 191st Symposium of International Astromonical Union "Asymptotic Giant Branch Stars," 1999,* Ed. by T. Le Bertre *et al.*, p. 91.
11. R. G. Gratton, E. Caretta, K. Eriksson, and B. Gustafsson, Astron. Astrophys. **350**, 955 (1999).
12. N. Grevesse, A. Noels, and A. J. Sauval, Astron. Soc. Pac. Conf. Ser. **99**, 117 (1996).
13. B. J. Hrivnak, S. Kwok, and K. M. Volk, Astrophys. J. **331**, 832 (1988).
14. B. J. Hrivnak, S. Kwok, and T. R. Geballe, Astrophys. J. **420**, 783 (1994).
15. V. G. Klochkova, Mon. Not. R. Astron. Soc. **272**, 710 (1995).
16. V. G. Klochkova, Bull. Spec. Astrophys. Obs. **44**, 5 (1998).
17. V. G. Klochkova and G. A. Galazutdinov, Preprint No. 71 (Spets. Astrofiz. Obs., 1991).
18. V. G. Klochkova and V. E. Panchuk, Soobshch. Spets. Astrofiz. Obs. **54**, 5 (1987).

19. V. G. Klochkova and V. E. Panchuk, Pis'ma Astron. Zh. **14**, 933 (1988a) [Sov. Astron. Lett. **14**, 395 (1988a)].
20. V. G. Klochkova and V. E. Panchuk, Pis'ma Astron. Zh. **14**, 77 (1988b) [Sov. Astron. Lett. **14**, 32 (1988b)].
21. V. G. Klochkova and V. E. Panchuk, Astrofiz. Issled. **27**, 25 (1989).
22. V. G. Klochkova and V. E. Panchuk, Bull. Spec. Astrophys. Obs. **41**, 5 (1996).
23. V. G. Klochkova, R. Szczerba, V. E. Panchuk, and K. Volk, Astron. Astrophys. **345**, 905 (1999).
24. V. G. Klochkova, R. Szczerba, and V. E. Panchuk, Pis'ma Astron. Zh. **26**, 510 (2000) [Astron. Lett. **26**, 439 (2000)].
25. V. G. Klochkova, V. E. Panchuk, and R. Szczerba, Astrophys. Space Sci. **275**, 265 (2001).
26. R. L. Kurucz, Smithsonian Astrophysical Observatory Special Report No. 309 (1970).
27. R. L. Kurucz, CDROMs (Smithsonian Astrophysical Observatory, Cambridge, 1993).
28. T. Le Bertre and J. Lequeux, Astron. Astrophys. **274**, 909 (1993).
29. L. Likkel, Astrophys. J. **344**, 350 (1989).
30. L. Likkel, A. Omont, M. Morris, and T. Forveille, Astron. Astrophys. **173**, L11 (1987).
31. L. Likkel, T. Forveille, A. Omont, and M. Morris, Astron. Astrophys. **246**, 153 (1991).
32. B. M. Lewis, Astrophys. J. **338**, 234 (1989).
33. C. Loup, T. Forveille, A. Omont, and J. F. Paul, Astron. Astrophys., Suppl. Ser. **99**, 291 (1993).
34. R. E. Luck, H. E. Bond, and D. L. Lambert, Astrophys. J. **357**, 188 (1990).
35. J. M. Marlborough, Astrophys. J. **156**, 135 (1969).
36. L. I. Mashonkina, V. V. Shimanskiĭ, and N. A. Sakhibullin, Astron. Zh. **77**, 893 (2000) [Astron. Rep. **44**, 790 (2000)].
37. G. Münch, Astrophys. J. **125**, 42 (1957).
38. A. Omont, C. Loup, T. Forveille, *et al.*, Astron. Astrophys. **267**, 515 (1993).
39. V. E. Panchuk, Astrometr. Astrofiz. **22**, 37 (1974).
40. V. E. Panchuk, Astrometr. Astrofiz. **25**, 20 (1975).
41. V. E. Panchuk, I. D. Najdenov, V. G. Klochkova, *et al.*, Bull. Spec. Astrophys. Obs. **44**, 127 (1998).
42. M. Parthasarathy, S. R. Pottash, and W. Wamsteker, Astron. Astrophys. **203**, 117 (1988).
43. N. E. Piskunov, F. Kupka, T. A. Ryabchikova, *et al.*, Astron. Astrophys., Suppl. Ser. **112**, 525 (1995).
44. R. Poeckert and J. M. Marlborough, Astrophys. J. **233**, 259 (1979).
45. D. J. Slowik and D. M. Peterson, Astron. J. **109**, 2193 (1995).
46. G. Sonneborn, T. J. Kuzma, and G. W. Collins, Astrophys. J. **232**, 807 (1979).
47. Y. Takeda and M. Takada-Hidai, Publ. Astron. Soc. Jpn. **52**, 113 (2000).
48. R. N. Thomas and R. G. Athay, *Physics of the Solar Chromosphere* (Interscience, London, 1961; Mir, Moscow, 1965).
49. F. X. Timmes, S. E. Woosley, and T. Weaver, Astrophys. J., Suppl. Ser. **98**, 617 (1995).
50. V. Tsymbal, Astron. Soc. Pac. Conf. Ser. **108**, 198 (1996).
51. C. Waelkens, H. van Winckel, E. Bogaert, and N. R. Trams, Astron. Astrophys. **251**, 495 (1991).
52. C. Waelkens, H. van Winckel, N. R. Trams, and L. B. F. M. Waters, Astron. Astrophys. **256**, L15 (1992).
53. J. C. Wheeler, C. Sneden, and J. W. Truran, Annu. Rev. Astron. Astrophys. **27**, 279 (1989).
54. H. van Winckel, Astron. Astrophys. **319**, 561 (1997).
55. H. van Winckel, C. Waelkens, and L. B. F. M. Waters, Astron. Astrophys. **306**, L37 (1996a).
56. H. van Winckel, R. D. Oudmaijer, and N. R. Trams, Astron. Astrophys. **312**, 553 (1996b).
57. B. Wolf, Astron. Astrophys. **20**, 275 (1972).
58. B. Wolf, Astron. Astrophys. **28**, 335 (1973).
59. B. Wolf, Astron. Astrophys. **36**, 87 (1974).
60. K. Young, T. G. Phillips, and G. R. Knapp, Astrophys. J., Suppl. Ser. **86**, 517 (1993).

Translated by V. Astakhov

Astronomy Letters, Vol. 28, No. 1, 2002, pp. 63–67. Translated from Pis'ma v Astronomicheskiĭ Zhurnal, Vol. 28, No. 1, 2002, pp. 71–75.
Original Russian Text Copyright © 2002 by Agekyan, Orlov.

Motion in the Field of a Rotationally Symmetric Potential: Exact Use of an Approximate Equation for the Derivative of the Field of Directions along the Normal to a Trajectory

T. A. Agekyan and V. V. Orlov[*]

Astronomical Institute, St. Petersburg State University, Bibliotechnaya pl. 2, Petrodvorets, 198904 Russia

Received July 30, 2001

Abstract—The previously derived equation (Agekyan 1974) for the derivative $\partial f/\partial n$ of the field of directions along the normal to a trajectory is approximate, because differentiating along the normal takes the point out of the orbit and changes the third integral of motion. However, on the envelope of the trajectory, i.e., on the contour of an orbit or a fold, $\partial f/\partial n$ undergoes a discontinuity of the second kind. Many authors have used this property to find points of the contours of orbits and folds. Although the integrable equation is approximate, the envelope points are determined accurately. *© 2002 MAIK “Nauka/Interperiodica”.*

Key words: *rotationally symmetric potential, particle orbits*

The exact equation for a particle trajectory in the meridional plane (R, z) of a rotationally symmetric potential is

$$\frac{\partial f}{\partial l} = \frac{\partial f}{\partial R}\cos f + \frac{\partial f}{\partial z}\sin f \tag{1}$$
$$= \frac{1}{2(U+I)}\left(-\frac{\partial U}{\partial R}\sin f + \frac{\partial U}{\partial z}\cos f\right) = 0,$$

where f is the angle between the tangent to the trajectory in the meridional plane and the R axis, $U(R, z)$ is the rotationally symmetric potential reduced to the meridional plane, and I is the energy integral. Equation (1) can be derived directly from the equations of particle motion.

Given the form of the potential $U(R, z)$, I, and the angle f at point (R, z) of the region of possible motions

$$U(R, z) + I \geq 0, \tag{2}$$

Eq. (1) defines the particle orbit and the unknown third integral of motion.

The equation

$$\frac{\partial f}{\partial n} = -\frac{\partial f}{\partial R}\sin f + \frac{\partial f}{\partial z}\cos f \tag{3}$$

is not exact, because differentiating along the normal to the trajectory takes the point out of the orbit and, hence, does not conserve the third integral of motion.

Differentiating Eqs. (1) and (3) along the tangent and normal to the trajectory, respectively, yields the following two approximate equalities:

$$\frac{\partial}{\partial l}\frac{\partial f}{\partial n} = \left(-\frac{\partial^2 f}{\partial R^2}\sin f + \frac{\partial^2 f}{\partial R\partial z}\cos f\right)\cos f \tag{4}$$
$$+ \left(-\frac{\partial^2 f}{\partial R\partial z}\sin f + \frac{\partial^2 f}{\partial z^2}\cos f\right)\sin f$$
$$+ \left(-\frac{\partial f}{\partial R}\cos f - \frac{\partial f}{\partial z}\sin f\right)$$
$$\times \frac{1}{2(U+I)}\left(-\frac{\partial U}{\partial R}\sin f + \frac{\partial U}{\partial z}\cos f\right),$$

$$\frac{\partial}{\partial n}\frac{\partial f}{\partial l} \tag{5}$$
$$= \frac{\partial}{\partial n}\left[\frac{1}{2(U+I)}\left(-\frac{\partial U}{\partial R}\sin f + \frac{\partial U}{\partial z}\cos f\right)\right]$$
$$= \left(\frac{\partial^2 f}{\partial R^2}\cos f + \frac{\partial^2 f}{\partial R\partial z}\sin f\right)(-\sin f)$$
$$+ \left(\frac{\partial^2 f}{\partial R\partial z}\cos f + \frac{\partial^2 f}{\partial z^2}\sin f\right)\cos f$$
$$+ \left(-\frac{\partial f}{\partial R}\sin f + \frac{\partial f}{\partial z}\cos f\right)\frac{\partial f}{\partial n}.$$

Let us subtract Eq. (5) from Eq. (4). Given (1) and (3), we obtain

$$\frac{\partial}{\partial l}\frac{\partial f}{\partial n} - \frac{\partial}{\partial n}\left[\frac{1}{2(U+I)}\left(-\frac{\partial U}{\partial R}\sin f\right.\right. \tag{6}$$

---

[*] E-mail: `vor@astro.spbu.ru`

1063-7737/02/2801-0063$22.00 © 2002 MAIK “Nauka/Interperiodica”

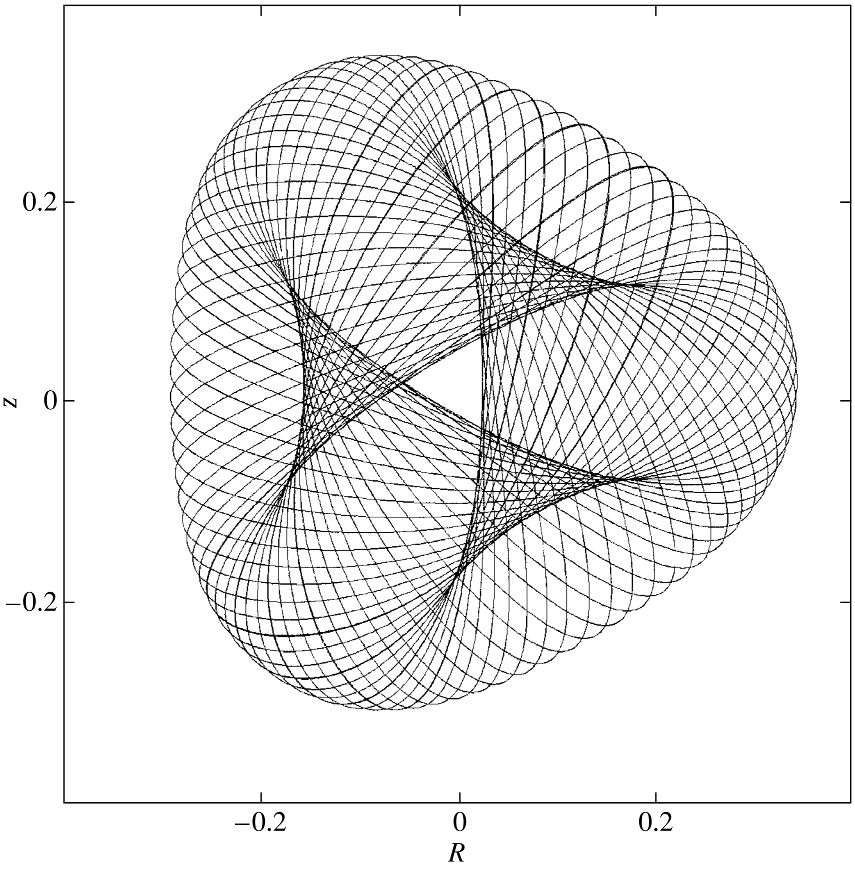

Fig. 1. Particle trajectory in the potential of Henon and Heiles (1964): $A = 1$, $B = 1$, $\varepsilon = -1$, $\mu = 1/3$, and energy integral $I = 0.051$. The starting-point coordinate is $R_0 = -0.15$.

$$+\left.\left.\frac{\partial U}{\partial z}\cos f\right)\right] = \frac{1}{4(U+I)^2}\left(\frac{\partial U}{\partial n}\right)^2 - \left(\frac{\partial f}{\partial n}\right)^2.$$

The final form of the approximate equation for $\partial f/\partial n$ is

$$\frac{\partial}{\partial l}\frac{\partial f}{\partial n} + \left(\frac{\partial f}{\partial n}\right)^2 + \frac{1}{2(U+I)}\frac{\partial U}{\partial l}\frac{\partial f}{\partial n} \qquad (7)$$

$$+\frac{3}{4(U+I)^2}\left(\frac{\partial U}{\partial n}\right)^2 + \frac{1}{2(U+I)}\gamma = 0,$$

where

$$\gamma = -\frac{\partial^2 U}{\partial R^2}\sin^2 f + 2\frac{\partial^2 U}{\partial R\partial z}\sin f\cos f \qquad (8)$$

$$-\frac{\partial^2 U}{\partial z^2}\cos^2 f.$$

Equation (7) is approximate, because its derivation involved differentiating along the normal to the trajectory.

Agekyan and V'yuga (1973) and Saginashvili (1974), who analyzed the motion of a particle in the Newtonian and Hooke potentials, showed that $\partial f/\partial n$ becomes $\pm\infty$ at the orbit contour. In general, the equality $\partial f/\partial n = \pm\infty$ at the contours of the orbit and of the direction field folds follows from the fact that these contours are the trajectory envelopes (see Agekyan 1974).

If we numerically integrate Eq. (1) simultaneously with Eq. (7) and consider Eq. (7) at the tangency point of the orbit contour or the contour of direction-field folds, then $\partial f/\partial n = \pm\infty$ at this point.

Substituting $\partial f/\partial n = t^{-1}$ in Eq. (7) yields

$$\frac{\partial t}{\partial l} - 1 - \frac{1}{2(U+I)}\frac{\partial U}{\partial l}t \qquad (9)$$

$$-\left[\frac{3}{4(U+I)^2}\left(\frac{\partial U}{\partial n}\right)^2 + \frac{1}{2(U+I)}\gamma\right]t^2 = 0.$$

Equation (9) has the following exact limiting solution at the contours of the orbit and direction-field folds:

$$t \to 0,\ l \to 0,\ t = l.$$

Consequently, although Eq. (9) is approximate, when solving it together with Eq. (1), it gives the exact positions of the points at which $t = 0$, i.e.,

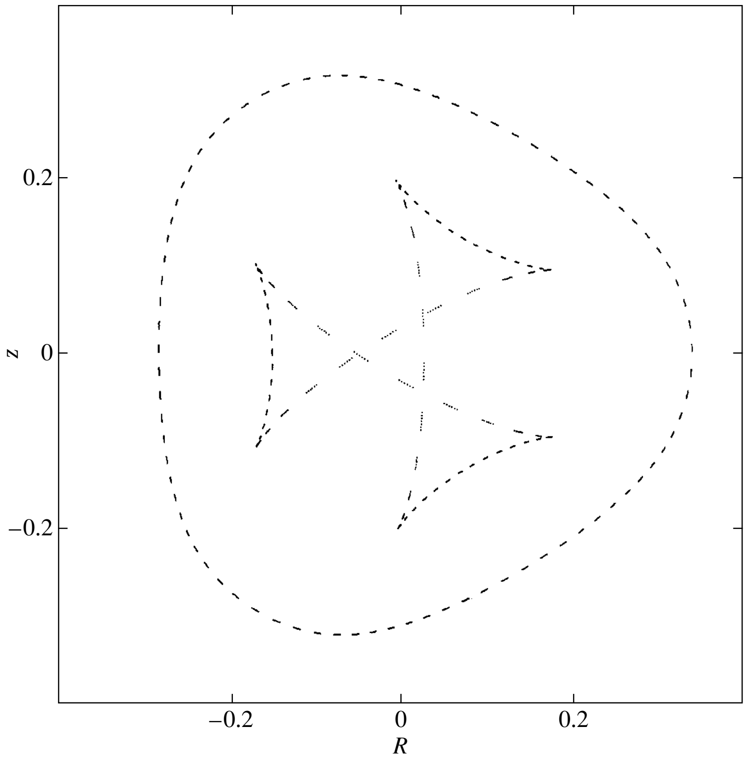

Fig. 2. The form of the orbit contours and the contours of velocity field folds for the particle trajectory shown in Fig. 1.

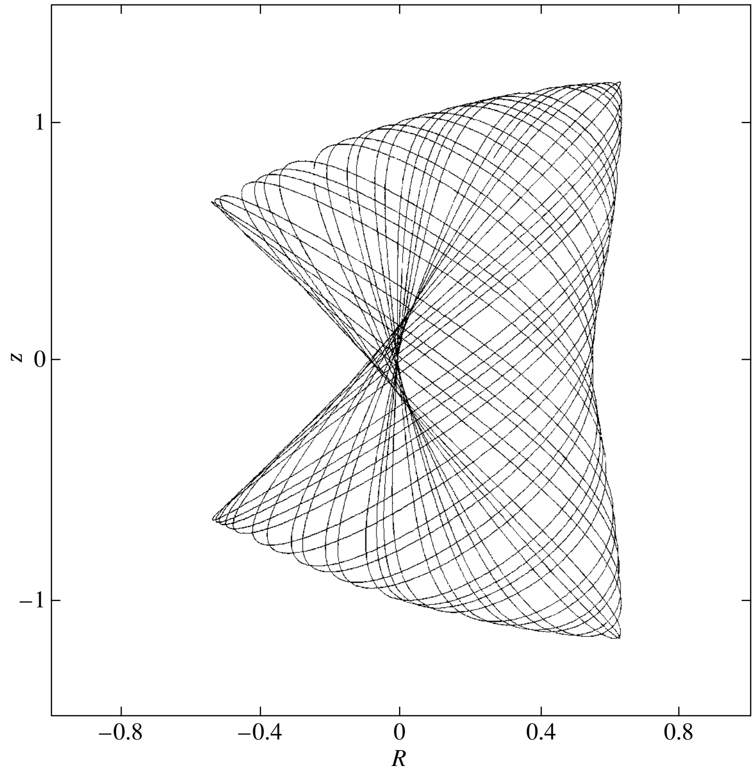

Fig. 3. Particle Trajectory in the potential of Contopoulos (1965): $A = 1$, $B = 2/3$, $\varepsilon = 1/3$, $\mu = 0$, and energy integral $I = 0.366$. The starting-point coordinate is $R_0 = 0$.

this equation defines the contours of the orbit and direction-field folds.

This approach was used by Agekyan and Yakimov (1976), Pit'ev (1980, 1981), Agekyan *et al.*

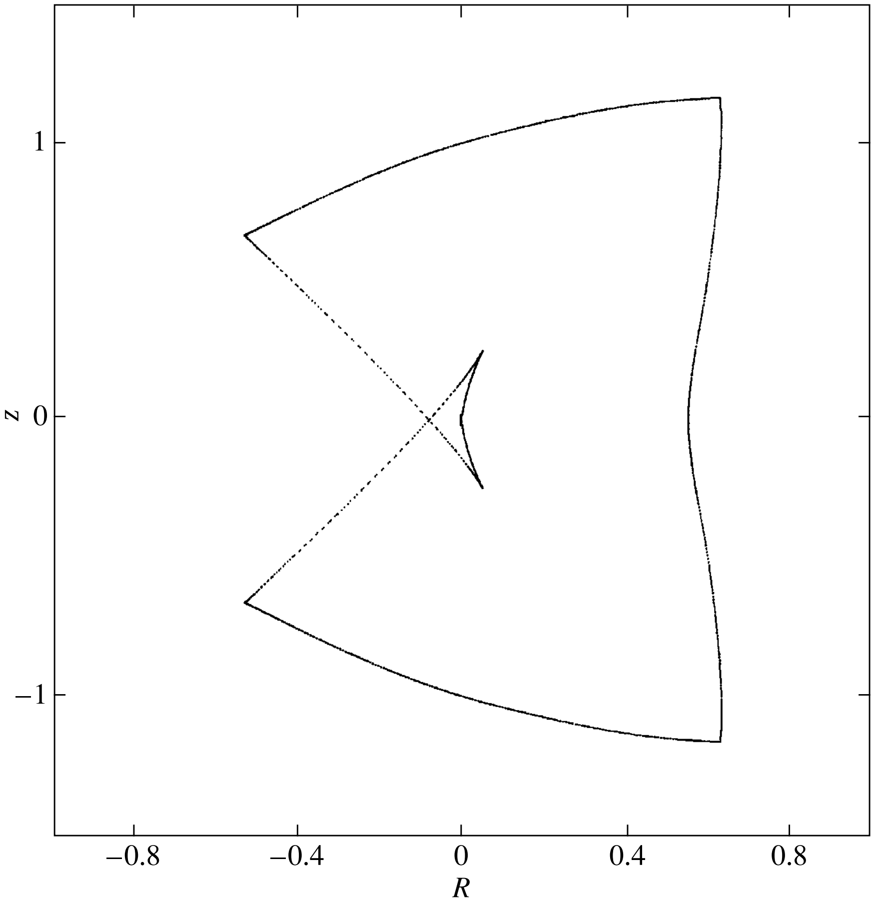

Fig. 4. Orbit contours and contours of velocity-field folds for the particle trajectory shown in Fig. 3.

(1992), Mylläri and Orlov (1993), Dubinina (2001), Agekyan and Orlov (2001), and Mylläri *et al.* (2001), and, hence, their results are correct. These results were also confirmed by directly constructing trajectory turns.

For completeness, we give here two examples of comparing the contours of orbits and direction-field folds that are barely identifiable when filling the orbits with trajectory turns and that are well defined when using Eq. (9). These examples are shown in Figs. 1–4.

We analyzed the models by Hénon and Heiles (1964) and Contopoulos (1965) whose potentials can be represented in general form as

$$U(R,z) = -\frac{1}{2}(AR^2 + Bz^2) + \varepsilon Rz^2 + \mu R^3. \quad (10)$$

The parameters, energy integral, and initial conditions used are given in the captions to the figures.

A comparison of Figs. 1 and 3 constructed by a prolonged numerical integration of the equations of motion with Figs. 2 and 4 constructed by simultaneously integrating Eqs. (1) and (9) shows that the positions for the contours of the orbit and directional-field folds coincide. These contours are well defined in Figs. 2 and 4.

In some cases (Mylläri *et al.* 2001), the contours have a very fine structure that cannot be resolved by numerically integrating the equations of motion.

REFERENCES

1. T. A. Agekyan, Dokl. Akad. Nauk SSSR **214**, 783 (1974) [Sov. Phys. Dokl. **19**, 45 (1974)].
2. T. A. Agekyan and A. A. V'yuga, Vestn. Leningr. Univ., No. 7, 128 (1973).
3. T. A. Agekian and V. V. Orlov, *Stellar Dynamics: from Classic to Modern,* Ed. by L. P. Ossipkov and I. I. Nikiforov (St. Petersb. Univ., St. Petersburg, 2001), p. 183.
4. T. A. Agekyan and S. P. Yakimov, Vestn. Leningr. Univ., No. 13, 177 (1976).
5. T. A. Agekyan, A. A. Myullyari, and V. V. Orlov, Astron. Zh. **69**, 469 (1992) [Sov. Astron. **36**, 236 (1992)].
6. G. Contopoulos, Astron. J. **70**, 526 (1965).

7. L. Dubinina, in *Stellar Dynamics: From Classic to Modern,* Ed. by L. P. Ossipkov and I. I. Nikiforov (St. Petersb. Univ., St. Petersburg, 2001), p. 198.
8. M. Hénon and C. Heiles, Astron. J. **69**, 73 (1964).
9. A. A. Myulläri and V. V. Orlov, Vestn. St. Petersb. Univ., No. 15, 120 (1993).
10. A. A. Mylläri, V. V. Orlov, and N. P. Pitjev, in *Stellar Dynamics: From Classic to Modern,* Ed. by L. P. Ossipkov and I. I. Nikiforov (St. Petersb. Univ., St. Petersburg, 2001), p. 205.
11. N. P. Pit'ev, Vestn. Leningr. Univ., No. 19, 98 (1980).
12. N. P. Pit'ev, Astron. Zh. **58**, 528 (1981) [Sov. Astron. **25**, 299 (1981)].
13. M. G. Saginashvili, Byull. Akad. Nauk Gruz. SSR, Abastumanskaya Astrofiz. Obs., No. 46, 125 (1974).

Translated by A. Dambis